

INFORMATION TO USERS

This manuscript has been reproduced from the microfilm master. UMI films the text directly from the original or copy submitted. Thus, some thesis and dissertation copies are in typewriter face, while others may be from any type of computer printer.

The quality of this reproduction is dependent upon the quality of the copy submitted. Broken or indistinct print, colored or poor quality illustrations and photographs, print bleedthrough, substandard margins, and improper alignment can adversely affect reproduction.

In the unlikely event that the author did not send UMI a complete manuscript and there are missing pages, these will be noted. Also, if unauthorized copyright material had to be removed, a note will indicate the deletion.

Oversize materials (e.g., maps, drawings, charts) are reproduced by sectioning the original, beginning at the upper left-hand corner and continuing from left to right in equal sections with small overlaps.

Photographs included in the original manuscript have been reproduced xerographically in this copy. Higher quality 6" x 9" black and white photographic prints are available for any photographs or illustrations appearing in this copy for an additional charge. Contact UMI directly to order.

ProQuest Information and Learning
300 North Zeeb Road, Ann Arbor, MI 48106-1346 USA
800-521-0600

UMI[®]

Identification of Tephtras from the Eastern Mediterranean Using Solid State Techniques

Ernesto E. Moran

A Thesis

in

The Department

of

Chemistry and Biochemistry

Presented in Partial Fulfillment of the Requirements
for the Degree of Master of Science at
Concordia University
Montréal, Québec, Canada

March 2001

© Ernesto E. Moran, 2001



National Library
of Canada

Acquisitions and
Bibliographic Services

395 Wellington Street
Ottawa ON K1A 0N4
Canada

Bibliothèque nationale
du Canada

Acquisitions et
services bibliographiques

395, rue Wellington
Ottawa ON K1A 0N4
Canada

Your file Votre référence

Our file Notre référence

The author has granted a non-exclusive licence allowing the National Library of Canada to reproduce, loan, distribute or sell copies of this thesis in microform, paper or electronic formats.

The author retains ownership of the copyright in this thesis. Neither the thesis nor substantial extracts from it may be printed or otherwise reproduced without the author's permission.

L'auteur a accordé une licence non exclusive permettant à la Bibliothèque nationale du Canada de reproduire, prêter, distribuer ou vendre des copies de cette thèse sous la forme de microfiche/film, de reproduction sur papier ou sur format électronique.

L'auteur conserve la propriété du droit d'auteur qui protège cette thèse. Ni la thèse ni des extraits substantiels de celle-ci ne doivent être imprimés ou autrement reproduits sans son autorisation.

0-612-59272-3

Canada

ABSTRACT

Identification of Tephra From the Eastern Mediterranean Using Solid State Techniques

Ernesto E. Moran

Solid state techniques have been used to characterize volcanic deposits from two areas in Greece: the Philippi peat basin, and the Myrtöön basin. The characterization involved the use of X-ray powder diffraction (XRPD) to identify the minerals present in the materials, electron probe microanalysis (EPMA) to obtain the chemical composition of the glassy components, and scanning electron microscopy (SEM) to study the morphology of the glassy components. The materials from the Philippi peat basin were found to be part of three tephra layers that are widespread in the area of study. The layers were composed of cusped glass shards, vesicular pumice shards, and mineral fragments. The upper tephra layer (UT) was 3-4 cm thick, with an approximate age of about 10 ka. The median tephra layer (MT) was 2-4 cm thick, with an approximate age of about 18 ka. Both of these tephras, UT and MT, possibly originated from the Akrotiri eruptions of the Thera volcano. The lower tephra layer (LT) was 25 – 100 cm thick, with an approximate age of 28-30 ka. This tephra had similar composition to tephras from the Campanian area of Italy.

The materials from the Myrtöön basin were composed of glass shards, vesicular pumice shards, and mineral fragments. The materials formed part of several tephra deposits that varied in thickness depending on the location from where the materials were

obtained. Two samples were found to have chemical characteristics that indicated that they had possible origins in the Minoan eruption of the volcano of Thera, which occurred 3500 years ago. Two samples had characteristics that indicated that they originated from the Akrotiri vent eruptions of the volcano of Thera, which occurred approximately 1800 years ago. Six other samples may have originated from eruptions of the volcanoes in the Campanian area of Italy that could have occurred during several periods of activity of the volcanoes in this area.

The morphology of the glassy fragments present in the tephrae from the Myrtöön and Philippi basins indicates that the eruptions that gave rise to these volcanic deposits were plinian, and that the magmas involved in the eruptions were high-viscosity magmas.

ACKNOWLEDGEMENTS

I would like to express my gratitude to my research supervisors, Dr. Georges Dénés and Dr. Karen St. Seymour, for their guidance, encouragement, friendship, and understanding. I would also like to thank them for the extraordinary commitment of their time to this project, and for all the other ways in which they have helped me during my graduate studies.

I would like to thank the members of my research committee, Dr. Peter H. Bird and Dr. Raymond Le Van Mao, for their guidance during the course of this project.

I would also like to thank the Pharmaceutical Research and Development Department at Merck Frosst for allowing me to use their X-ray diffraction and scanning electron microscopy facilities. I would also like to thank its Director, Dr. Elizabeth Vadas, for her support during this project.

I would like to acknowledge, and thank, Mr. A. Muntassar for his advice, friendship, and generous help during this project.

I would especially like to thank my wife, Sharon Booth, for her loving patience and support, and for always believing in me.

To my loving wife, Sharon

TABLE OF CONTENTS

List of Figures	xi
List of Tables	xv
Chapter 1: INTRODUCTION	1
1.1 Statement of Problem	1
1.2 Tephrochronology and its methods of study.	4
1.3 Shard morphology	8
1.4 Volcanology of the Mediterranean region	9
1.4.1 - Volcanoes of the Roman province	11
1.4.2 Volcanoes of the Campanian province	12
1.4.3 The volcanoes of the Hellenic Arc	13
Chapter 2: ANALYTICAL METHODS	15
2.1 X-ray powder diffraction	15
2.1.1 Principles	15
2.1.1.1 Production of X-rays	15
2.1.1.2 Diffraction	16
2.1.1.3 Experimental technique	17
2.1.2 Instrumentation	18
2.1.2.1 X-ray tubes	18
2.1.2.2 Diffractometer	19

2.1.2.3 Sample preparation	20
2.1.3 Analysis of XRPD data	20
2.1.3.1 Data Reduction	20
2.1.3.2 Correction of the raw data pattern	21
2.1.3.3 Generation of peak lists	27
2.1.3.4 Search/match procedure.	27
2.2 Electron probe microanalysis	33
2.2.1 Principles	33
2.2.1.1 Wavelength dispersive spectrometers (WDS)	34
2.2.2 Instrumentation	34
2.2.3 Sample Preparation	35
2.3 Scanning electron microscopy	35
2.3.1 Principles	35
2.3.2 Instrumentation	36
2.3.3 Sample Preparation	37
 Chapter 3: CORRELATION METHODS	 38
3.1 Mineralogy	38
3.2 Major element chemical analysis	40
3.2.1 The graphical correlation method.	40
3.2.2 The statistical method	43

Chapter 4: RESULTS AND DISCUSSION: EVALUATION OF SEARCH/MATCH SOFTWARE	47
4.1 Introduction	47
4.2 Effect of peaks missing from the sample pattern	52
4.3 Effect of d-spacing errors	54
4.4 Effect of errors in intensity	56
4.5 Conclusions	56
 Chapter 5: RESULTS AND DISCUSSION: METHOD SUITABILITY	 58
5.1 Introduction	58
5.2 Sensitivity of the method	58
5.3 Ability of the method to identify minerals in the presence of other minerals.	65
5.4 Conclusion	67
 Chapter 6: RESULTS AND DISCUSSION: TEPHROCHRONOLOGY OF THE PHILIPPI PEAT BASIN	 68
6.1 Description of the basin	68
6.2 Mineralogy of Tephra Layers - XRPD results	70
6.3 Shard Chemistry - Electron Probe Microanalysis Results	72
6.4 Approximate ages of the Philippi tephtras	74
6.5 Shard morphology	75
6.6 Identification of Tephra Layers	79
6.7 Summary	86

Chapter 7: RESULTS AND DISCUSSION: TEPHROCHRONOLOGY OF THE MYRTÖÖN BASIN.	89
7.1 Description of the Basin	89
7.2 Mineralogy of the tephra deposits	91
7.3 Shard Chemistry - Electron Microprobe Results	91
7.4 Approximate age of the Myrtöön tephra.	94
7.5 Shard Morphology	94
7.6 Identification of the tephra deposits.	98
7.6.1 Core 18	98
7.6.2 Core 20	102
7.6.3 Core 37	107
7.6.4 Core 39	109
7.6.5 Core 40	110
7.7 Summary	113
 References	 117
Appendix 1	120
Appendix 2	159
Glossary	168

LIST OF FIGURES

Figure 1.1	Schematic diagram of a volcanic system showing different regions from non-vesiculated magma to eruption plume	3
Figure 1.2	Map of the Mediterranean region showing the location of the areas of study, and the distribution of main volcanic centers of Quaternary age	5
Figure 1.3	Diagrammatic representation and terms for common glass shards	10
Figure 2.1	Graphical representation of the Bragg law	17
Figure 2.2	Diagram of a diffractometer setup	18
Figure 2.3	Raw intensity XRPD pattern of sample EEM-6: PH2 487-490	22
Figure 2.4	XRPD pattern of sample EEM-6: PH2 487-490 after the background corrections	23
Figure 2.5	Expansion of raw-intensity XRPD pattern of EEM-6: PH2 487-490 showing low intensity peaks.	24
Figure 2.6	Expansion of XRPD pattern of sample EEM-6: PH2 487-490 after the background corrections, showing low intensity peaks	24
Figure 3.1	The composition of eastern Mediterranean tephra layers projected in terms of wt% FeO vs K ₂ O vs CaO + MgO for all layers, showing that the marine tephra layers and their terrestrial equivalents occupy discrete fields	41
Figure 5.1	XRPD pattern of augite	61
Figure 5.2	XRPD pattern of Philippi sample used as matrix	61
Figure 5.3	XRPD of matrix plus augite at various percent concentrations	62
Figure 5.4	XRPD pattern of biotite	63

Figure 5.5	XRPD pattern of Philippi sample used as matrix (PH-4 330-335)	63
Figure 5.6	XRPD of matrix plus biotite at various percent concentrations	66
Figure 6.1	Position and approximate ages of the tephras of in the Philippi peat cores	69
Figure 6.2	SEM micrographs of glassy fragments from the upper tuff (UT) of Philippi	76
Figure 6.3	SEM micrographs of glassy fragments from the middle tuff (MT) of Philippi	77
Figure 6.4	SEM micrographs of glassy fragments from the lower tuff (LT) of Philippi	78
Figure 6.5	Distinctive groupings of various ash layers according to ratios of alkali to calcium	81
Figure 6.6	Ternary plot of the tephra layers from the upper tuff of Philippi	85
Figure 6.7	Ternary plot of the tephra layers from the middle tuff of Philippi	85
Figure 6.6	Ternary plot of the tephra layers from the lower tuff of Philippi	86
Figure 7.1	SEM micrographs of Myrtöön tephra MYR 20/1 showing bubble wall junctions and pumice shards	96
Figure 7.2	SEM micrographs of Myrtöön tephra MYR 20/2 showing bubble wall junctions and pumice shards	97
Figure 7.3	Graphical correlation graph for Myrtöön 18/12	100
Figure 7.4	Graphical correlation graph for Myrtöön 18/13	100
Figure 7.5	Graphical correlation graph for Myrtöön 20/1	104
Figure 7.6	Graphical correlation graph for Myrtöön 20/2	104
Figure 7.7	Graphical correlation graph for Myrtöön 20/3	105

Figure 7.8	Chemical characterization of deposits from Campanian origin by their alkali content	106
Figure 7.9	Graphical correlation graph for Myrtöön 37/1	108
Figure 7.10	Graphical correlation graph for Myrtöön 37/5	108
Figure 7.11	Graphical correlation graph for Myrtöön 39/2	110
Figure 7.12	Graphical correlation graph for Myrtöön 40/2	112
Figure 7.13	Graphical correlation graph for Myrtöön 40/7	113
Figure A1	X-ray diffraction pattern of Philippi sample PH-1 358-362	121
Figure A2	X-ray diffraction pattern of Philippi sample PH-1 447-450	121
Figure A3	X-ray diffraction pattern of Philippi sample PH-1 630-640	124
Figure A4	X-ray diffraction pattern of Philippi sample PH-1 640-660	124
Figure A5	X-ray diffraction pattern of Philippi sample PH-1 660-680	127
Figure A6	X-ray diffraction pattern of Philippi sample PH-2 487-490	127
Figure A7	X-ray diffraction pattern of Philippi sample PH-2 528-530	130
Figure A8	X-ray diffraction pattern of Philippi sample PH-2 830-840	130
Figure A9	X-ray diffraction pattern of Philippi sample PH-2 840-855	133
Figure A10	X-ray diffraction pattern of Philippi sample PH-3 305-309	133
Figure A11	X-ray diffraction pattern of Philippi sample PH-3 565-570	136

Figure A12	X-ray diffraction pattern of Philippi sample PH-3 570-595	136
Figure A13	X-ray diffraction pattern of Philippi sample PH-4 330-335	139
Figure A14	X-ray diffraction pattern of Philippi sample PH-4 335-350	139
Figure A15	X-ray diffraction pattern of Philippi sample PH-4 350-400	142
Figure A16	X-ray diffraction pattern of Philippi sample PH-4 400-430	142
Figure A17	X-ray diffraction pattern of Myrtöön sample MYR 18/12	145
Figure A18	X-ray diffraction pattern of Myrtöön sample MYR 18/13	145
Figure A19	X-ray diffraction pattern of Myrtöön sample MYR 20/1	148
Figure A20	X-ray diffraction pattern of Myrtöön sample MYR 20/2	148
Figure A21	X-ray diffraction pattern of Myrtöön sample MYR 20/3	150
Figure A22	X-ray diffraction pattern of Myrtöön sample MYR 37/1	150
Figure A23	X-ray diffraction pattern of Myrtöön sample MYR 39/1	153
Figure A24	X-ray diffraction pattern of Myrtöön sample MYR 39/2	153
Figure A25	X-ray diffraction pattern of Myrtöön sample MYR 40/2	156
Figure A26	X-ray diffraction pattern of Myrtöön sample MYR 40/7	156

LIST OF TABLES

Table 2.1	Peak list from raw data	25
Table 2.2	Peak list from background corrected data	26
Table 2.3	Match list after searching with full peak list.	30
Table 2.4	Line by line match list for silicon oxide showing quality of match.	31
Table 2.5	List of lines (peaks) removed by the subtraction of silicon oxide from the pattern.	32
Table 2.6	Results of the search/match procedure for sample PH2: 487-490	33
Table 3.1	Mineralogical composition of Mediterranean tephra	39
Table 3.2	Average major element composition of marine tephra layers from the Eastern Mediterranean.	42
Table 3.3	Example of calculations for correlation using coefficients of variation	45
Table 4.1	List of possible phases present in a sample pattern.	49
Table 4.2	Table showing line-by-line match of augite (24-0203).	51
Table 4.3	Effects of missing peaks on the SI score	53
Table 4.4	Effect of d-spacing error in major peaks on the SI score.	53
Table 4.5	Effect of d-spacing error in minor peaks on the SI score.	54
Table 4.6	Effect of intensity errors in a major peak on the SI score.	55
Table 4.7	Effect of intensity error in a minor peak on the SI score.	55

Table 5.1	Minerals detected by the method as a function of percent content of biotite and augite	60
Table 5.2	List of minerals included in modeled pattern	65
Table 5.3	Minerals identified in modeled sample by search/match procedure	66
Table 5.4	Remaining pattern after uPDSM search/match	67
Table 6.1	Tephra layers found in the cores from the Philippi Basin	70
Table 6.2	Mineral phases identified in the tephra from the Philippi basin	71
Table 6.3	Average major element composition of samples from the Philippi basin	73
Table 6.4	Approximate ages of the identified tephra layers from the Philippi peat basin	75
Table 6.5	Comparison of major element composition of glass shards from Philippi and from Akrotiri	82
Table 6.6	Comparison of major element composition of glass shards from Philippi and the Campanian Ignimbrite	83
Table 6.7	Correlation of tephra layers from the Philippi basin by coefficients of variation	84
Table 7.1	Location and depth of tephra layers from Myrtöön basin	90
Table 7.2	Mineral Phases identified in the tephra phases from the Myrtöön archipelago.	92
Table 7.3	Average major element composition of tephras from the Myrtöön basin	93
Table 7.4	Approximate ages of samples from the Myrtöön basin	95
Table 7.5	Comparison of major element composition of glass shards from Myrtöön and from Akrotiri.	99

Table 7.6	Correlation of tephra deposits from the Myrtöön archipelago by coefficients of variation	101
Table 7.7	Comparison of major element composition of glass shards from Myrtöön and the Campanian Ignimbrite	103
Table 7.8	Comparison of major element composition of glass shards from Myrtöön and from Minoan deposits.	111
Table A1	Peak list for Philippi sample PH-1 358-362 (EEM-1)	122
Table A2	Peak list for Philippi sample PH-1 447-450 (EEM-2)	123
Table A3	Peak list for Philippi sample PH-1 630-640 (EEM-3)	125
Table A4	Peak list for Philippi sample PH-1 640-660 (EEM-4)	126
Table A5	Peak list for Philippi sample PH-1 660-680 (EEM-5)	128
Table A6	Peak list for Philippi sample PH-2 487-490 (EEM-6)	129
Table A7	Peak list for Philippi sample PH-2 528-530 (EEM-7)	131
Table A8	Peak list for Philippi sample PH-2 830-840 (EEM-8)	132
Table A9	Peak list for Philippi sample PH-2 840-855 (EEM-9)	134
Table A10	Peak list for Philippi sample PH-3 305-309 (EEM-10m2)	135
Table A11	Peak list for Philippi sample PH-3 565-570 (EEM-11)	137
Table A12	Peak list for Philippi sample PH-3 570-595 (EEM-12)	138
Table A13	Peak list for Philippi sample PH-4 330-335 (EEM-14)	140
Table A14	Peak list for Philippi sample PH-4 335-350 (EEM-15)	141
Table A15	Peak list for Philippi sample PH-4 350-400 (EEM-16)	143
Table A16	Peak list for Philippi sample PH-4 400-430 (EEM-17)	144
Table A17	Peak list for Myrtöön sample MYR 18/12 (EEM-50)	146
Table A18	Peak list for Myrtöön sample MYR 18/13 (EEM-53)	147
Table A19	Peak list for Myrtöön sample MYR 20/1 (EEM-56)	149

Table A20	Peak list for Myrtöön sample MYR 20/2 (EEM-48)	149
Table A21	Peak list for Myrtöön sample MYR 20/3 (EEM-60)	151
Table A22	Peak list for Myrtöön sample MYR 37/1 (EEM-61)	152
Table A23	Peak list for Myrtöön sample MYR 39/1 (EEM-63)	154
Table A24	Peak list for Myrtöön sample MYR 39/2 (EEM-64)	155
Table A25	Peak list for Myrtöön sample MYR 40/2 (EEM-40)	157
Table A26	Peak list for Myrtöön sample MYR 40/7 (EEM-44)	158
Table A27	Major-element composition of Philippi sample PH-1 358-362	160
Table A28	Major-element composition of Philippi sample PH-1 447-450	160
Table A29	Major-element composition of Philippi sample PH-1 630-640	160
Table A30	Major-element composition of Philippi sample PH-1 660-680	161
Table A31	Major-element composition of Philippi sample PH-2 487 490	161
Table A32	Major-element composition of Philippi sample PH-2 528-530	162
Table A33	Major-element composition of Philippi sample PH-2 830-840	162
Table A34	Major-element composition of Philippi sample PH-2 840-855	163
Table A35	Major-element composition of Philippi sample PH-3 305-309	163
Table A36	Major-element composition of Philippi sample PH-3 565-570	163
Table A37	Major-element composition of Philippi sample PH-3 570-595	164

Table A38	Major-element composition of Myrtöön sample MYR 18/12	164
Table A39	Major-element composition of Myrtöön sample MYR 18/13	164
Table A40	Major-element composition of Myrtöön sample MYR 20/1	165
Table A41	Major-element composition of Myrtöön sample MYR 20/2	165
Table A42	Major-element composition of Myrtöön sample MYR 20/3	165
Table A43	Major-element composition of Myrtöön sample MYR 37/1	166
Table A44	Major-element composition of Myrtöön sample MYR 37/5	166
Table A45	Major-element composition of Myrtöön sample MYR 39/2	166
Table A46	Major-element composition of Myrtöön sample MYR 40/2	167
Table A47	Major-element composition of Myrtöön sample MYR 40/7	167

CHAPTER 1

INTRODUCTION

1.1 Statement of Problem

The study and characterization of fragmental material that originates from volcanic eruptions is an important component of the study of volcanoes and volcanic processes. Through these type of study, data can be obtained that may contribute to the understanding of the conditions present in a volcanic area before, and during, and eruptive period. This information can be used in the prediction of the magnitude of future eruptions, and the probability of their occurrence. [28]

Most volcanic eruptions occur as an indirect result of movement of a silicic melt that exists under the earth's crust at high temperature and pressure called the magma. The composition of this melt is dependent on variables such as chemical and mineralogical composition of the source rock, degree of melting, type and abundance of volatiles, and depth of magma generation [11].

Besides its elemental components, magma also contains dispersed in it dissolved volatiles such as H_2O , CO_2 , and SO_2 , which make up about 5 weight percent of the magma, and high temperature crystals such as quartz, plagioclase, sanidine, augite, and others biotite, depending on its elemental composition.

Because of its fluid nature, magma moves towards the surface of the earth along fissures in the earth's mantle and becomes stagnated in the earth's crust in large cavities called magma chambers. As it rises towards the surface of the earth's crust, the pressure exerted on the magma decreases. This decrease in pressure allows the exsolution of the

volatiles into gas bubbles called vesicles, which grow larger, in number and in size as the magma travels to regions of lower and lower pressure. The proliferation of the vesicles leads to the fragmentation of the magma by trapping it in the interstitial spaces between adjacent bubbles. [11]. In addition, the exsolution of the volatiles reduces the surface tension of the melt, restricting the expansion of the bubbles, and leading to overpressure of the bubbles, and to bubble bursting. (See Figure 1.1)

In an aerial explosive eruption, the rapid exsolution of volatiles from the magma, and the resulting bursting of the vesicles due to overpressure, causes the acceleration of the fragmented magma towards the surface of the earth. This process, in turn, gives rise to an eruption column that transports volcaniclastic particles from the magma chamber into the atmosphere [11]. Because of convective currents, and temperature inversion at high altitudes in the atmosphere, a mushroom-like cloud containing material of all sizes forms above the eruption center.

The fragments and other material generated by an explosive aerial eruption are either abruptly transported through the air and fall back to the surface, or into water bodies, to become *fallout deposits*, or else they become pyroclastic flow deposits from flows along the ground surface on land or beneath the sea. [11]

The erupted material settles mainly around the volcanic center. However, the finer particles can become suspended in the air, forming a cloud of ash that can be carried by the prevailing winds away from the volcanic center. The suspended ash eventually falls onto the earth surface, or into bodies of water on the earth surface (lakes, rivers, oceans) forming sheet deposits of ash in an elliptical pattern along the direction of the winds.

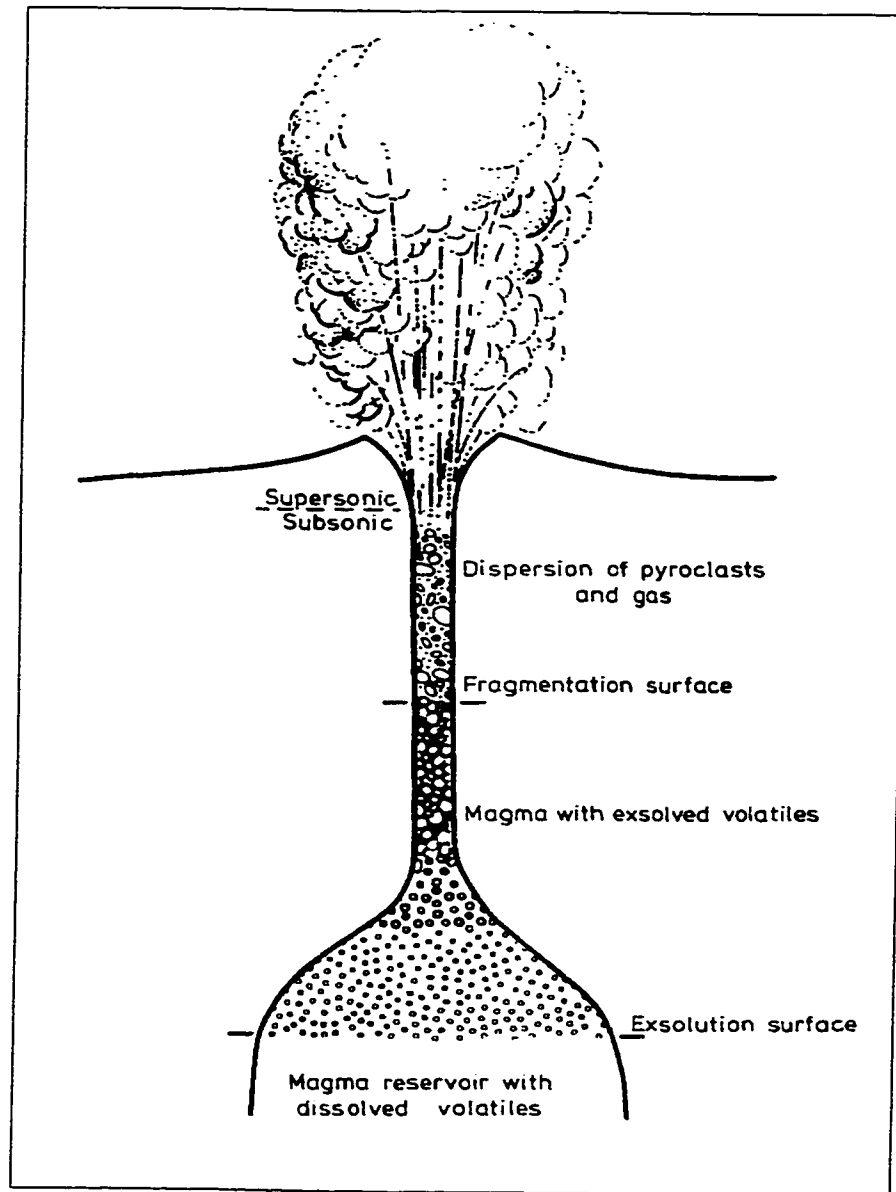


Figure 1.1 – Schematic diagram of a volcanic system showing different regions from non-vesiculated magma to eruption plume (Adapted from Fisher & Schmincke, [11]).

Since the finer particles can travel long distances when carried by the winds, deposits from a single volcanic explosion can be found spread over wide areas. Sometimes, these deposits can form near a second volcanic center, or above already existing deposits from another source, making the identification of the originating volcanic center complicated.

The problem presented in this work involved the characterization of samples of volcanic material from two separate areas of Greece through solid state techniques, with the goal of identifying the volcanic source from which the material originated. The information obtained by this study is also expected to contribute to the body of knowledge about the volcanic activity in the region. The two areas of study were (Figure 1.2):

- 1) the Philippi peat basin,
- 2) the basin off the Myrtöön Archipelago.

1.2 Tephrochronology and its methods of study.

One major kind of subaerial fallout deposit that is a product of pyroclastic eruptions is called *tephra* [11]. Fallout tephra deposits are the most extensive kind of volcanic sheet deposits (aerial), forming widespread blankets of pumice lapilli or ash. Individual sheets commonly have elliptical forms due to unidirectional wind transport. They are the result of powerful explosions and can generally be traced to a source. These sheets are especially well preserved as ash layers in deep-sea sediments, peat bogs, lake sediments, and in other areas of quiet sediment accumulation [11].

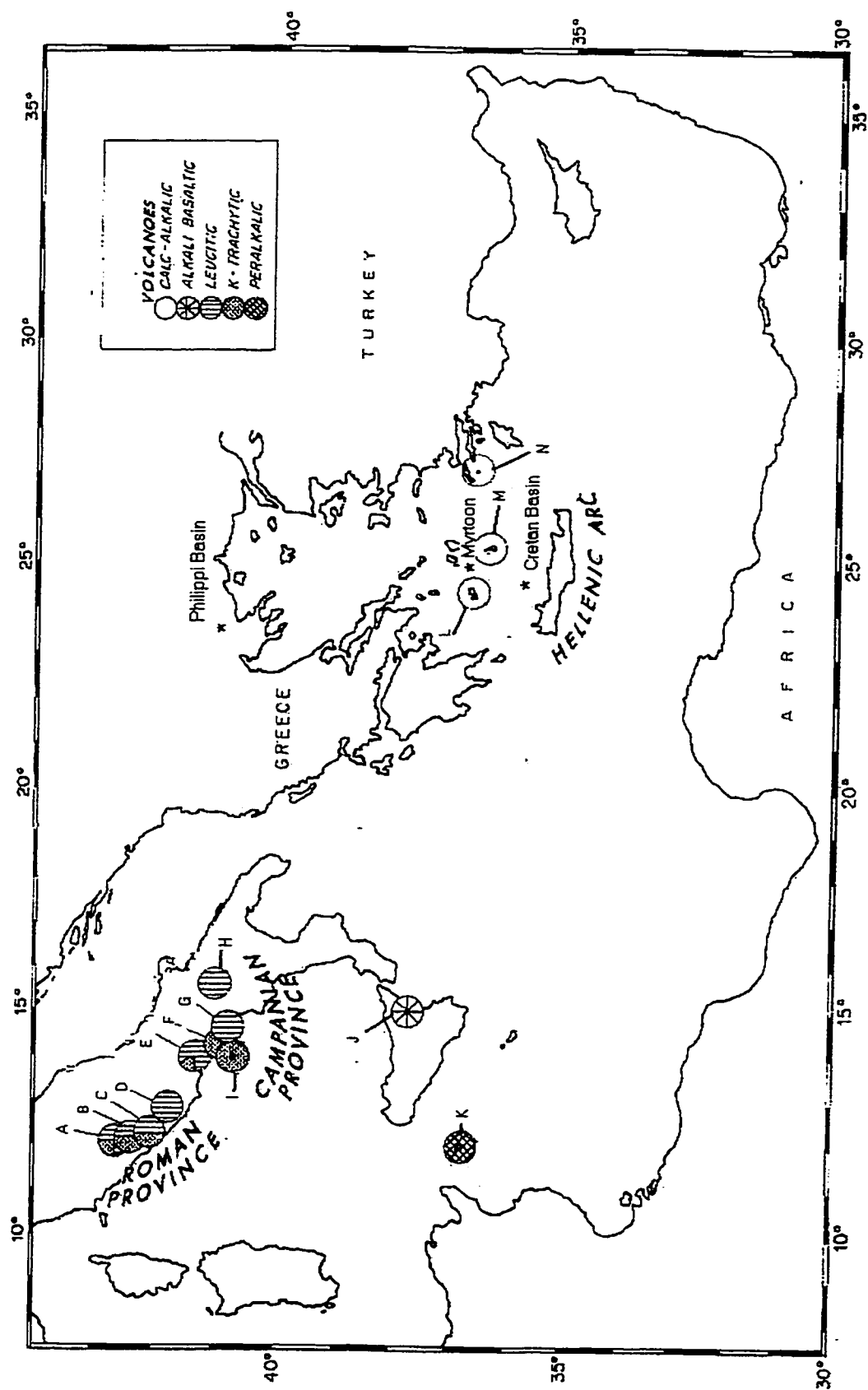


Figure 1.2 – Map of the Mediterranean region showing the location of the areas of study, and the distribution of main volcanic centers of Quaternary age [14].

A= Vulsini, B= Vico, C= Sabatini, D= Albani, E= Roccamonfina, E= Phlegrean Fields, G= Somma-Vesuvius, H= Vulture, I= Ischia Island, J= Etna, K= Pantelleria, L= Milos, M= Santorini Island, N = Nysiros.

Tephra is made up mainly of solid fragments of magmatic material that solidified as it was cooled through contact with the atmosphere or with a body of water. These fragments are usually amorphous glasses that exhibit morphological qualities such as the spherical surfaces of bubble walls. Also contained in the tephra are fragments of the high temperature minerals that were present in the originating magma at the time of the eruption, as well as other minerals that formed as the conditions in the magmatic chamber changed during the eruption [11].

The glassy fragments are classified by morphology as shards (when they are parts of a spherical wall), pumice shards (when the fragments contain the hollow cavities from many small elongated bubbles), and pumice lapilli (when they are larger fragments shaped as rods). Because tephra originates from the magma, one of the features of the glassy fragments is that they also retain the chemical characteristics of the magma at the time of the eruption.

The study of pyroclastic deposits such as tephra layers has many uses. Pyroclastic deposits have been used as stratigraphic marker horizons in archaeology, for measuring sedimentation rates in sedimentary basins, to aid in the understanding of the physical processes involved in explosive eruptions, to learn about the conditions within and underneath volcanoes, and to assess volcanic hazard. [28]

The study of tephra layers for chronological and correlation purposes are known as tephrochronology [11]. These types of studies can be used for establishing the origin of the tephra layers found in the area of interest by determining their mineralogy, chemical composition, and approximate time period of the layers.

Since the chemical composition of the tephra is reflective of the chemical

composition of the originating magma, this information helps in the identification of the volcanic source, as well as in the understanding of the processes that were in effect in the magmatic chambers during the volcanic explosion. The chemical composition of glass shards, and other pyrogenic materials, can be established using techniques such as electron microprobe, X-ray fluorescence, and atomic absorption [11].

The total mineral assemblage in the tephra is reflective of the mineral content of the originating magma, and can be used as supporting evidence in the identification of the source of the tephra layer under study because the mineral content will depend on the chemical composition of the magma. It can also yield information about conditions in the magmatic chamber such as differentiation of the magma. The mineral assembly can be determined using techniques such as X-ray diffraction, refractive index, and optical microscopy.

The time period of deposition of the volcanic material is another piece of information that is useful in tephrochronology studies since it can help differentiate between eruptions from a given volcanic source that happened at different times in the active life of the source. The approximate ages of tephra layers are often established through stratigraphical methods that correlate them to previously characterized layers by making use of the position of the layer of interest in relation to the rest of the layers present in the core. If one or more of those layers (a sapropel layer, for instance) can be identified, then the age of the layer of interest can be defined relative to the characterized layer(s). The approximate age is then expressed as older, or younger, than the previously characterized layer.

Radio-dating methods make use of radiogenic isotopes that can be found as components of the tephra material, or as components of layers such as organic material that is found in close contact with the tephra layers of interest. The ratio of radioactive isotopes to stable isotopes of the chosen element is measured, and the approximate age of the material is calculated using the rate of decay of the radiogenic isotope.

To perform the identification of the tephra materials studied for this work, several solid state techniques were employed. The chemical composition of the tephra was established by electron probe microanalysis, the mineral content of the tephra composition was studied by x-ray powder diffraction (XRPD), and the chronological origin of the tephra was established by ^{14}C dating in some cases, and by stratigraphical methods in other cases.

1.3 Shard morphology

The shape of the glass fragments that are produced during an eruption depends on the physical properties of the melt. The most familiar glass shards consist mainly of the walls of tiny broken bubbles or the junctions of bubbles developed by the vesiculation of silicic magma. Other nonvesicular processes may also form small glass particles, but they lack bubble wall texture. [11]

Among the shards from large-scale ash eruptions of high viscosity lavas (Plinian), there are essentially three types that form from shattered bubbles (Figure 1.3):

- 1) *cusate or lunate*-shaped fragments of broken bubble walls that are commonly Y-shaped and represent remnants of three bubble junctions, or double-concave plates that formed the wall between adjoining bubbles

- 2) *flat plates* from glass walls separating large flattened vesicles
- 3) *small pumice* fragments with a fibrous or cellular structure composed of small elongate or circular cavities enclosed by glass walls

Spheroidal bubbles may also be present, but they are not common.

There are many variables affecting the shape of glass shards. However, there is evidence to show that pumice shards tend to develop from relatively high viscosity rhyolitic magmas with temperature $< 850\text{ }^{\circ}\text{C}$, while bubble wall and bubble junction shards tend to develop from lower viscosity rhyolitic magmas with temperature $> 850\text{ }^{\circ}\text{C}$. Spheroidal bubbles also have been described as originating from low viscosity magmas. Shards that originate from eruptions that result in lava fountaining and ash eruptions (Hawaiian and Strombolian types) of low-viscosity lavas ordinarily do not cause particles to explode smaller pieces. Shards include smooth-skinned, slightly vesicular spheres, ovoids, teardrops, dumbbells and other similar shapes, and the broken shards of these droplets. [11]

1.4 Volcanology of the Mediterranean region

The Mediterranean region has been an area of much volcanic activity during the past 200,000 yr. The volcanic centers that can be found in this area include the volcanoes of the Roman province (Sabatini, Vulsini, Albani, and Vico) to the north of Rome in Italy, the volcanoes of The Campanian province (Ischia, Phlegrean Fields, Somma-Vesuvius, Vulture, etc) in Italy, and the volcanoes of the Hellenic Arc (Milos, Santorini, Nisyros [14]; Kos, Yali [10]) (See Fig 1.2).

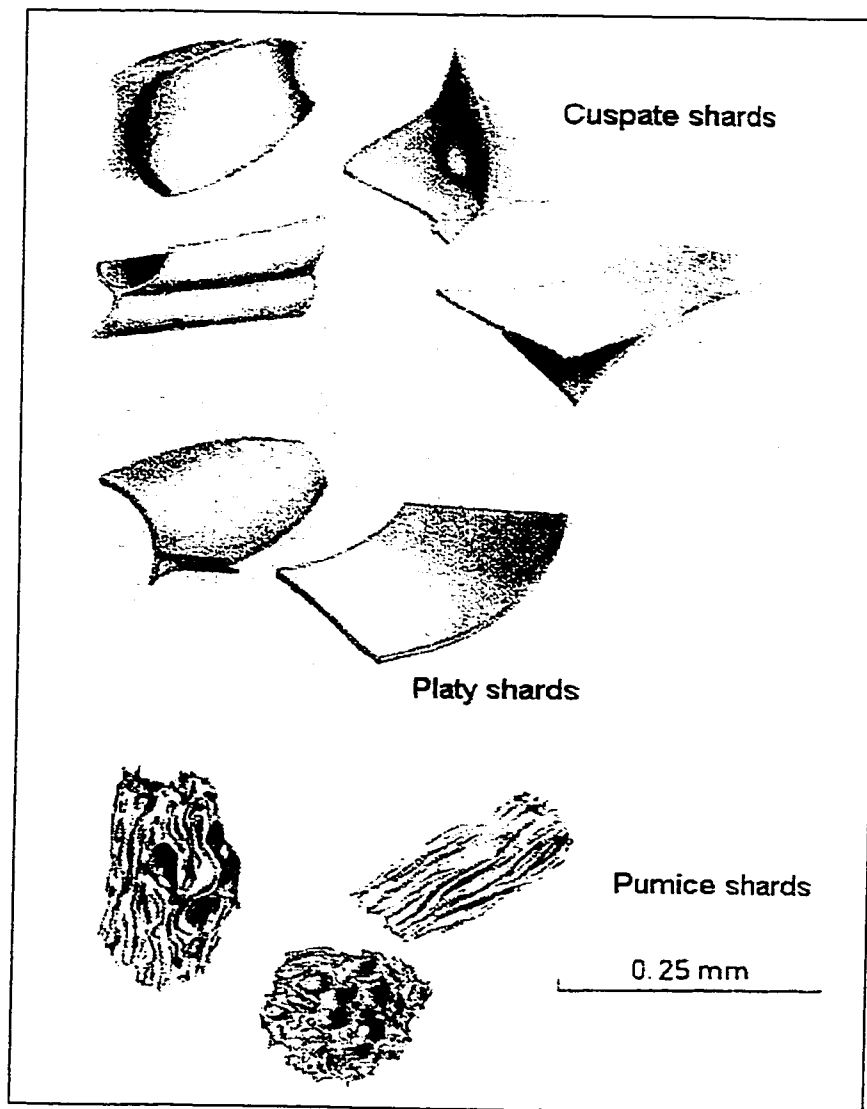


Figure 1.3 – Diagrammatic representation and terms for common glass shards (Adapted from Fisher & Schmincke [11]).

The explosions of these volcanoes have altered their respective areas in many ways such as in their geography and culture. For example, Marinatos [15] presented the theory that widespread destruction of Minoan civilization on Crete was a result of volcanic events on the Island of Santorini

1.4.1 - Volcanoes of the Roman province

The volcanoes of the Roman province are located in the central part of Italy, and include the volcanoes Sabatini, Vulsini, Albani, and Vico [8].

Sabatini is a volcanic complex with many eruptive centers. Its activity is believed to have begun about 600 thousand years ago with a mainly explosive eruptive period that was mainly due to interaction of the magma with deep groundwater. Many other periods of activity from the different centers followed until the last eruptions, which are believed to have occurred about 40 thousand years ago. The ash flows from this volcanic complex cover a large portion from what is now Rome, and have yielded the primary material for construction in that city.

The Vulsini volcanic complex was formed from four main eruptive centers that lie along main tectonic lines of weakness. Its activity is believed to have initiated about 800 ka. ago from fissural eruptive centers. The historic records indicate that eruptive activity of Vulsini occurred as recently as 104 BC. The activity of this volcano has been mainly explosive and has deposited voluminous air-fall deposits with considerable thickness.

The Albani volcano (Colli Albani, or Alban Hills) most recently erupted about 22000 years ago forming craters now filled by lakes. This volcano was formed during

several cycles of activity that started about 600 ka ago and continued until about 22000 years ago. The volcano is seismically active.

The Vico volcano is a volcano with a relatively simple structure. The volcanic history of Vico covers the period from 90 to 8000 thousand years ago. During this period, four phases of activity are recognized. These phases have been dominated by magmatic eruptions, with a few hydromagmatic eruptions. The eruptions formed many airfall deposits and lava flows.

1.4.2 Volcanoes of the Campanian province

The volcanoes of the Campanian province are located south of those of the Roman province. The volcanoes included in this province are the Phlegrean Fields, Ischia, Somma-Vesuvius, and Vulture.

The Phlegrean Fields (or Campi Flegrei) is a caldera with two historic eruptions and signs of unrest in recent years. Volcanism in the area has occurred during the past 50 thousand years, including two extremely violent explosive eruptions, the one that erupted the Campanian Tuff (35,000 years ago) and another one only 12,000 years ago which produced the Neapolitan Yellow Tuff. The two historic eruptions occurred in 1198 and 1538 AD.

The Ischia volcanic complex is an island lying off the Gulf of Napoli. The earliest dated event occurred about 53 ka ago. Ischia has seen many periods of activity since then, and it is considered to still be active. Eruptions have been ^{14}C dated at 1000, 850, 500, 470, 350, 150 and 90 BC. Other eruptions have been recorded in 69, 180, 300, and 1800-1900 AD. Continuing ground deformation indicates that the volcano will erupt again.

Somma-Vesuvius is a complex volcano with a long history. The oldest dated rock from the volcano is about 300,000 years old. Vesuvius formed after the collapse of the former Somma volcano about 17,000 years ago. One famous eruption from this volcano occurred in 79 AD. This eruption was accompanied by earthquakes, air fall deposits, pyroclastic flows, and even tsunamis. It is estimated that about 10 feet of tephra fell on Pompeii in about 19 hours, burying everything except the roofs of some buildings. Vesuvius has erupted about three dozen times since then, most recently in the period from 1913-1944.

Monte Vulture is a volcano with several eruptive centers. The first stage of formation occurred about 1 million years ago, and it was characterized by violent eruptions. The latest phase of formation was characterized by lava flows, and it was occurring as recently as 40 thousand years ago.

1.4.3 The volcanoes of the Hellenic Arc

The volcanoes of the Hellenic volcanic arc form a curved line of volcanoes stretching from Methana in the east to Kos in the west. The volcanoes in the Hellenic arc are Methana, Milos, Santorini, Nisyros, Yali, and Kos.

The Methana volcano is located on the peninsula of Methana, which is made of lava domes and lava flows. Volcanism here began in the late Tertiary or early Quaternary, with eruptions having been recorded as early as 258 BC. The rocks at Methana range from basalt to rhyodacite in composition.

Milos is located on the island of the same name. Milos is a Pliocene to Holocene volcano with no historic eruptions. Domes and lava flows make up most of the island.

Active fumaroles with temperatures up to 100 C can be found on the island. The volcanic activity gives the island the potential to produce geothermal energy.

Santorini is a complex of overlapping shield volcanoes that form an island on which investigators have found evidence of at least 12 large explosive eruptions in the last 200,000 years. The eruption of Santorini in 1650 BC was one of the largest in the last 10,000 years. About 30 cubic km of rhyodacite magma was erupted. The removal of such a large volume of magma cause the volcano to collapse, producing a caldera. The column during the initial phase of the eruption was about 23 miles high. Ash fell over a large area in the eastern Mediterranean and Turkey. It is believed that the eruption caused the end of the Minoan civilization on the island of Crete.

The Nisyros volcano is on the island of Nisyros, Greece. The pyroclastic deposits found on the island are related to two explosive phases of the volcano. The two explosive phases were probably several thousand years apart. One phase is believed to have occurred roughly 25000 years ago. The other phase is more recent with eruptions occurring in 1422, 1871, and 1873. Each phase is believed to have produced tall columns of ash above the volcano. The collapse of the tall columns of ash made the pyroclastic deposits. Also, the volume of magma erupted was great enough to cause the top of the volcano to collapse, forming a caldera.

The volcano of Yali is half made of pumice, which is being quarried at the present time. The rest of it is mad of Holocene lava domes. There are no recorded historic eruptions.

The Kos volcano is Pleistocene in age. There have been no eruptions in the last 10,000 years [8].

CHAPTER 2

ANALYTICAL METHODS

2.1 X-ray powder diffraction

2.1.1 Principles

X-ray powder diffraction (XRPD) is a powerful nondestructive technique for the identification of unknown crystalline solid state samples. This technique makes use of the properties of solids to scatter an incident beam of x-rays and produce scattering patterns that are characteristic of the crystalline solid.

2.1.1.1 Production of X-rays

X-rays are a form of electromagnetic radiation, approximately in the range of 0.5 to 2.5 Å, that are produced when particles (electrons) with enough kinetic energy are rapidly decelerated by a given material in their path. The produced X-radiation forms a smooth continuum, called heterochromatic radiation, which consists of a mixture of wavelengths and whose overall intensity depends on the voltage of the tube [7].

By increasing the voltage of the tube above a certain critical value, sharp intensity maxima can occur. These maxima, called spectral lines, are superimposed on the continuum at wavelengths that are dependent on the nature of the target material. There are several sets of lines in a given spectrum. They are identified K, L, M, etc. after the corresponding electron shell from which they originate. Since the intense narrow lines are characteristic of the target material, they and the smooth continuum are known as the characteristic spectrum of the material. [7]

XRPD experiments require radiation that is as close to monochromatic as possible. To obtain monochromatic radiation, a filter material can be employed to absorb radiation of wavelengths that are not of interest. The use of filters allows for the selection of only one set of lines, such as the K-lines, from the characteristic spectrum. The K-lines are of special usefulness because they are usually the most intense. However, the K lines are made up of two components, $K\alpha_1$ and $K\alpha_2$, which cannot be separated by the use of filters. In cases where a specific K line is desired, a monochromator can be used to select it. [7]

2.1.1.2 Diffraction

Crystals are three-dimensional arrays that are made up of periodically repeating units called unit cells, which can contain atoms, groups of atoms, or complex molecules. The unit cells can be described using sets of imaginary lattice planes that are separated by a perpendicular distance d (the d -spacing) from one another. While the planes may or may not contain atoms, the type and number of atoms that are found on these planes depends on the nature of the material.

When an X-ray beam enters a crystal, the X-rays are scattered by all atoms in the crystal that lie in the path of the beam. However, beam diffraction takes place only when the Bragg law is satisfied. This law states that constructive interference between scattered rays occurs only at certain angles, which are dependent on the d -spacing, the distance d between the atomic planes of the crystal, and the wavelength of the incident beam [7].

The Bragg law is expressed as:

$$n\lambda = 2d\sin\theta$$

where n is the order of diffraction, d is the interplanar distance, and θ is the angle formed by the incident beam and the atomic planes. Figure 2.1 illustrates the diffraction of X-rays according to the Bragg law.

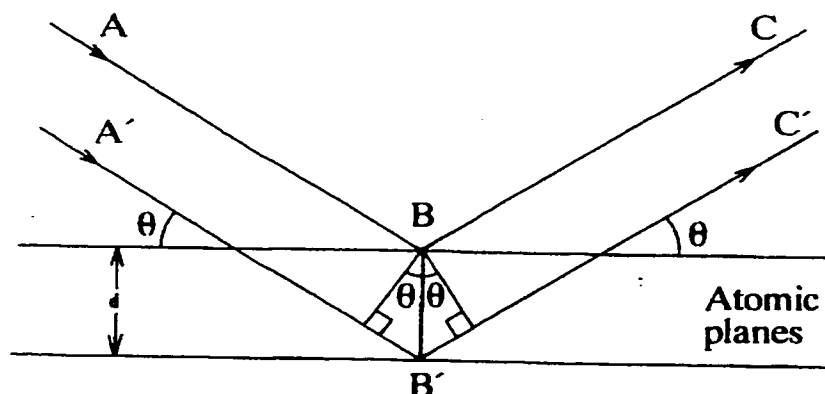


Figure 2.1 – Graphical representation of the Bragg law (Adapted from Bish & Post [3])

2.1.1.3 Experimental technique

In the powder method, an X-ray beam is directed from an X-ray tube (or less commonly, from synchrotron radiation) towards the sample under study. A scan of the angles of diffraction by a detecting device is then performed to measure the position and intensity of the diffracted beams. The intensity of the diffracted beams, which is dependent on the type and position of the atoms in the cell, is plotted against the corresponding Bragg angle. The resulting plot is a pattern of reflections that are unique to the crystal under investigation. This feature is useful in the identification of unknown substances because the position and intensity of the diffracted lines can be compared to those of known materials in a database.

2.1.2.2 Diffractometer

The diffractometer setup is illustrated in Figure 2.2.

In Figure 2.2, an X-ray beam coming from the X-ray tube passes through a collimator assembly and a divergence slit assembly, irradiating the specimen. The incident beam reaches the specimen at an angle θ from the plane of the specimen. The rays are diffracted by the specimen, pass through a receiving slit, and are detected by a radiation detector. The detecting device is set up so that it measures the diffracted radiation at an angle θ from the plane of the specimen, but at an angle 2θ from the direction of the incident beam. To maintain this geometry, in some diffractometers, the X-ray source and the detector are moved along their respective circles at the same angular velocity, but in opposite directions, while the sample remains stationary. In other diffractometers, the detector rotates at twice the angular velocity of that of the sample, while the X-ray source remains stationary. The detecting device can be a scintillation detector, a gas proportional detector, or a semiconductor type of detector called a solid-state detector [3].

The experiments described in this work were performed using a Scintag XDS 2000 X-ray diffraction system equipped with a solid state detector, a copper radiation tube, a monochromator, and a 12-position auto-sampler. The angle position was calibrated using silicon powder standard. The experiments were conducted using the $K\alpha$ line of copper (wavelength = 1.54060 armstrong units). The instrument was operated in step-scanning mode at a speed of $2\theta = 0.3$ degrees per minute, with a step size of 0.02 degrees.

2.1.2.3 Sample preparation

The samples were ground using a mortar and pestle to achieve a small and uniform particle size. The ground samples were then mounted on circular sample holders for use in the auto-sampler. In the cases where the amount of sample was too small, a low-background quartz insert was used in the sample holder to minimize the volume of the sample cavity. The quartz insert contributed no reflections to the patterns.

2.1.3 Analysis of XRPD data

2.1.3.1 Data Reduction

The data generated through XRPD experiments consists mainly of x,y paired data where x is the 2-Theta angle of diffraction and y is the intensity of the diffracted beam. This data, which is usually called the raw data, is usually represented as a graph of intensity (I) vs. 2-theta angle, and is characteristic of the material under study. This is a useful feature that allows for the identification of an unknown by comparison to the XRPD pattern to a series of known patterns using a list of peak positions. However, the raw data usually contains other components (like background intensity, and $K\alpha_2$ component of the X-radiation) that must be removed before the comparison of patterns is started.

The materials studied for this work were complex mixtures of amorphous material (glass shards, pumice shards) and crystalline mineral phases with similar chemical compositions. The XRPD patterns that were obtained for these materials contained an amorphous background as well as many overlapping reflections.

A computer-aided method was used to identify the spectrum of minerals present in the samples. The method of analysis of the XRPD data consisted of three steps:

1. Correction of the raw data pattern
2. Extraction of peak lists from the raw and corrected patterns
3. Identification of possible components present in the material through a search/match procedure

The method of analysis is best illustrated through the use of an example. The following example is the process used to analyze the data for sample EEM-6: PH2 487-490.

2.1.3.2 Correction of the raw data pattern

The raw XRPD pattern of sample EEM-6 (PH2 487-490) is shown in Figure 2.3. The pattern shows the presence of crystalline reflections superimposed on an amorphous background. In general, the peaks are of weak intensity, as compared to the intensity of peaks exhibited by a similar amount of pure minerals. A few strong, more intense reflections can be observed at around 26.5 2-Theta, but most peaks are of weak intensity.

Before a list of peak positions and intensities could be generated, some corrections had to be applied to the raw pattern. The first correction was the removal of the back ground intensity which was present as a result of effects such as non-diffractive reflection of the incident beam by amorphous material, fluorescence of the material caused by the incident beam, and electronic noise that originate from the instrumentation.

The second correction applied is the removal of the peaks generated by the $K\alpha_2$ of the X-radiation. The presence of the $K\alpha_2$ lines results in splitting of the diffraction peaks,

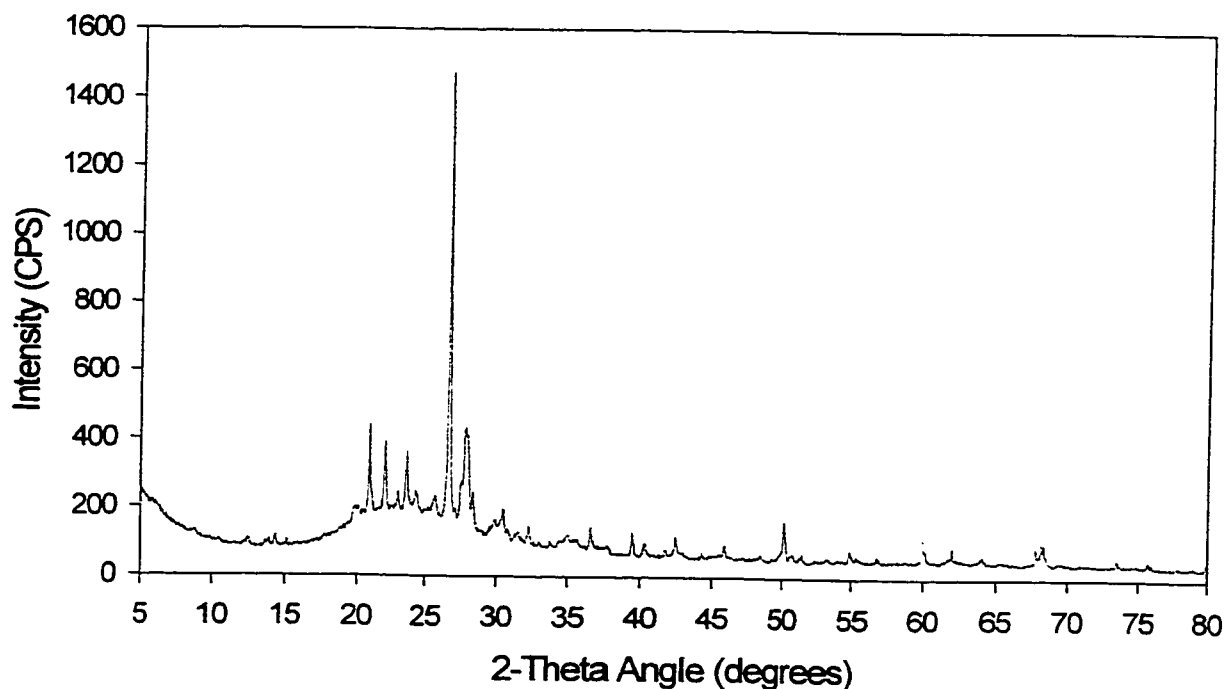


Figure 2.3 – Raw intensity XRPD pattern of sample EEM-6: PH2 487-490

and are observed as a peak shoulders at low angles, and as separate peaks at high angles. The peak splitting can, in turn, lead to the incorrect number of peaks being included in the peak list, and to a shift in the peak positions due to the overlap between the $K\alpha_1$ and the $K\alpha_2$. This correction, then, is necessary to obtain an accurate number of peaks, and more accurate peak positions.

After these two corrections were applied to the raw pattern, a new pattern was generated. The new pattern, called the net-intensity pattern, is shown in Figure 2.4. The net-intensity pattern shows reduced splitting of the peaks, as well as a flatter baseline from where a more accurate measurement of peak heights can be obtained. An expanded

view of the minor peaks of the raw and net-intensity patterns are shown in Figures 2.5 and 2.6, respectively, to show the how the corrections affected the minor peaks. Both of the pattern corrections discussed above were applied using the correction programs included in the Scintag XDS-2000 data analysis software

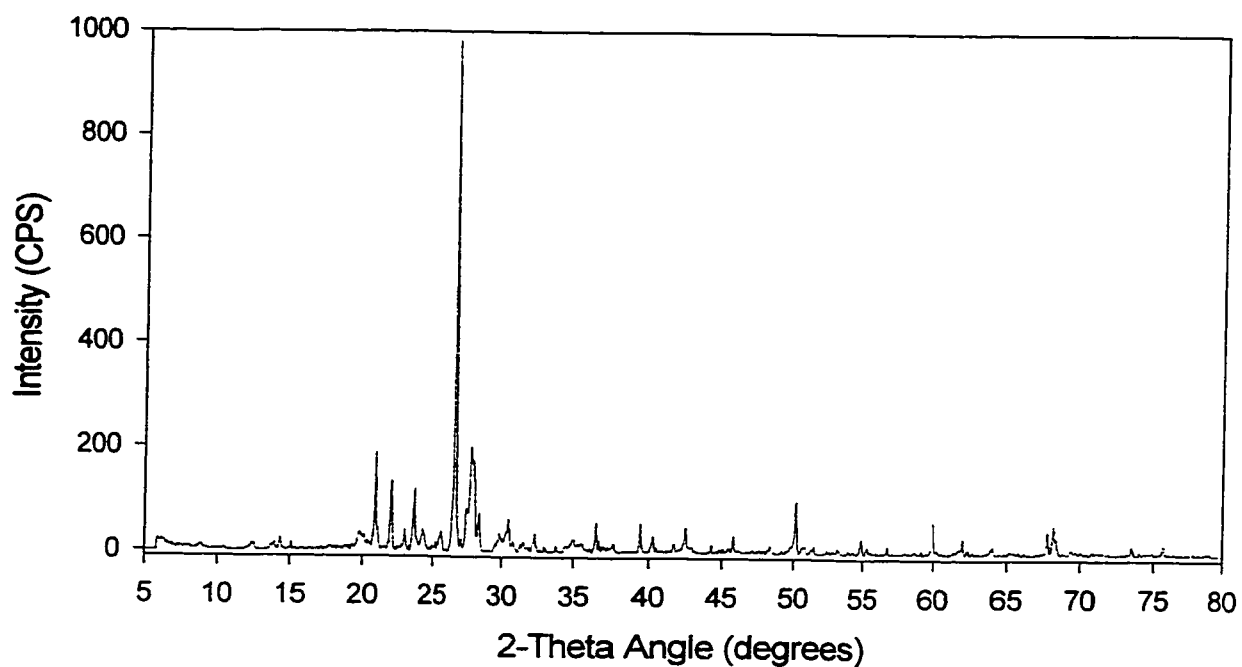


Figure 2.4 – XRPD pattern of sample EEM-6: PH2 487-490 after the background corrections.

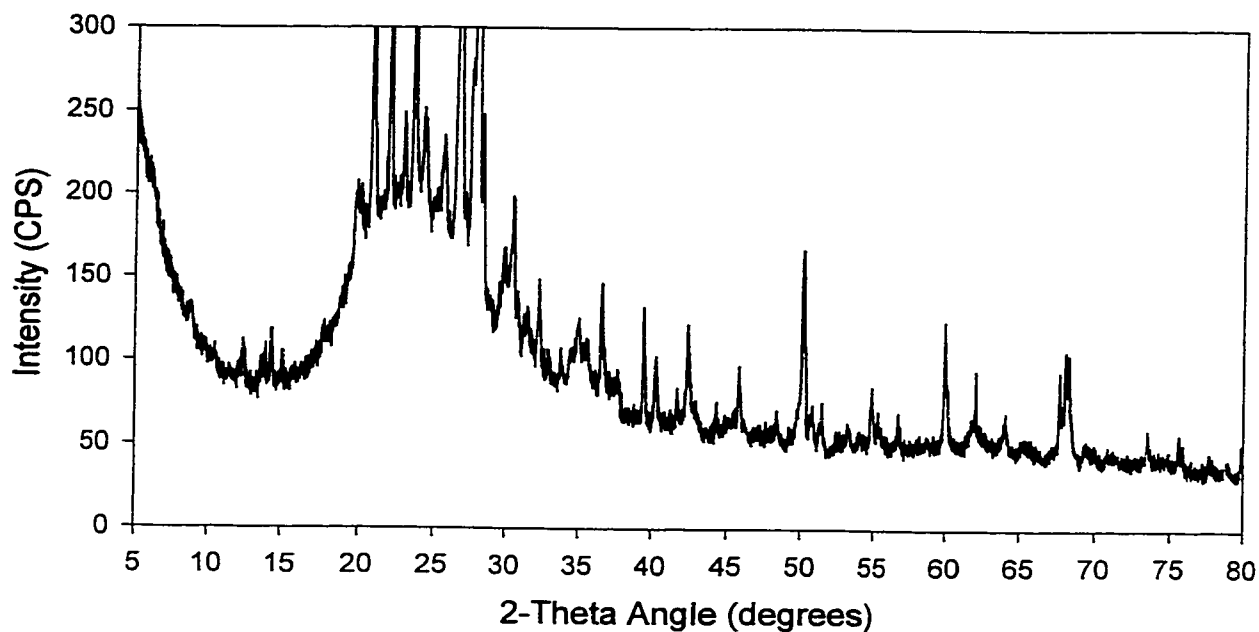


Figure 2.5 – Expansion of raw-intensity XRPD pattern of EEM-6: PH2 487-490 showing low intensity peaks.

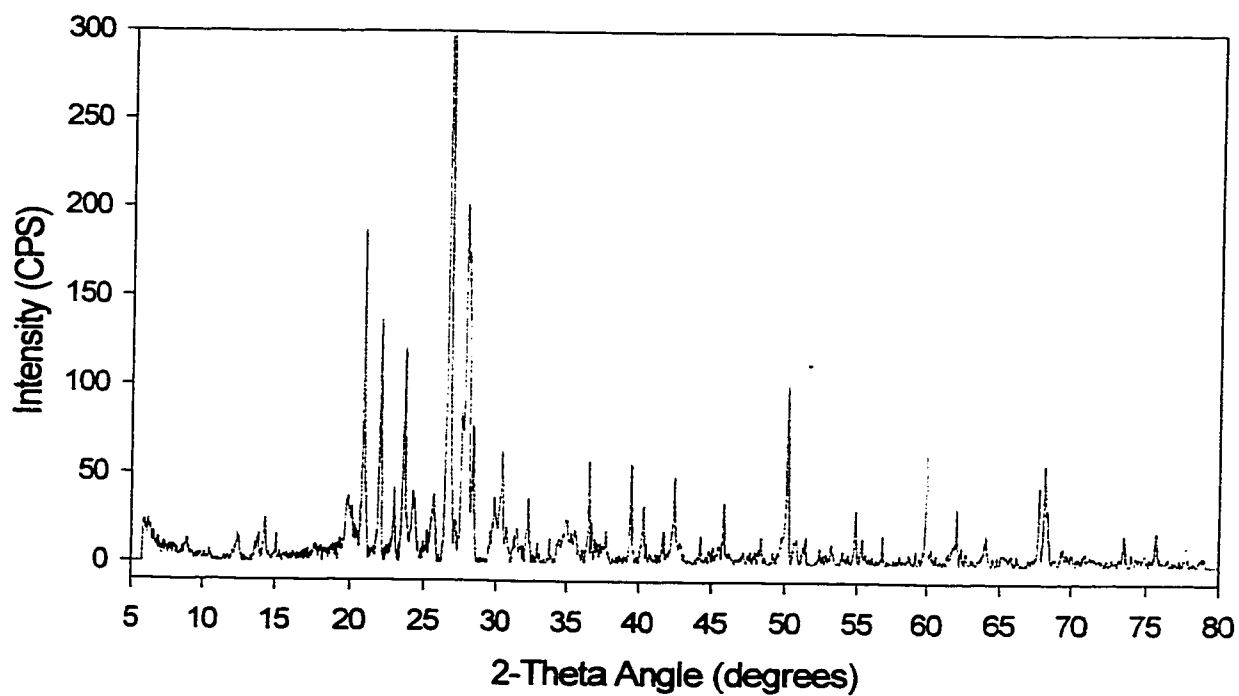


Figure 2.6 – Expansion of XRPD pattern of sample EEM-6: PH2 487-490 after the background corrections, showing low intensity peaks.

Table 2.1 - Peak list from raw data

peak #	2-theta angle	raw intensity	d-spacing	relative intensity
1	8.90	133	9.928	9
2	12.42	102	7.121	6
3	12.50	104	7.076	7
4	13.88	101	6.375	6
5	14.32	119	6.180	8
6	15.10	106	5.863	7
7	19.84	196	4.471	13
8	20.10	197	4.414	13
9	20.86	446	4.255	30
10	22.00	369	4.037	25
11	22.96	248	3.870	16
12	23.64	366	3.761	24
13	24.26	235	3.666	16
14	25.20	202	3.531	13
15	25.62	236	3.474	16
16	26.64	1465	3.343	100
17	27.06	201	3.293	13
18	27.54	275	3.236	18
19	27.80	419	3.207	28
20	27.96	412	3.189	28
21	28.32	240	3.149	16
22	29.56	143	3.020	9
23	29.84	166	2.992	11
24	30.42	199	2.936	13
25	30.76	132	2.904	9
26	31.26	126	2.859	8
27	31.48	132	2.840	9
28	32.28	149	2.771	10
29	32.92	107	2.719	7
30	33.78	101	2.651	6
31	34.48	107	2.599	7
32	34.94	119	2.566	8
33	35.30	110	2.541	7
34	35.54	111	2.524	7
35	36.54	147	2.457	10
36	36.74	108	2.444	7
37	37.68	95	2.385	6
38	39.46	133	2.282	9
39	40.28	100	2.237	6
40	41.74	84	2.162	5
41	42.44	122	2.128	8
42	44.28	74	2.044	5
43	45.80	98	1.980	6
44	48.34	69	1.881	4
45	50.14	166	1.818	11
46	50.62	65	1.802	4
47	50.74	69	1.798	4
48	51.26	64	1.781	4
49	51.44	70	1.775	4
50	54.88	85	1.672	5
51	55.32	71	1.659	4
52	56.76	70	1.621	4
53	56.90	62	1.617	4
54	59.96	124	1.542	8
55	60.08	89	1.539	6
56	62.02	95	1.495	6
57	64.06	70	1.452	4
58	67.72	94	1.383	6
59	67.94	74	1.379	5
60	68.14	107	1.375	7
61	68.32	105	1.372	7
62	73.48	60	1.288	4
63	75.64	57	1.256	3
64	77.70	46	1.228	3

Table 2.2 - Peak list from background corrected data

peak #	2-theta angle	net intensity	d-spacing	relative intensity
1	8.90	12	9.928	1
2	12.42	13	7.121	1
3	12.50	15	7.076	1
4	13.88	14	6.375	1
5	14.32	25	6.180	2
6	15.10	13	5.863	1
7	19.84	38	4.471	3
8	20.10	30	4.414	3
9	20.86	190	4.255	19
10	22.00	137	4.037	13
11	22.96	43	3.870	4
12	23.64	121	3.761	12
13	24.26	42	3.666	4
14	25.20	19	3.531	1
15	25.62	39	3.474	3
16	26.64	985	3.343	100
17	27.06	21	3.293	2
18	27.54	75	3.236	7
19	27.80	199	3.207	20
20	27.96	172	3.189	17
21	28.32	78	3.149	7
22	29.56	18	3.020	1
23	29.84	38	2.992	3
24	30.42	65	2.936	6
25	30.76	21	2.904	2
26	31.26	15	2.859	1
27	31.48	20	2.840	2
28	32.28	38	2.771	3
29	32.92	11	2.719	1
30	33.78	15	2.651	1
31	34.48	14	2.599	1
32	34.94	24	2.566	2
33	35.30	18	2.541	1
34	35.54	19	2.524	1
35	36.54	59	2.457	5
36	36.74	24	2.444	2
37	37.68	19	2.385	1
38	39.46	57	2.282	5
39	40.28	33	2.237	3
40	41.74	19	2.162	1
41	42.44	50	2.128	5
42	44.28	17	2.044	1
43	45.80	35	1.980	3
44	48.34	16	1.881	1
45	50.14	101	1.818	10
46	50.62	12	1.802	1
47	50.74	14	1.798	1
48	51.26	11	1.781	1
49	51.44	17	1.775	1
50	54.88	31	1.672	3
51	55.32	15	1.659	1
52	56.76	17	1.621	1
53	56.90	2	1.617	1
54	59.96	64	1.542	6
55	60.08	11	1.539	1
56	62.02	33	1.495	3
57	64.06	18	1.452	1
58	67.72	45	1.383	4
59	67.94	7	1.379	1
60	68.14	58	1.375	5
61	68.32	32	1.372	3
62	73.48	19	1.288	1
63	75.64	18	1.256	1
64	77.70	11	1.228	1

2.1.3.3 Generation of peak lists

Two sets of peak positions and intensities were generated. The first list was obtained through a visual examination, on the computer screen, of the raw data pattern. The second list was generated by using the first list as a guide to identify the correct position of the peaks on the net-intensity pattern.

This sequence of steps was necessary because the background subtraction algorithm used by the analysis program sometimes creates artifact peaks, and can also wipe out weak peaks. By identifying the peaks before the correction was applied, the listing of these artifact peaks, and the deletion of weak peaks, was avoided.

The two peak lists are shown on Tables 2.1 and 2.2.

2.1.3.4 Search/match procedure.

The identification of the crystalline phases was performed using a search/match procedure that compared the experimental powder pattern to the patterns included in the JCPDS database. The search/match procedure was performed with μ PDSM (Fein-Marquat and Associates, 1989), a computerized search program, and the JCPDS database containing 55984 phases.

A modified net intensity peak list (modifications consisted of generating a slightly different data format to accommodate the requirements of the software) called a JCP file was read into the search program. A search was then conducted using the entire list of peaks for the X-ray diffraction pattern. The resulting matches are shown on Table 2.3.

The top mineral choices presented by the first full search (Table 2.3) were quartz, albite, and anorthite. While all three minerals are possible components of our samples,

the program forces us to choose only one of them at a time. The user instructions for the program tell us that once the list has been narrowed to a few possible candidates, the first choice should have a combination of the following qualities:

1. It usually has the highest similarity index score (SI).
2. It has few missing lines (X), ideally none. While weak lines may not be observed, if strong lines are missing, the match must be rejected.
3. It has a higher SI/ML ratio; that is, higher SI per matched line (ML).
4. It is present at high “expected intensity” (At%), except if the phase is present at low concentrations, or it exhibits preferred orientation, in which cases the At% value will be low.

Among the three choices, it can be observed that quartz may be the best choice because of the following reasons:

- a. its SI/ML ratio is superior to that of the other two candidates (16.4 vs. 9.3 for albite, and 7.4 for anorthite)
- b. it has the least number of missing lines (1 vs. >10 for albite)
- c. it is present in the full pattern at 85% of the expected intensity (At%) vs. 29% for albite and 24% for anorthite. This means that there is little preferred orientation in quartz, as it is expected from its three dimensional system of bending. The low At% for albite or anorthite indicates either that the peak intensities do not match well, or that they are present in the sample at lower concentrations.

The match list for quartz (33-1161) is shown on Table 2.4. This table shows a line-by-line (peak-by-peak) comparison between the d-spacing position and intensity of the peaks in the reference pattern and those of the peaks from the sample pattern. The percent error in the d-spacing position of each peak is also listed. This list is useful when evaluating matched phases with similar scores.

The match for quartz (33-1161) was then subtracted. Table 2.5 shows that this procedure removed 19 peaks corresponding to quartz from the original pattern. These lines accounted for 53.5% of the total intensity of the pattern.

The process was then started again by searching the database with the remaining pattern. A new match was chosen from the new match list using the same criteria described above, and the peaks corresponding to the chosen match were subtracted from the pattern. This process was continued until one of the following events occurred:

- a) there were no peaks left in the remaining peak list, or
- b) the matches presented by the program did not include any reasonable matches.

The results obtained by this process were then tabulated. The results for the current example are listed on Table 2.6. The results show that a significant portion of the total peak intensity was due to Quartz and that the other identifiable components contributed less to the total intensity. The phases identified were quartz, albite, and orthoclase.

JCPDS#	SI	ML/X	At%	Identity	
F1					
F2					
Search Results [50 Entries]					
33-1161*	312	19/1	85	*Silicon Oxide / Quartz, syn = SiO2	
20-0548C	306	33/*	29	Sodium Calcium Aluminum Silicate / Albite, calcia	
5-0490D	299	19/1	69	Silicon Oxide / Quartz, low = SiO2	
20-0572C	273*	37/*	24	*Sodium Aluminum Silicate / Albite, ordered = NaAl	
18-1202I	254*	31/1	15	*Sodium Calcium Aluminum Silicate / Anorthite, so	
20-0528C	215	31/*	21	*Sodium Calcium Aluminum Silicate / Anorthite, so	
9-0466*	204	23/6	38	Sodium Aluminum Silicate / Albite, low = NaAlSi3O8	
20-0554C	200*	25/*	24	Sodium Aluminum Silicate / Albite, low = NaAlSi3O8	
20-0452I	193	30/*	64	Calcium Aluminum Silicate Hydrate / Gismondine =	
32-0684	186	27/*	16	Neodymium Titanium Oxide = Nd2Ti4O11	
20-0020C	172*	33/*	16	Calcium Aluminum Silicate / Anorthite, ordered =	
9-0478I	154	21/7	29	*Potassium Sodium Aluminum Silicate / Anorthoclas	
10-0359D	151	16/5	9.0	Sodium Calcium Aluminum Silicate / Andesine, low	
34-1222	145*	32/*	7.9	Barium Ytterbium Borate = Ba3Yb2(BO3)4	
9-0457I	145	17/2	10	*Sodium Calcium Aluminum Silicate / Albite, calci	
Ierr:50,150 derr:2.0 Bground:1 dmax/min:17.57/1.198					
Test Results [0 Entries]					
Plot Shift+F8	Hold F1	F2	Copy	Ins	Test F7
					Match F8
					Subtract F9
					Exit Esc

Table 2.3 – Match list after searching with full peak list.

JCPDS# SI ML/X At% Identity . . . * Obscured Lines									
33-1161* 312 19/1 85 *Silicon Oxide / Quartz, syn = SiO2									
Ierr:50,150 derr:2.0 Bground:1 dmax/min:17.57/1.198									
33-1161 @ 84.6%									
d	I	User d	Pattern	Resid I	derr	I	User d	Pattern	Resid I
4.257	19	4.255	19	-0.1	None		1.5390	1	-1.2
3.342	85	3.343	100	+0.1	None		1.4520	1	-0.8
2.457	6.8	2.4570	5	0.0	None		Below Background		
		2.4440	2	-2.2			1.3830	4	+0.5
2.282	6.8	2.2820	5	0.0	None		1.3790	1	-1.6
2.237	3.4	2.2370	3	0.0	None		1.3750	5	-0.1
		2.1380	1	+2.4			1.3720	3	+0.1
2.127	5.1	2.1280	5	+0.2	None		1.2880	1	0.0
1.9792	3.4	1.9800	3	+0.2	None		1.2558	1	+0.1
		1.8260	1	+2.5			1.2285	0.8	
1.8179	12	1.8180	10	0.0	None		1.1999	1.7	
1.8021	0.8	1.8020	1	0.0	None		Missing		
		1.7980	1	-1.3					
1.6719	3.4	1.6720	3	0.0	None				
1.6591	1.7	1.6590	1	0.0	None				
		1.6170	1	+3.4					
1.6082	0.8	Below Background							
1.5418	7.6	1.5420	6	+0.1	None				
Plot Shift+f8									
Return to Tables Esc									

Table 2.4 - Line by line match list for silicon oxide showing quality of match.

JCPDS#	SI	ML/X	At%	Identity	...
33-1161*	312	19/1	85	*Silicon Oxide / Quartz, syn = SiO2	
	Ierr:50,150	derr:2.0	Bground:1	dmax/min:17.57/1.198	
Subtraction					
Lines removed:					
	4.255	3.343	2.4570	2.2820	2.2370 2.1280 1.9800
	1.8180	1.8020	1.6720	1.6590	1.5420 1.4520 1.3830
	1.3750	1.3720	1.2880	1.2560	1.2280
No lines reduced.					
19 lines removed. No lines reduced. 54 lines left.					
46.5% of the original total intensity remains.					
Use MODIFY to make manual adjustments.					
Press Esc when ready to proceed					

Table 2.5 – List of lines (peaks) removed by the subtraction of silicon oxide from the pattern.

Table 2.6 - Results of the search/match procedure for sample PH2: 487-490

JCPDS #	SI	ML/X	At%	% of Total Intensity due to Phase	Identity
33-1161	312	19/1	85	47	Silicon Oxide/Quartz, syn Sodium calcium aluminum silicate / Albite, calcian Potassium Aluminum Silicate / Orthoclase
20-0548	291	29/6	25	15	
31-0966	72	14/0	6.1	6	

2.2 Electron probe microanalysis

2.2.1 Principles

Electron probe microanalysis is a technique used for chemically analyzing small selected areas of solid samples in which X-rays are excited by a focused electron beam. The analysis is usually conducted in a scanning electron microscope in which the SEM detector has been replaced by an electron spectrometer. Though SEM detectors are sometimes found in the equipment, they are used mainly to locate the desired spot for the analysis.

An electron beam is produced by the electron gun in the SEM and is focused onto the specimen. The electrons in the beam then cause the emission of X-rays by the processes explained before. The X-ray spectrum produced contains lines that are characteristic of the elements present in the specimen. Qualitative identification of the elements present is then achieved by identifying the wavelength of the characteristic lines (wavelength dispersive spectrometry), or by measuring the energy of the emitted X-rays (energy dispersive spectrometry). Quantitative analysis is achieved by comparing the

intensities of the characteristic lines to the intensities of a carefully selected standard. Quantitative analysis is usually performed with a wavelength dispersive spectrometer because of its higher sensitivity [21, 22].

2.2.1.1 Wavelength dispersive spectrometers (WDS)

In wavelength dispersive spectrometry, a Bragg spectrometer is constructed by mounting a crystal, with the diffracting planes parallel to the surface, on a rotating shaft. A gas proportional X-ray detector is mounted on an arm geared to the shaft in the ratio 2:1 to maintain equal angles of incidence and reflection. The X-rays from the sample that are incident on the crystal are then diffracted at angles that satisfy the Bragg law.

The spectrometer is tuned to measure the intensity of the first order reflection of the K line of the element of interest because the first order line is usually the most intense line. The spectrometer works in serial mode in which it is tuned to only one wavelength at a time. This requires making a decision about which elements to analyze. Several spectrometers (up to 5) can be mounted around the column to make analysis faster.

Quantitative analysis entails measuring the intensity of a characteristic peak of each element present in the unknown sample and comparing this peak with measurements of a standard under identical conditions.

2.2.2 Instrumentation

The microprobe analysis of the glassy fragments was conducted in a JEOL JXA 8900L WD/ED Combined Microanalyzer equipped with five detectors. The instrument was operated at a voltage of 15 kV, and a beam current of 10 nA. The measurements

were collected using a sampling rate of 20 seconds. Natural glass standards were used and ZAF corrections were applied. A highly defocused beam (12 μm in diameter) was used in order to prevent any devolatilization of the glass.

2.2.3 Sample Preparation

The glassy fragments were mounted in the sample holders by suspending them in an epoxy resin. The appropriate face of the sample holder containing the suspended sample was then polished to achieve a flat surface that contained as many glassy fragments as possible.

2.3 Scanning electron microscopy

2.3.1 Principles

In scanning electron microscopy, an image at high magnifications is produced by collecting the secondary and/or backscattered electrons that are produced in a specimen when an electron beam is scanned across the surface of specimen.

The typical scanning electron microscope usually consists of an emanating filament, several magnetic fields called condenser lenses, a specimen holder, a detector, and an output device.

In the electron gun, electrons are produced as a result of thermionic emission of a heated tungsten filament that is kept at high negative potential relative to the anode. The potential accelerates the electrons towards the anode, which has a small circular hole in its center. Through this circular hole in the anode, a beam of electrons carrying energies of between 2-40 keV is generated. The accelerated beam of electrons then travels towards

the specimen passing through a series of magnetic fields called condenser lenses. Some of these condenser lenses are used to demagnify the beam until it has a diameter of 2-10 nm when it hits the specimen, while the other condenser lenses are used to scan the beam back and forth across the specimen.

The detection mode in scanning electron microscopy is by scintillation. As the beam is scanned back and forth, a detector counts the number of backscattered electrons and other secondary electrons produced. The detector collects secondary electrons by keeping a grid at a potential of several 100 volts. This way even electrons not moving towards the scintillator are attracted. Backscattered electrons are detected exclusively when the collector is turned off.

At the same time that the beam is scanned across the specimen, a spot on a cathode ray tube (CRT) is scanned across the output screen, producing an image. Magnification of the image is achieved by scanning smaller areas while keeping the CRT scan constant.

Samples for SEM need to be electrically conducting. Otherwise, electrons accumulate at the surface of the specimen and the surface becomes negatively charged. The negative charge then repels the incident beam. To achieve electrical conductivity, a thin coat of gold or carbon is deposited on the specimen using sputter coating. [13]

2.3.2 Instrumentation

The SEM photographs were obtained using a JEOL JSM-820 Scanning Electron Microscope equipped with a Polaroid photographic camera. The microscope was operated at an accelerating voltage of 5 kV.

2.3.3 Sample Preparation

The samples for scanning electron microscopy included in this work were mounted by gluing the particles onto aluminum stubs with a conductive adhesive. The mounted samples were then sputter-coated with a gold alloy. The sputter coater (Edwards, Auto 306) was set at 1.2 kV, 20 mA for 5 minutes.

CHAPTER 3

CORRELATION METHODS

3.1 Mineralogy

The chemical composition of the magma found under the earth's surface is different from one geographical area to another. As the magma travels upwards towards the surface of the earth, and becomes trapped in magmatic chambers under volcanoes, cooling processes cause the crystallization of high temperature minerals. The type and relative amounts of high temperature minerals that crystallize out of the melt is largely dependent on the relative concentrations of each of the elements that make up the magma and, therefore, is different from one geographical area to another [11].

At the time of a volcanic explosion, the minerals that are present in the magmatic chamber are expelled by the eruption and become part of the volcanic deposits, presenting a mineralogical spectrum that can be used to identify the source of the deposits. Keller [15] compiled a list of the mineralogical composition of Mediterranean tephra layers which showed that the Hellenic volcanoes are rich in augite, hypersthene, while the Campanian volcanoes are rich in aegirine-augite, biotite, and sanidine.

In 1995, St. Seymour and Christanis [24] used this list to correlate a tephra layer from Kalodiki, in Western Greece, to the Grey Campanian Tuff. This correlation is shown on Table 3.1 as an example of how these correlations are done. The data in the table shows that the spectrum of minerals present in the Kalodiki tephra is similar to that of the volcanoes from the Campanian area of Italy.

Layer	Provenance of tephra layer	Aegirine-									
		Olivine	Augite	Augite	Hyperssthene	Hornblende	Biotite	Apatite	Sphene	Zircon	Plagioclase Sanidine
X-1	Helenic andesite (Thera-Nisyros- Milos)		xxx		xxx			x			xxx
V-1	Lower pumice Thera		xxx		xxx	x		x			xxx
V-3	Thera		xxx					x			xxx
Y-3	Campanian trachyte	x		xxx		x	xxx	x			xx xxx
Y-5	Grey Campanian tuff			xxx		x	xxx	x	x		xxx xxx
Y-7	Campanian acmite trachyte (Ischia Isalnd)			xxx	xx		xx	x	x	x	xx xxx
	Kalodiki tephra			xxx			x	x	x		xx xxx

Table 3.1 – Mineralogical composition of Mediterranean tephra layers (Adapted from St. Seymour [24]).

3.2 Major element chemical analysis

Major element analysis of the glassy components of tephra (glass shards, pumice shards) has been found to be the most useful tool used in the identification and correlation of unknown tephra layers [10].

The correlation is usually accomplished by a direct comparison of the percent major element composition of an unknown sample to that of previously identified samples. In this work, two other methods were used to confirm the results obtained by the traditional method:

- 1- a graphical correlation method that compares the alkali content of unknown samples to that of tephra layers which are commonly found in the eastern Mediterranean.
- 2- a statistical correlation method which compares the composition of an unknown sample to that of a known sample using the % concentration of 5 major elements.

3.2.1 The graphical correlation method.

The graphical method is based on the work of Federman and Carey [10] who observed that when the percent K_2O vs. FeO vs. $(CaO + MgO)$ were plotted using ternary graphs, distinct groupings arose that could be used in the identification of the layers.

Figure 3.1 is a representation of the ternary graph presented by Federman and Carey. On this graph, the authors have plotted the percent K_2O vs. FeO vs. $(CaO + MgO)$ composition of glass and pumice shards from tephra layers from the Eastern Mediterranean.

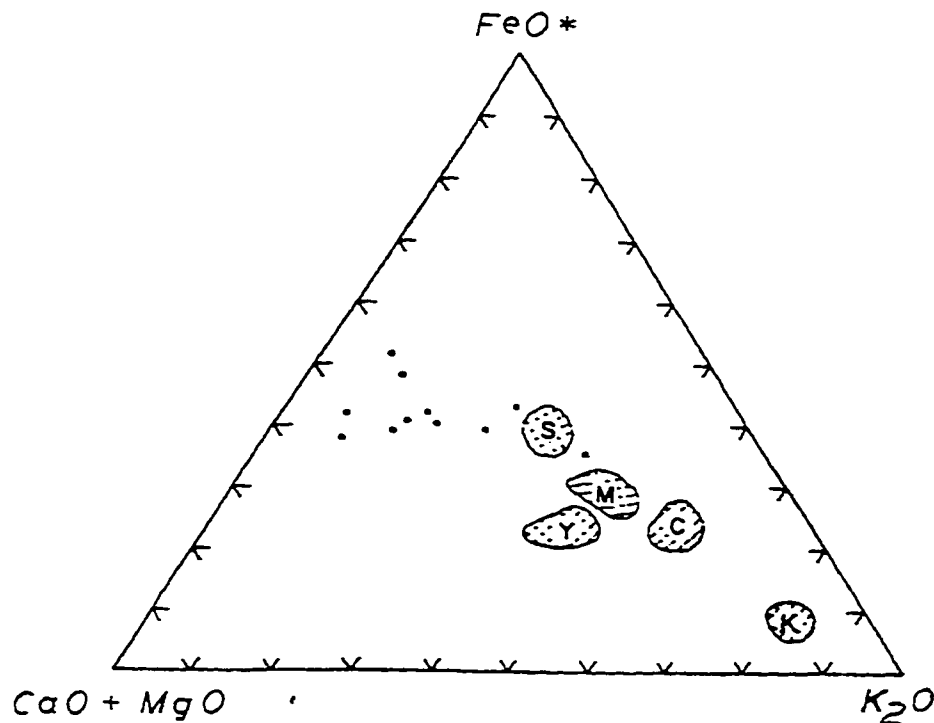


Figure 3.1 – The composition of eastern Mediterranean tephra layers projected in terms of wt% FeO vs K₂O vs CaO + MgO for all layers, showing that the marine tephra layers and their terrestrial equivalents occupy discrete fields. (M) Minoan, (S) Akrotiri (18,000 yr B.P.), (Y) Yali-C, (C) Campanian, and (K) Kos Plateau. (Adapted from Federman and Carey [10])

Each of the layers had been correlated previously to a respective terrestrial source by major element, electron probe microanalysis of glass and pumice shards (Table 3.2).

The correlation showed that there were five widespread layers that were identified as:

1. the Minoan layer, which originated from an eruption on the island of Santorini that occurred approximately 3300 years ago.
2. the Akrotiri ignimbrite layer, which also originated from the island of Santorini and is approximately 18000 years old;

Tephra Layer	Layer Symbol	SiO ₂	Al ₂ O ₃	FeO	MgO	CaO	Na ₂ O	K ₂ O	TiO ₂	Total
Minoan	M	72.5	13.7	1.9	0.26	1.3	4.9	3.1	0.26	97.7
Akrotiri	S	71.5	14.3	2.9	0.38	1.8	5.7	2.8	0.42	99.8
Yali C	Y	71.8	14.4	1.8	0.46	1.8	4.5	3.5	0.32	98.6
Campanian	C	61.4	18.3	2.8	0.35	1.8	6.9	7.2	0.37	99.1
Middle Pumice	X	63.6	15.5	5.7	1.4	4	4.5	2.4	1.1	98.2
Kos Plateau	K	73.5	12	0.42	0.03	0.5	4.2	4.2	0.05	94.9

Table 3.2 - Average major element composition of marine tephra layers from the Eastern Mediterranean.
(Adapted from Federman and Carey [10])

3. the Yali layer, which originated from an eruption of Yali volcano that occurred 31000 years ago.
4. The Campanian layer, which originated from the volcanoes in the Campanian province of Italy and is thought to be about 37000 years old;
5. and the Kos Plateau layer, which originated from eruptions of the Kos volcano about 20000 years ago.

The ternary graph shown in Figure 3.1 shows how the plot of K_2O vs. FeO vs. $(CaO + MgO)$ separated each of the widespread layers and their terrestrial equivalents into discrete fields, making the graph useful in the identification of tephra layers by graphical analysis.

3.2.2 The statistical method

The statistical method is based on the work of Borchardt et al [4] who correlated volcanic ash deposits in the Pacific Northwest to sources in the Cascade Mountains. This method was also successfully used by Federman and Carey [10] to correlate marine ash deposits in the eastern Mediterranean to land deposits in the same region, as described before.

The statistical method uses variation analysis, and it basically expresses the compositional differences between two samples in terms of relative concentrations. To perform this comparison, the method uses only 1 number to represent the relative concentration of 5 elements present in a sample and a reference.

The method is illustrated by the following general example. In the example, a five element vector containing the concentrations of five elements [A1, A2, A3, A4, A5] is compared to a reference vector [B1, B2, B3, B4, B5] containing the concentrations for the same elements. In general,

the sample vector $A = [A1, A2, A3, A4, A5]$

is compared to the reference vector B for a known sample $= [B1, B2, B3, B4, B5]$

by dividing A by B and obtaining a ratio vector

$C = A/B = [C1, C2, C3, C4, C5]$.

With this method, each element of the new vector is nearly 1.00 if the vectors A and B are similar. The variation about the average of all elements of the new vector C is a measure of the dissimilarity of the two analyses. The variance is given by the coefficient of variation (CV) calculated from the standard deviation (s) about the average (x):

$$\% CV = (s) (100/x)$$

where $x = (C1 + C2 + C3 + C4 + C5)/5$ and s is the standard deviation.

For a sample that correlates well with a known reference, then the average ratio of all elements in the sample will approach 1.0 and the coefficient of variation will be low. The method can be used to compare unknown samples to a list of possible sources, where the source with the lowest CV is the most likely match for the sample.

Table 3.3 illustrates how the method was used to correlate one of our unknown sample to the chemical composition of five identified layers in the Mediterranean. In this

Element	Philippi 630-640		Minoan		Akrotiri		Yali C		Campanian		Middle Pumice		Kos Plateau	
	Composition	Ratio	Composition	Ratio	Composition	Ratio	Composition	Ratio	Composition	Ratio	Composition	Ratio	Composition	Ratio
SiO ₂	61.18	0.8	72.50	0.9	71.50	0.9	71.80	0.9	61.40	1.0	63.60	1.0	73.50	0.8
TiO ₂	0.33	1.3	0.26	0.8	0.42	0.8	0.32	1.0	0.37	0.9	1.10	0.3	0.05	6.6
Al ₂ O ₃	19.42	1.4	13.70	1.4	14.30	1.4	14.40	1.3	18.30	1.1	15.50	1.3	12.00	1.6
FeO	2.48	1.3	1.90	0.9	2.90	0.9	1.80	1.4	2.80	0.9	5.70	0.4	0.42	5.9
MgO	0.28	1.1	0.26	0.7	0.38	0.7	0.46	0.6	0.35	0.8	1.40	0.2	0.03	9.4
CaO	1.41	1.1	1.30	0.8	1.80	0.8	1.80	0.8	1.80	0.8	4.00	0.4	0.50	2.8
Na ₂ O	6.00	1.2	4.90	1.1	5.70	1.1	4.50	1.3	6.90	0.9	4.50	1.3	4.20	1.4
K ₂ O	7.83	2.5	3.10	2.8	2.80	2.8	3.50	2.2	7.20	1.1	2.40	3.3	4.20	1.9
AVERAGE														
Std. Dev		1.3		1.2		1.2		1.2		0.9		1.0		3.8
Coefficient		0.5		0.7		0.7		0.5		0.1		1.0		3.1
		37.8		60.2		60.2		42.6		12.3		99.9		81.3

Table 3.3 - Example of calculations for correlation using coefficients of variation

example, the vectors that are being compared are the major element compositions of a Philippi sample and the major element composition of the layers identified by, and as reported by, Federman and Carey [10] (Table 3.2). The comparison was performed using the same elements used by Federman and Carey (Si, Al, Ca, Fe, and K) to form the vectors.

When correlated using this method, the tephra in our sample showed lower %CV when compared to the tephra from the Campanian area of Italy than when compared to the other tephtras. This observation led to the conclusion that our unknown sample originated from the Campanian area.

The correlation tables reported in the tephrochronology sections were calculated in a similar manner. However, only the final % CV's are shown in the tables, not the intermediate calculations.

CHAPTER 4

RESULTS AND DISCUSSION

EVALUATION OF SEARCH/MATCH SOFTWARE

4.1 Introduction

μ PDSM is a commercial search program that uses the JCPDS PDF2 database as its reference. This database contains the peak lists from patterns of more than 55900 crystalline materials (as of 1989). The program operates by comparing the position and intensity of the list of peaks in a pattern to those of patterns contained in the database. Once a possible match has been identified, the match is qualified with a “Similarity Index” (SI) score. The SI score is based on factors such as:

- the ratio of number of line matched versus the missing lines (ML/X),
- the error in the position of the lines as compared to the lines in the reference pattern,
- and the relative intensity of matched lines in the sample as compared to that of the lines in the reference phase (At%).

The general procedure followed when using the search/match software consists of performing a search, choosing the best match from a list of possibilities, and subtracting the chosen pattern from the original pattern. According to the instructions provided with the software by the publisher, the best match is not necessarily the one with the highest SI. The software manual states that the best choice has a combination of the following qualities:

- It usually has the highest similarity index score (SI)
- It has few missing lines (X), ideally none. While weak lines may not be observed, if strong lines are missing, the match must be rejected.
- It has the highest SI/ML ratio; that is, the highest SI per matched line (ML).
- It is present at high “expected intensity” (At%), except if the phase is present at low concentrations, or it exhibits preferred orientation, in which cases the At% value will be low.

However, the most important of these qualities is, according to the publisher of the software, the SI score.

Table 4.1 shows an example of a list of possible matches for a sample pattern.

The meaning of the column headings is:

JCPDS#	The JCPDS number from the PDF2 database for the phase
SI	the similarity index
ML	the number of lines from the sample pattern that match lines in that phase
X	the number of lines present in the reference pattern that are not in the sample pattern
At%	the percentage intensity as compared to a perfect match
Identity	the identity and the chemical formula of the reference pattern.

JCPDS#	SI	HL/X	At%	Identity	:	:
F1						
F2						
Search Results [50 Entries]						
24-0203I	679	33/0	100	*Calcium Iron Magnesium Silicate / Augite = Ca(Mg		
19-0239D	352	35/*	126	Calcium Magnesium Silicate / Diopside, syn = CaMg		
11-0654I	307	35/*	178	*Calcium Magnesium Silicate / Diopside = CaMg(SiO		
19-0001D	204	19/7	125	*Sodium Calcium Iron Aluminum Silicate / Acmite-a		
31-0305I	204	19/7	125	*Calcium Sodium Iron Manganese Zinc Silicate / Ae		
24-0202I	162	18/6	112	*Calcium Aluminum Iron Magnesium Silicate / Augit		
38-0466I	141	26/*	123	Calcium Magnesium Aluminum Iron Silicate / Diopsi		
24-0201I	111	11/8	93	Calcium Iron Magnesium Silicate / Augite = Ca(Fe,		
25-0154D	80	17/*	115	Calcium Magnesium Aluminum Silicate / Diopside, a		
8-0179D	78	7/4	39	Magnesium Carbonate Hydroxide Hydrate / Hydromagn		
37-0518C	71	11/*	79	*Lead Oxide Sulfate = Pb302S04		
18-0507	65	4/0	56	Europium Oxide = EuO		
36-1179	65	13/*	13	Germanium Rhenium = Ge7Re3		
36-1494*	61	14/*	66	Lead Oxide Sulfate = Pb302(S04)		
22-14430	61	8/4	23	Strontium Titanium Oxide = SrTi12019		
Ierr:50,150				derr:2.0	Bground:4	dmax/min:4.504/1.259
Test Results [0 Entries]						
Plot Shift+F8	Hold F1	F2	Copy Ins	Test F7	Match F8	Subtract F9
						Exit Esc

Table 4.1 – List of possible phases present in a sample pattern.

According to the program instructions, if the elemental composition is appropriate, some of the matched phases with the higher SI scores can be considered to be present in the sample that corresponds to the pattern being analyzed [27]. However, when none of the phases that are contained in a sample are included in the database, even the suggested matches with the highest SI values are of poor quality and unacceptable. In addition, in many instances where the sample is a complex matrix of crystalline phases with similar chemical composition, it can be difficult to choose a compound from the match list because the SI scores of the top matches are not significantly different. In these cases it is necessary to examine the quality of the match for all the phases under consideration, and to understand how the SI scores are generated. This is necessary because, as in many computer-aided searches, the results obtained through μ PDSM depend to a large extent on the quality of the input data, and on the restrictions placed on the search.

The object of this study was to evaluate the program to understand how the SI score is generated, so that in cases where the scores are close to one another a more educated selection can be made. To accomplish this objective a series of tests were performed using a pattern taken straight from the JCPDS database. The pattern used was that of the mineral augite (# 24-02031) because it was a mineral phase that was expected to be present in our samples. Since the peak list corresponded to a pattern from the database, the match was a perfect one. This perfect match had a score SI=679, a matched/missing peak ratio (ML/X) of 33/0, and a percent intensity (At%) of 100. (See Table 4.2)

JCPDS#	SI	HL/X	At%	Identity	...	Obscured Lines
24-0203I	679	33/0	100	*Calcium Iron Magnesium Silicate / Augite = Ca(Mg ₂ Si ₂ O ₆)		
	Ierr:50,150	derr:2.0	Bground:4	dmax/min:4.504/1.259		
24-0203 @100.0% User Pattern						
d	I	d	I	derr	Resid	
4.464	12	4.464	12	0.0	None	
3.234	75	3.234	75	0.0	None	
2.994	100	2.994	100	0.0	None	
2.949	65	2.949	65	0.0	None	
2.895	34	2.895	34	0.0	None	
2.839	7	2.839	7	0.0	None	
2.566	55	2.566	55	0.0	None	
2.516	65	2.516	65	0.0	None	
2.497	4	2.497	4	0.0	None	
2.300	22	2.300	22	0.0	None	
2.213	10	2.213	10	0.0	None	
2.200	6	2.200	6	0.0	None	
2.153	22	2.153	22	0.0	None	
2.134	35	2.134	35	0.0	None	
2.108	16	2.108	16	0.0	None	
2.073	6	2.073	6	0.0	None	
2.041	25	2.041	25	0.0	None	
2.016	17	2.016	17	0.0	None	
Plot Shift+F8						
24-0203 @100.0% User Pattern						
d	I	d	I	derr	Resid	
1.835	12	1.835	12	0.0	None	
1.812	6	1.812	6	0.0	None	
1.753	30	1.753	30	0.0	None	
1.625	35	1.625	35	0.0	None	
1.616	17	1.616	17	0.0	None	
1.612	9	1.612	9	0.0	None	
1.587	8	1.587	8	0.0	None	
1.562	13	1.562	13	0.0	None	
1.550	13	1.550	13	0.0	None	
1.527	8	1.527	8	0.0	None	
1.487	16	1.487	16	0.0	None	
1.421	35	1.421	35	0.0	None	
1.407	12	1.407	12	0.0	None	
1.331	15	1.331	15	0.0	None	
1.263	8	1.263	8	0.0	None	
Return to Tables Esc						

Table 4.2 – Table showing line-by-line match of augite (24-0203).

The parameters that were studied were those that were considered to influence the SI score of a matched phase. These parameters were:

- the effect of missing peaks
- the effect of error in the d-spacing position of the peaks
- the effects of errors in the intensity of the peaks

4.2 Effect of peaks missing from the sample pattern

To evaluate the effect of a missing peak on the SI score of the match, several peaks of different intensity were removed, one at a time, from the pattern. The search/match routine was conducted with the resulting patterns to see what the new SI score would be as compared to the original score. The results of the study are shown on Table 4.3.

The results indicate that the SI score is achieved by assigning a value to each matched peak. In this case, the maximum average value per peak is given by $SI/ML = 679/33$, or approximately 20.6/peak. The results also indicate that when a peak is missing a combination of corrections are made to the SI score:

- The contribution of that peak to the SI score is subtracted from the total score
- The At% value is adjusted down to match the intensity of the remaining peaks
- The original SI score seems to have been adjusted by multiplying it by the new At% value.

Table 4.3 - Effects of missing peaks on the SI score

% intensity of missing peak	d-sp (Å)	SI found	ML/X	At%
-----	-----	679	33/0	100
75	3.234	474	32/1	75
65	2.949	506	32/1	79
65	2.516	506	32/1	79
22	2.300	628	32/1	96
35	2.134	597	32/1	91

Table 4.4 - Effect of d-spacing error in major peaks on the SI score.
(Major peak - 100% rel. int.)

% error	d-sp (Å)	SI found	ML/X	At%
0.0	2.994	679	33/0	100
-0.5	2.990	679	33/0	100
-1.0	2.985	678	33/0	100
-2.0	2.976	669	33/0	100
-2.5	2.971	661	33/0	100
-3.0	2.967	394	32/1	67

Table 4.5 - Effect of d-spacing error in minor peaks on the SI score.
(Minor peak - 12% rel. int.)

% error	d-sp (Å)	SI found	ML/X	At%
0.0	1.835	679	33/0	100
-0.5	1.833	679	33/0	100
-1.0	1.832	679	33/0	100
-2.0	1.828	671	33/0	100
-2.5	1.826	664	33/0	100
-3.0	1.824	645	32/1	100

4.3 Effect of d-spacing errors

The effect of d-spacing errors was evaluated by modifying the d-spacing value of a major peak (100% relative intensity), and a minor peak (12% relative intensity) and performing the search/match routine with the resulting pattern. The modifications involved the decrease of the value by an appropriate % error using the formula used by the software program to calculate d-spacing errors. :

$$\text{Error} = 0.001 * d^2$$

Where d = % error. Using this formula, an error of 2% translates to an error value of 0.004 Å units in the d-spacing position.

Since the formula uses a square of the % error, the direction of the error (increasing or decreasing) has the same effect on the results. For this part of the study, the error window limit was kept at 3.0 %.

The results of the study are shown on Table 4.4 for the case of error in a major peak, and on Table 4.5 for the case of error in a minor peak. The results show that as the % error was increased, the SI score was reduced by a comparable amount, regardless of whether the error was in a major peak or in a minor peak. The magnitude of the correction increased proportionally with the magnitude of the error until the % error was equal to the value of the error window setting (3.0). When the error equaled the error setting, the peak in consideration was considered to be a “missing peak” which led to the kind of penalties described in the previous section.

Table 4.6 - Effect of intensity errors in a major peak on the SI score.
(Major peak - 75% rel. int.)

% error	intensity	SI found	ML/X	At%
0	75	679	33/0	100
-10	67	677	33/0	100
-20	60	675	33/0	98
20	90	678	33/0	102

Table 4.7 - Effect of intensity error in a minor peak on the SI score.
(Minor peak - 25% rel. int.)

% error	intensity	SI found	ML/X	At%
0	25	679	33/0	100
-10	22	678	33/0	100
-20	20	678	33/0	100
20	30	679	33/0	101

4.4 Effect of errors in intensity

The effect of errors in the intensity of the peak on the SI score was evaluated by changing the intensity of a major peak (75% relative intensity) and of a minor peak (25% relative intensity). The results of the study (Tables 4.6 and 4.7) show the SI score was not affected significantly by errors in intensity. The SI score remained almost constant (~679) even at intensity errors of 20%. The only major corrections seem to have been related to changes in the At% value.

4.5 Conclusions

The SI score assigned by the μ PDSM program to a match is based largely on the number of peaks in the reference pattern that match peaks from the sample pattern. The higher the number of matched peaks, the higher the SI score. If there are peaks from the reference pattern that are missing in the sample pattern, the SI score is lowered. This action lowers the ratio of SI/ML, which seems to have a maximum of about 20 SI units per ML. The At% value of the match is lowered according to the intensity of the remaining peaks. This effect is more pronounced when major peaks are missing. Errors in d-spacing, and intensity, of the peaks also affect the SI score, but the effect is not as much as that observed with missing peaks.

When evaluating a list of possible matches with similar SI scores, a good decision can be made by choosing the one with the following characteristics:

- a) fewest missing peaks,
- b) largest ratio of SI/ML (closer to about 20 is better),

- c) when the At% is low, the best choice is the one with fewer major peaks, unless there is a considerable amount of preferred orientation,
- d) the match has the lowest error in peak position.

CHAPTER 5

RESULTS AND DISCUSSION

METHOD SUITABILITY

5.1 Introduction

The successful identification of components present in a mixture is dependent on the suitability of the method of analysis to detect them, as well as its ability to differentiate the individual components from the matrix containing them.

In this study, the ability of the X-ray diffraction and search/match methods to detect and identify important minerals present in a mixture was evaluated through a series of tests. The evaluation was conducted in two parts:

- a) The sensitivity of the method to the presence of minerals at low levels, and its ability to identify important minerals in the presence of an amorphous matrix.
- b) The ability of the method to correctly identify minerals in the presence of other minerals.

5.2 Sensitivity of the method

The sensitivity of the method was tested by spiking one of the samples with known amounts of natural augite or biotite, and grinding them together to produce a uniform mixture. These minerals were chosen because they are two of the main minerals that were expected to be in the tephra, and it was necessary to know the lower limits for the detection and identification of these important minerals. The sample matrix that was chosen was a Philippi sample that had previously been characterized during the course of this work as containing few minerals and being mostly amorphous. The minerals that had

been identified previously in this sample included quartz, albite, and orthoclase.

The XRPD patterns that were generated for this study are shown in Figures 5.1 to 5.6. Figure 5.1 shows that the three strongest peaks from augite are at 2-theta angles of 29.8 (#1), 30.2 (#2), and 35.5 degrees (#3). The matrix contained peaks of low intensity at these angles, however they could not be completely resolved (Figure 5.2). Figures 5.3 shows that the peak at 29.8 degrees could be seen in the pattern corresponding to 4% augite content, however the other 2 peaks could not be resolved until the concentration of augite reached 10%.

Figure 5.4 shows that the two strongest peaks from biotite occurred at 2-theta angles of 8.8 (#1) and 26.7 degrees (#2). These two peaks were also present in the matrix, and could be seen to increase in intensity as the biotite content increased (Figure 5.6). The peak at 26.7 degrees also corresponds to the strongest peak of quartz, which was identified as the main crystalline component of the matrix. At the lower biotite concentrations, the peak at 26.7 degrees was completely subtracted with the peaks corresponding to quartz, which prevented the detection of biotite.

The results of this study are listed in Table 5.1. The lists of minerals show that that our experimental conditions and analytical methods were able to identify the presence of augite and biotite at levels as low as 10% w/w. However, when biotite and augite were present at levels of 6% w/w, the method failed to detect their presence in the matrix. Unfortunately, there were peaks originating from the other minerals in the matrix that overlapped with the strongest peaks of both augite and biotite. This overlap probably resulted in a higher limit of detection than would have been the case if the overlap had not occurred.

Mineral Name	Percent biotite present in matrix (w/w)						Percent augite present in matrix (w/w)					
	0	4	6	10	20		0	4	6	10	20	
Quartz	x	x	x	x	x		x	x	x	x	x	
Albite	x	x	x	x	x		x	x	x	x	x	
Orthoclase	x	x	x	x	x		x	x	x	x	x	
Biotite												
Augite										x	x	

Table 5.1 - Minerals detected by the method as a function of percent content of biotite and augite

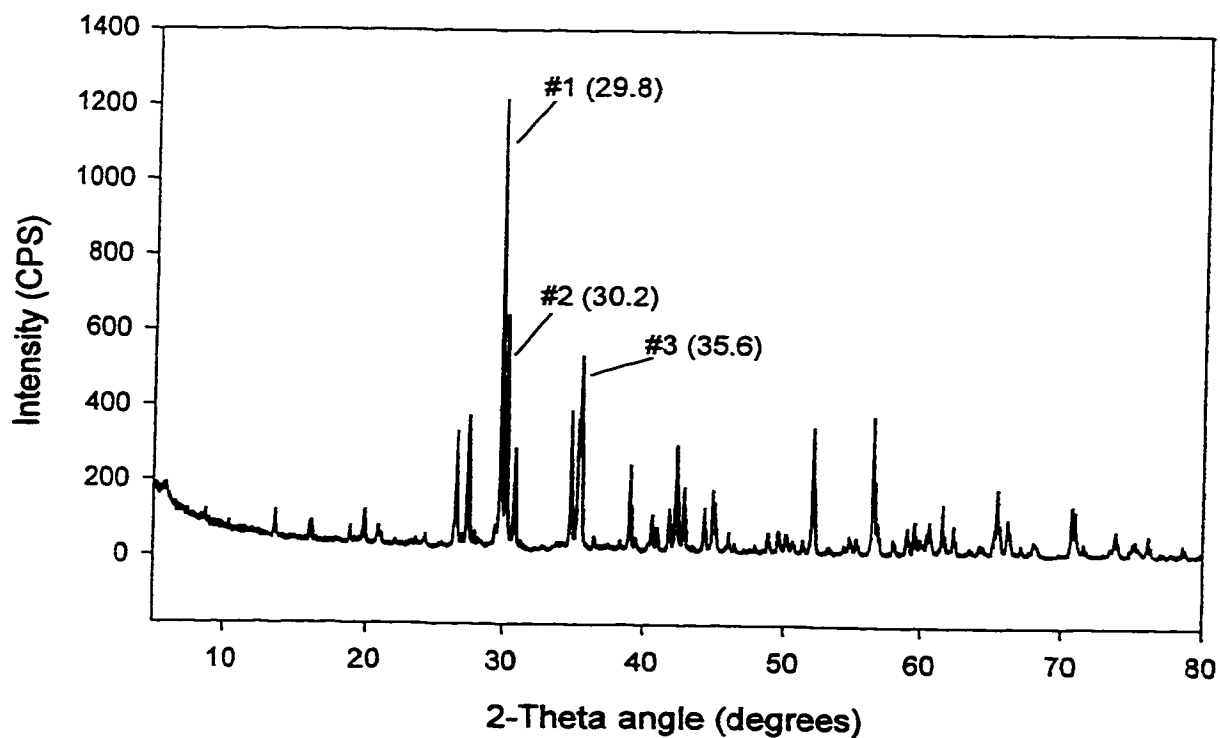


Figure 5.1 - XRPD pattern of augite

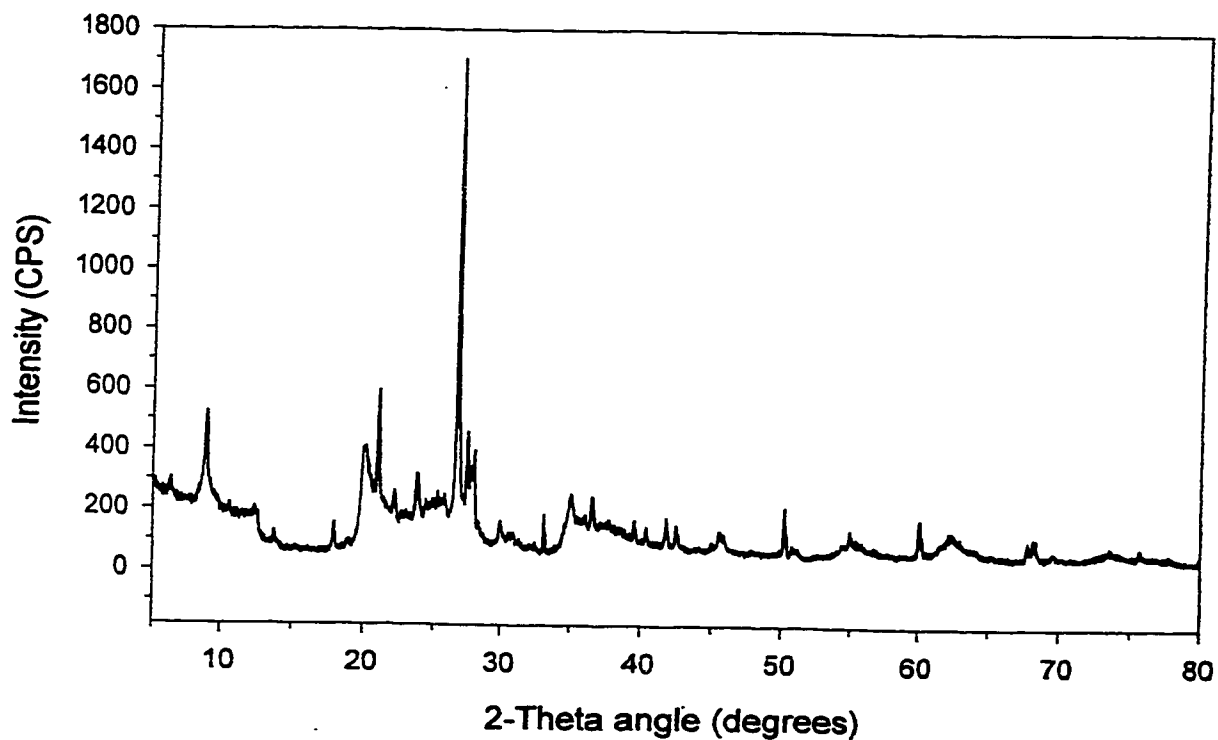


Figure 5.2 - XRPD pattern of Philippi sample used as matrix (PH-4 330-335)

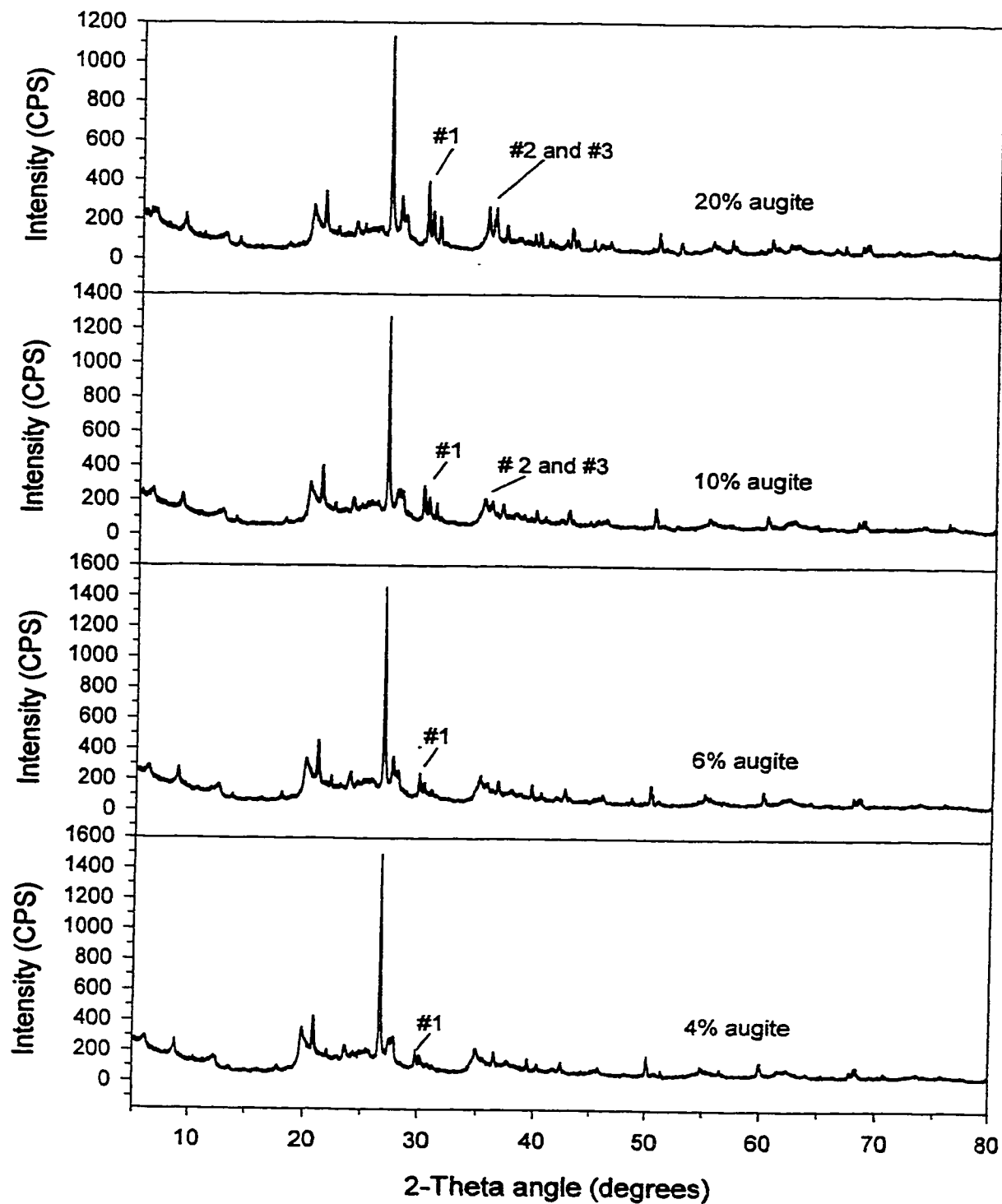


Figure 5.3 - XRPD of matrix plus augite at various percent concentrations

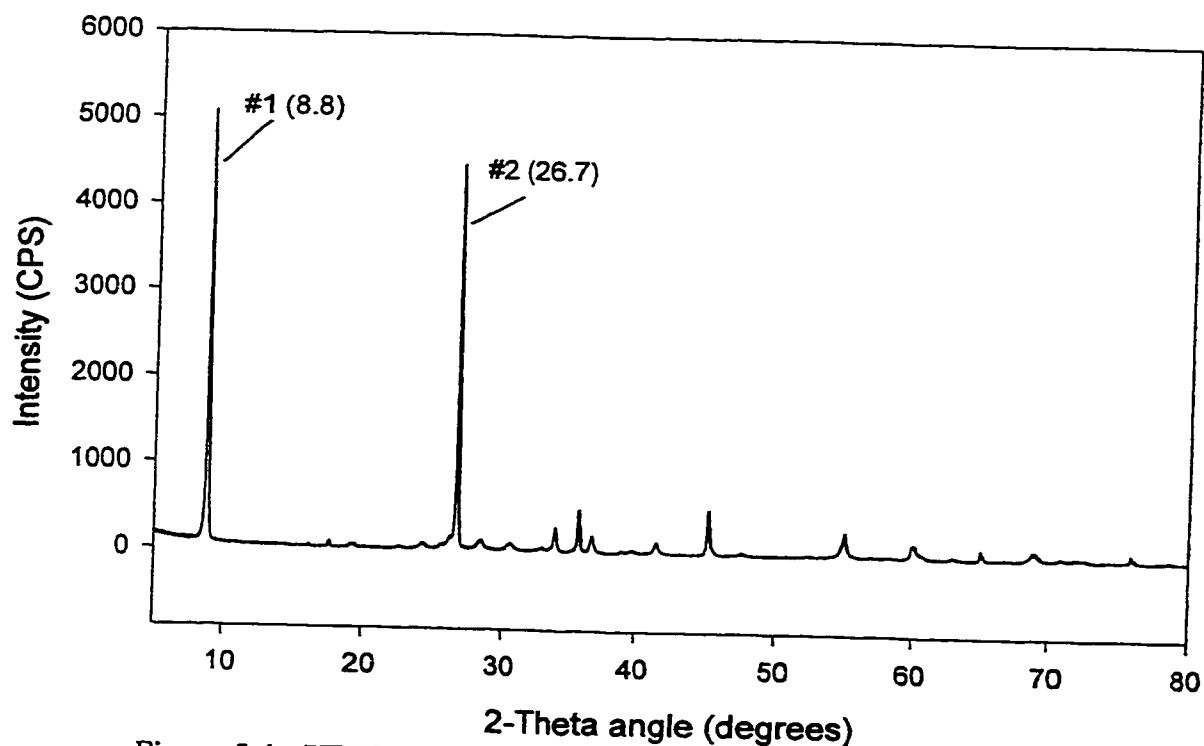


Figure 5.4 - XRPD pattern of biotite

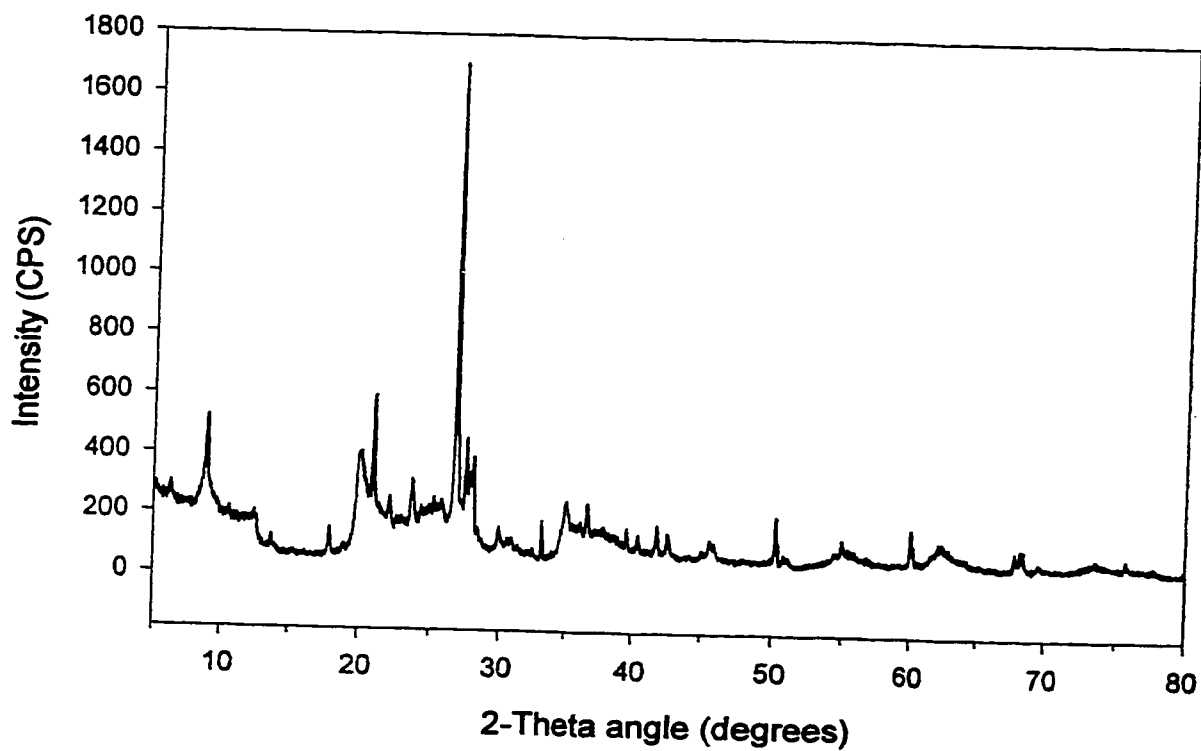


Figure 5.5 - XRPD pattern of Philippi sample used as matrix (PH-4 330-335)

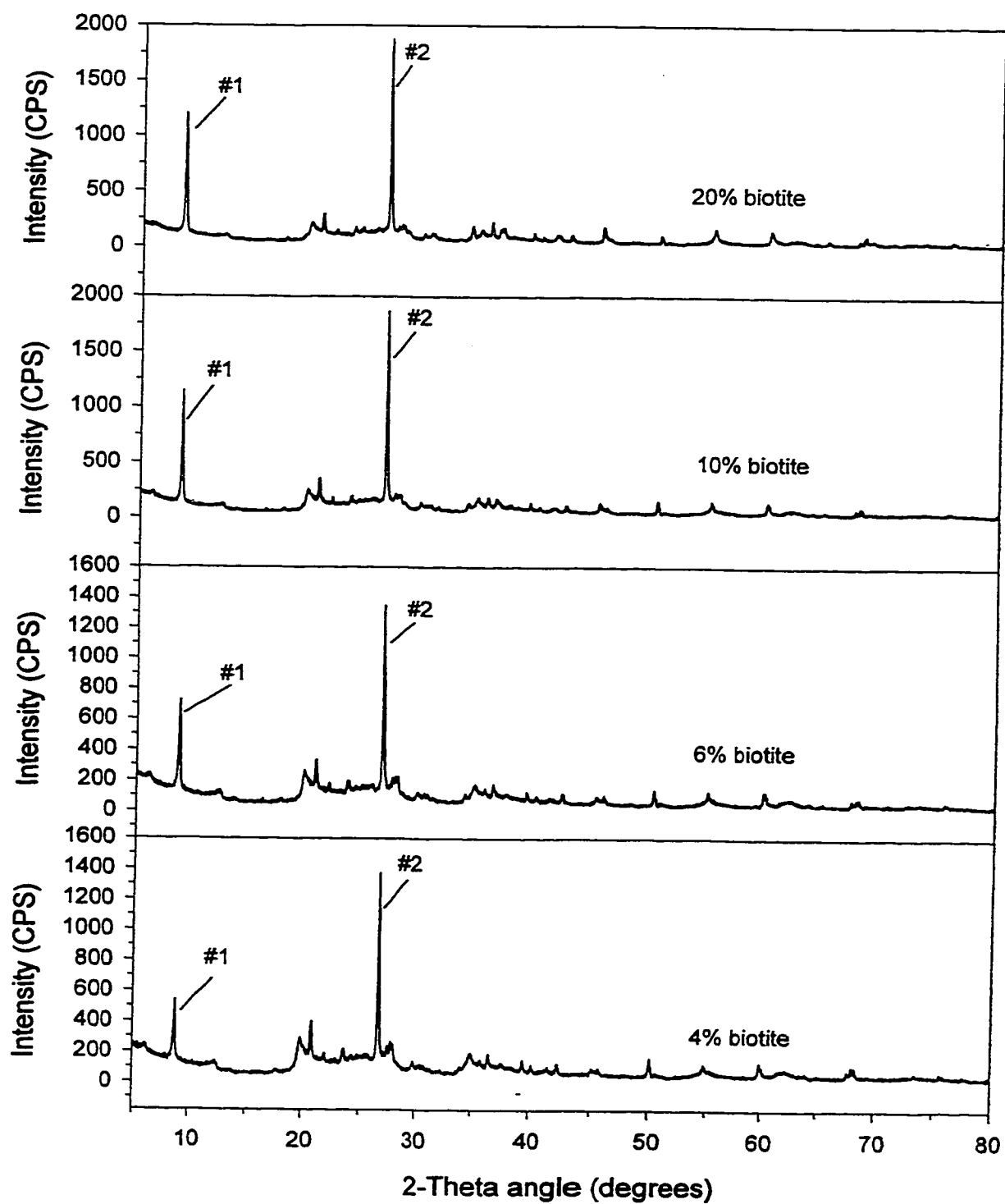


Figure 5.6 - XRPD of matrix plus biotite at various percent concentrations

5.3 Ability of the method to identify minerals in the presence of other minerals.

To test the ability of the search method to identify minerals present in a pattern containing several minerals at detectable levels, a peak list of a sample was modeled. The modeled list was generated by combining the peak lists of several minerals (quartz, albite, augite, and biotite) that were considered likely to be present in the real samples from the tephra layers.

The peak list for each of the mineral phases was obtained from the JCPDS file [19], and the relative intensities of the patterns were adjusted to reflect the relatively weak or strong intensities that the minerals were expected to exhibit in the real samples.

Table 5.2 contains the list of the minerals, along with the corresponding JCPDS numbers, and % intensity levels of the individual patterns. To obtain the % intensity of given mineral for this exercise, each peak in the pattern of the mineral was multiplied by the corresponding percent value. For example, if the desired intensity level was 25%, all the peaks in the pattern were multiplied by 0.25. The new relative intensities were rounded to the nearest integer.

Table 5.2 - List of minerals included in modeled pattern

Mineral name	JCPDS #	At% as entered
Quartz	33-1161	100
Albite	09-0466	80
Augite	24-0203	25
Biotite	42-1437	25

The resulting pattern was tested, as described before in chapter 2, by subtracting the best match, searching with the remaining pattern, and subtracting the best match until no peaks remained or until no good matches were reported.

The results of this test are listed in Table 5.3. The results show that all the individual minerals included in the modeled pattern were identified as being present in the mixture. Furthermore, all the minerals were identified with the appropriate At% relative intensity. These results indicate that the search method is able to differentiate components present in a complex pattern even if they show strong or weak intensities.

Table 5.3 - Minerals identified in modeled sample by search/match procedure

JCPDS #	Similarity Index	ML/X	At%	Identity
9-0466	620	39/0	82	Albite
24-0203	487	33/0	26	Augite
33-1161	334	21/0	119	Quartz
10-0493	62	10/7	10	Biotite

There were some peaks left as the remaining pattern after the search operation was finished (Table 5.4), however they were of minimum intensity and can be ignored. The remaining peaks belong to the minerals subtracted, however the substitution did not remove all the peak intensity. This effect can be attributed to the fact that At% determined by the search/match procedure did not match the input intensity exactly.

Very strong residual intensity is also observed when preferred orientation is present in the sample [9].

Table 5.4 - Remaining pattern after uPDSM search/match

d-spacing	Rel. Intensity	d-spacing	Rel. Intensity
10.05	15	1.829	3
4.570	1	1.824	14
1.851	2	1.804	4
1.844	2	1.785	6

5.4 Conclusion

The search method used to analyze the XRPD data generated in this work is suitable to the task. The method was able to differentiate minerals present in a complex pattern. The method was also able to detect important minerals in the presence of an amorphous matrix. The results also showed that the existence of low intensity peaks in a remaining pattern does not mean that there are still phases to be identified. The peaks may be just residual intensity that was not subtracted by the search/match software

CHAPTER 6

RESULTS AND DISCUSSION

TEPHROCHRONOLOGY OF THE PHILIPPI PEAT BASIN

6.1 Description of the basin

The Philippi peat basin is a 55-km² basin in eastern Greece that formed as a result of tectonic movements in the Miocene period. In this basin the peat was accumulating for 700 thousand years until recently (1944) when it was drained for agricultural use [25]. As a result, the basin is considered to contain the thickest known peatland in the world, with reserves of about 4300 million m³ of natural peat [25, 17], and also considered to be the largest fossil fuel deposit in the Balkans.

Intercalated with the peat in the basin, there are a sequence of sedimentary layers such as mud, clay, and volcanic ashes (tephra) as evidenced in the four drill cores from the basin that were part of this study.

The cores that were part of this study were identified as Ph-1, Ph-2, Ph-3, and Ph-4. Figure 6.1 shows the position of the different layers present in three of the four cores. Two of the cores (Ph-1 and Ph-2) show the presence of three layers of tephra, while the third core (Ph-3) shows the presence of only two tephra layers. The fourth core, not shown in the figure, contained only one thick layer of tephra.

The tephra layers were found at different depths within the core, depending on the length and geographical source of the core. The uppermost tephra layer was found at depths of between 3.58 m and 4.90 m from the surface; the median layer was found between 3.05 m and 5.30 m, and the lowermost layer was found between 3.35 m and 8.55

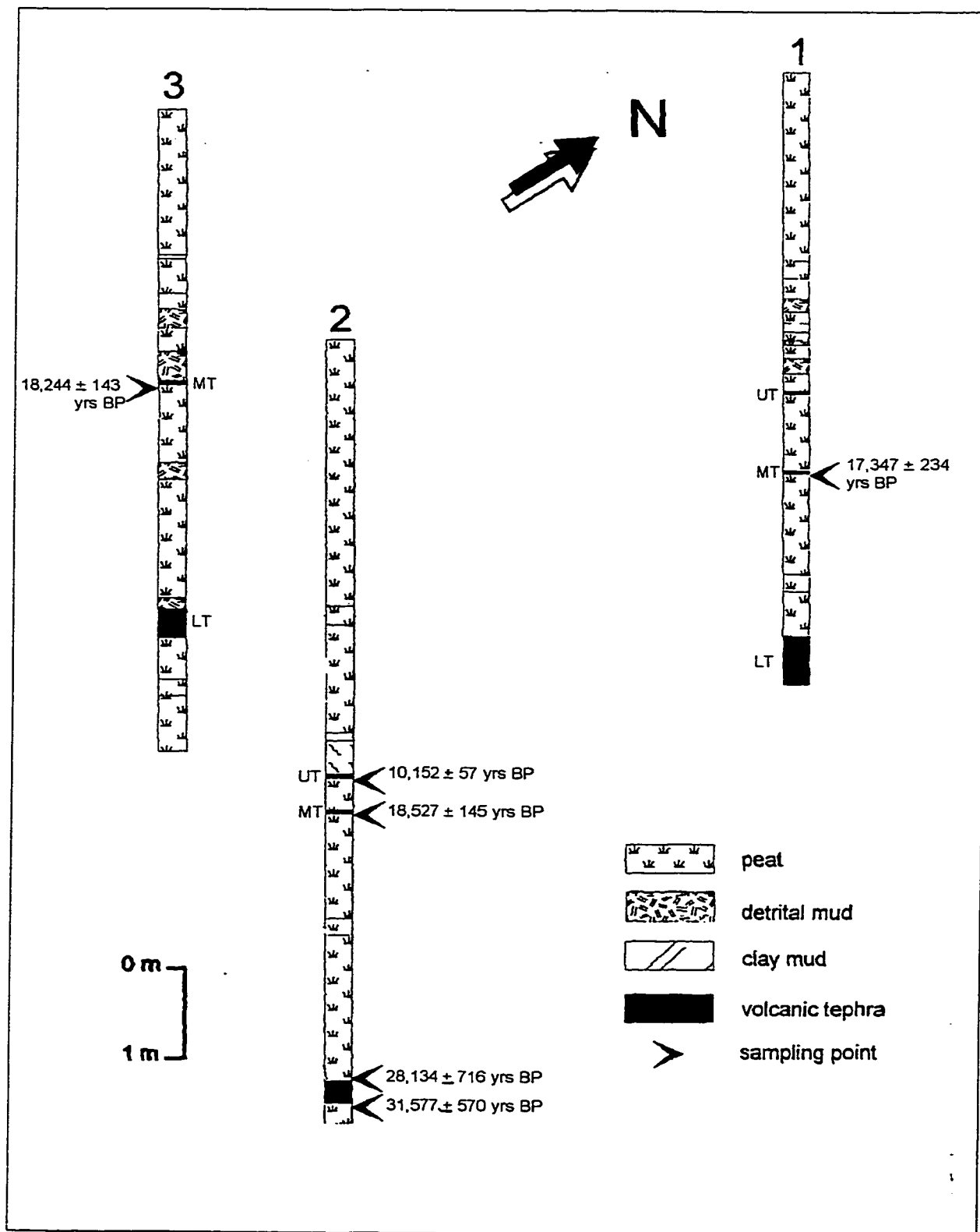


Figure 6.1 – Position and approximate ages of the tephras of in the Philippi peat cores (Adapted from St. Seymour et al. [25]).

m. (See Table 6.1). The difference in the depths of the layers could have been caused by geological processes, such as erosion and slumping, which may have altered the make up of the basin.

Table 6.1 - Tephra layers found in the cores from the Philippi Basin

Core	Tephra Layer (from top)	Depth from top (cm)
Philippi 1	1	358-362
	2	447-450
	3	630-680
Philippi 2	1	487-490
	2	528-530
	3	830-855
Philippi 3	1	305-309
	2	565-595
Philippi 4	1	330-430

6.2 Mineralogy of Tephra Layers - XRPD results

The mineralogy of the Philippi tephtras is summarized on Table 6.2. The XRPD patterns for each individual sample are include in Appendix I.

The minerals quartz and plagioclase-sodic were found in all of the Philippi samples. Minerals such as orthoclase, muscovite, plagioclase-calcic, biotite, and sanidine also appeared in many of the samples studied, but not as often as quartz and plagioclase.

Core	Layer	Quartz	Biotite	Plagioclase		Sanidine	Anorthoclase	Orthoclase	Muscovite	Microcline	Chlorochlore	Kaolinite
				sodic	calcic							
Philippi 1	358-362	x		x	x				x	x		
	447-450	x		x				x				
	630-680	x	x	x		x	x	x	x			
Philippi 2	487-490	x		x								
	528-530	x		x	x			x	x	x		
	830-855	x	x	x	x	x	x	x	x			
Philippi 3	305-309	x		x	x							
	565-595	x	x	x		x		x	x			
Philippi 4	330-430	x		x		x		x	x		x	x

Table 6.2 - Mineral phases identified in the tephra from the Philippi basin

Other minerals such as augite, aegirine-augite, olivine, and hypersthene, which were expected to be present, and which have been used by other investigators as diagnostic minerals to differentiate between Hellenic and Italian volcanoes, were not detected.

However, a previous work by Christanis [5] that examined tephra layers from a nearby area found that the minerals were present only in very low concentrations. The absence of some of these diagnostic minerals from our results may be explained by the results of the sensitivity study described before in Chapter 5. In that study, it was found that if the concentration of augite, and/or biotite, present in the samples was less than ~ 10%, the X-ray diffraction and search methods used in this work would not be able to detect them and identify them.

6.3 Shard Chemistry - Electron Probe Microanalysis Results

The results from the chemical analysis of the Philippi tephra by electron probe microanalysis are summarized in Table 6.3. The values shown are the averages of several analyses. The individual analysis results for each individual tephra are included in the appendix II.

Also included in Table 6.3 are the positional designation given to each tephra within a core: upper tuff (UT) for the uppermost layer, lower tuff (LT) for the lowermost layer, and median tuff (MT) for the layer in between. The term tuff is used to designate a compacted layer of volcanic ash material. The positional designation was assigned on the relative position of the layers and on the similarity of the chemistry as explained below.

The tephra layer found in core Ph-4 was not analyzed for chemical composition

Core Layer	Philippi 1						Philippi 2				Philippi 3				Philippi 4			
	358-362	447-450	630-640	640-660	660-680		487-490	528-530	830-840	840-855	305-309	565-570	570-595		330-335	335-350	350-400	400-430
	(UT)	(MT)	(LT)	(LT)	(LT)		(UT)	(MT)	(LT)	(LT)	(MT)	(LT)	(LT)					
SiO ₂	72.02	71.95	61.18		61.40		71.89	71.72	61.64	61.65	71.84	61.13	61.37					
TiO ₂	0.45	0.45	0.33		0.43		0.47	0.43	0.41	0.40	0.45	0.43	0.44					
Al ₂ O ₃	14.24	14.31	19.42		18.61		14.38	14.30	18.49	18.48	14.27	18.69	18.72					
FeO	3.03	3.15	2.48		2.97		2.85	3.25	2.97	3.04	3.13	3.01	2.96					
MgO	0.39	0.41	0.28		0.32		0.42	0.41	0.33	0.39	0.41	0.33	0.34					
CaO	1.80	1.67	1.41		1.71		1.71	1.70	1.68	1.80	1.69	1.71	1.72					
Na ₂ O	4.91	5.02	6.00		6.79		5.15	5.05	6.80	6.13	5.11	6.90	6.16					
K ₂ O	2.78	2.66	7.83		6.72		2.73	2.70	6.65	7.20	2.68	6.74	7.30					
Total	99.63	99.62	98.93		98.95		99.60	99.56	98.97	99.09	99.59	98.93	99.01					

Table 6.3 - Average major element composition of samples from the Philippi basin

because an acceptable sample could not be obtained, but it is expected to be similar to the lowermost layers found in the other three cores. This assumption was made based on the relative position of the layer with respect to the other material found in the core.

The results listed in Table 6.3 reveal the existence of two compositional groups among the tephra layers: one group with SiO_2 levels of about 60%, and another one with SiO_2 levels of about 70%.

The lower tuff (LT) is consistently lower in SiO_2 and richer in K_2O in all the cores, while the upper and middle tuffs (UT and MT) are richer in SiO_2 and poorer in K_2O . The similarity in the chemical composition of the upper and middle tuffs across the cores indicates that they may have a common origin, which may be different from the origin of the lower tuff.

6.4 Approximate ages of the Philippi tephtras

The difference in depths of the layers in the cores is indications that the tephtras may have been deposited during different chronological periods. The approximate ages established for the upper, middle, and lower tephra layers are listed on Table 6.4. These dates were obtained by ^{14}C dating of the peat layers in contact with tephra layers.

The approximate age of the upper tuff was established to be between close to 10 thousand years by ^{14}C dating of the peat layer immediately below the tephra. The approximate age of the median tuff was found to be between 17 and 18 thousand years by dating of the peat layer immediately below the tephra layer. The approximate age of the lower tuff was established by ^{14}C dating of the peat layers immediately above and below the tephra layer. The measurements yielded minimum approximate ages of 28 to 31

thousand years.

Table 6.4 -Approximate ages of the identified tephra layers from the Philippi peat basin

Layer	Sample #	Sampling depth (cm)	Sampling position	Approximate Age B.P. (yrs) *	Type of sample analyzed	Dating method used
Upper tuff	Philippi 2	495-500	Below UT	10152 ± 57	Peat	^{14}C
Middle Tuff	Philippi 1	455-460	Below MT	17347 ± 234	Peat	^{14}C
Middle Tuff	Philippi 2	530-535	Below MT	18527 ± 145	Peat	^{14}C
Middle Tuff	Philippi 3	310-315	Below MT	18244 ± 143	Peat	^{14}C
Lower Tuff	Philippi 2	825-830	Above LT	28134 ± 716	Peat	^{14}C
Lower Tuff	Philippi 2	860-865	Below LT	31577 ± 570	Peat	^{14}C

* B.P. = Before present

6.5 Shard morphology

The morphology of the glass and pumice shards that make up the Philippi tephra is illustrated on figures 6.2, 6.3, and 6.4. These figures represent the tephra from the upper tuff (UT), the median tuff (MT), and the lower tuff (LT), respectively.

In general, the glass shards that were present in UT, MT, and LT, were Y-shaped, or cusped, indicating that they were the remnants of bubble junctions. The particles were clear in color. The pumice shards were also clear, and exhibited the small, elongated cavities enclosed by glass walls.

The morphology of the glassy components of the tephra indicates that the deposits originated from high viscosity lavas that resulted in large-scale ash eruptions (Plinian eruptions). The fact that both types, bubble walls and pumice shards, are present



Figure 6.2 – SEM micrographs of glassy fragments from the upper tuff (UT) of Philippi

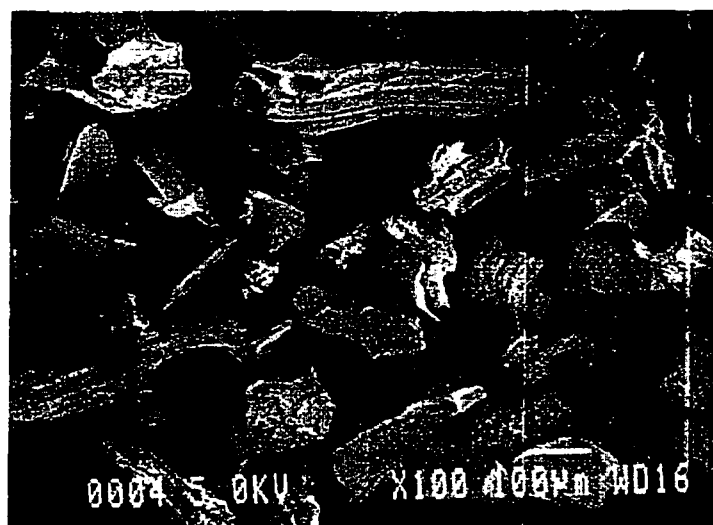
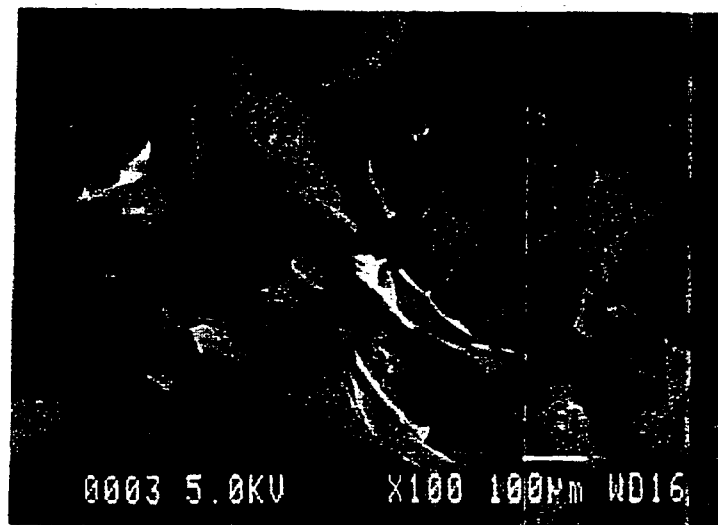


Figure 6.3 - SEM micrographs of glassy fragments from the middle tuff (MT) of Philippi

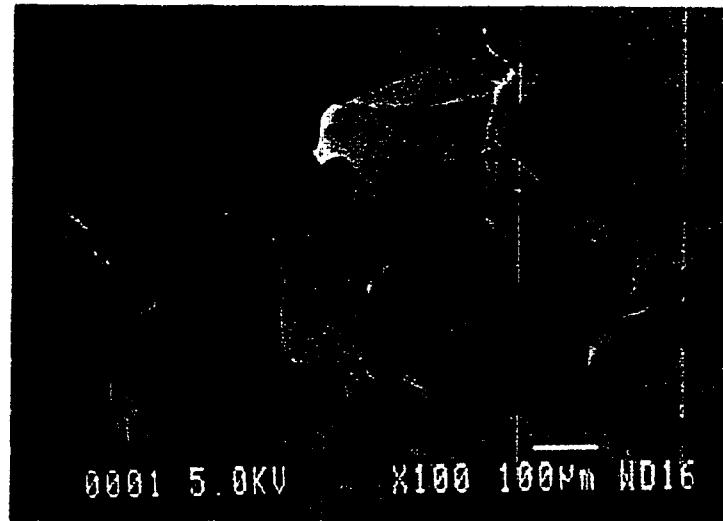


Figure 6.4 – SEM micrographs of glassy fragments from the lower tuff (LT) of Philippi

in the deposits indicates that the temperature of the melt may have been near 850 °C, and that the viscosity of the melt varied during the eruptive episodes.

6.6 Identification of Tephra Layers

The identification of tephra layers is usually done using the mineralogy, chemical composition, and age of the unknown tephtras to correlate to similar data found in the literature. In the case of the Philippi tephtras, however, some of the expected diagnostic minerals like hypersthene, augite, and aegirine-augite, were not detected in any of the samples, and could not be used in the correlation to differentiate between Hellenic and Italian volcanoes. Therefore, most of the identification of the Philippi tephtras was done using only the chemical composition and the approximate ages of the tephra layers.

The only diagnostic minerals that were detected were biotite and sanidine, which were found in the lowermost layers of each core. Both of these minerals are typical of minerals from the Campanian area of Italy (see Table 3.1 in Chapter 3), and indicate that the lowermost layer in each of the cores probably originated from that area.

Several investigators have studied marine deposits from the Mediterranean and Tyrrhenian seas and have correlated them with distinct pyroclastic deposits on land [14, 23, 19, and 18]. While doing the correlation, they have found that chemical composition is the most useful quantitative method for correlating ashes having distinct source areas [14].

In a study of tephra layers from the Mediterranean, Keller [14] has grouped the identified and correlated tephtras according to the ratios of alkali oxides to alkali oxides plus calcium oxide, versus the %SiO₂ content. Plotting a similar graph using the

composition of the tephtras from the upper, middle, and lower tuffs of the Philippi samples (Figure 6.5) was helpful in locating a general area of origin for the tephtras. The graph showed that the upper and median tuffs had similar characteristics to the rhyolitic, calc-alkalic ash layers from the Hellenic arc, while the lower tuff had similarity to the alkalic, trachytic ash layers from the Italian provinces.

Tables 6.5 and 6.6 show the direct comparison between the major element chemistry of the upper, median, and lower tuffs, and that of ash layer that show very close correlation: the Akrotiri layer for the upper and median tuffs, and the Campanian layer for the lower tuff, respectively.

The ternary graphs that were constructed for the tephra layers of the upper, median, and lower tuffs shown on Figures 6.6, 6.7, and 6.8, respectively. A comparison of these figures with the Figure 3.1 of Chapter 3 confirmed the correlation obtained through the direct comparison of the major element chemistry: the tephtras of the upper and median tuffs of Philippi plotted in the same area as those from the Akrotiri layer, while the tephtras from the lower tuff plotted in the same area as those from the Campanian layer.

Further confirmation was obtained when the chemical composition of the tephtras was tested by the statistical method. The similarity matrix constructed is shown on Table 6.7. The lowest %CV values of the comparison between the upper and middle tuffs were shown by the layers of the Akrotiri layer, while lowest %CV values for the lower tuff were shown by layer corresponding to the Campanian ignimbrite.

The Minoan and Akrotiri layers both originate from the island of Santorini, an island in the eastern Mediterranean. Located on this island is Thera, the most active and

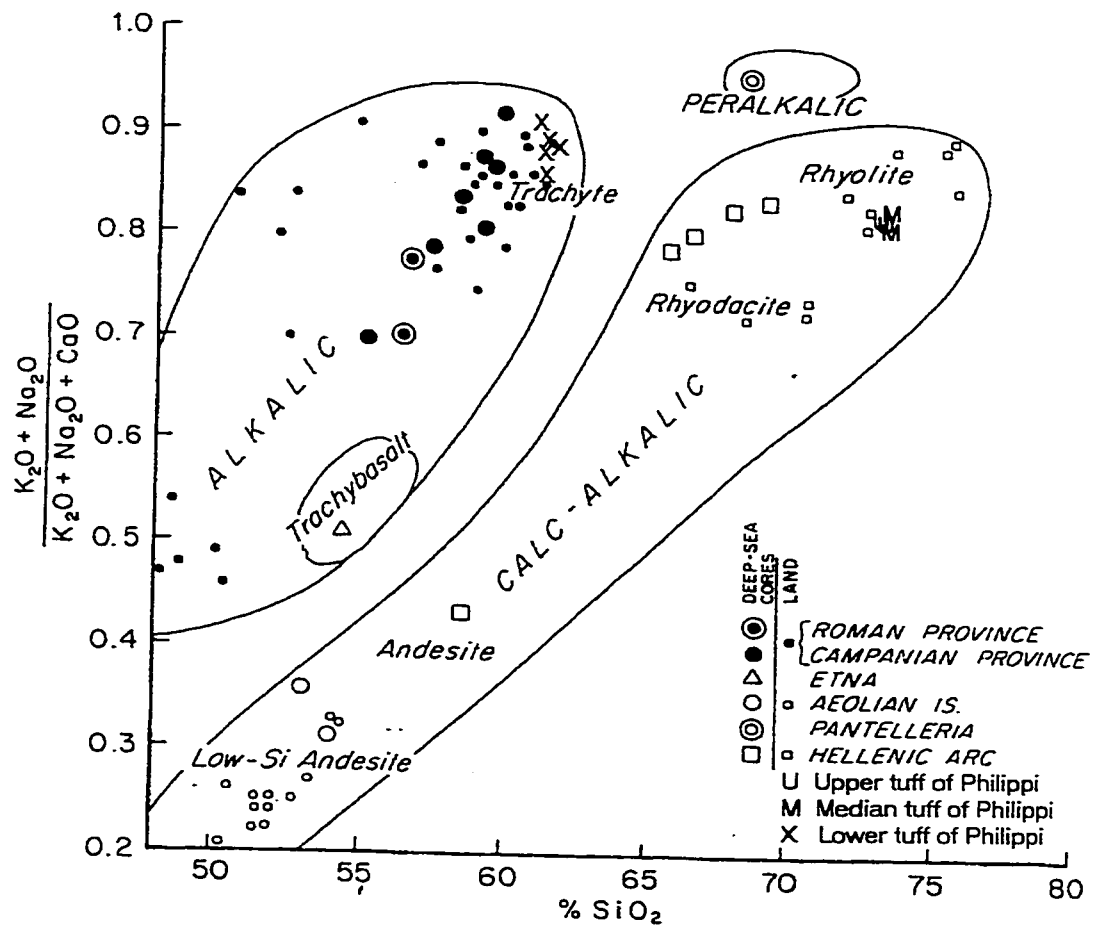


Figure 6.5 – Distinctive groupings of various ash layers according to ratios of alkali to calcium. (Adapted from Keller, [14]).

violently explosive volcano in the Hellenic arc. There have been several eruptive episodes of this volcano. One of them, which occurred about 3650 years ago, is thought to have deposited what is known as the Minoan tuff, and to have helped to end the Minoan civilization. A second episode is thought to have occurred approximately

	Akrotiri (1)	Philippi upper tephra		Philippi median tephra		
		PH-1 358-362	PH-2 487-490	PH-1 447-450	PH-2 528-530	PH-3 305-309
SiO ₂	72.10	72.02	71.89	71.95	71.72	71.84
TiO ₂	0.46	0.45	0.47	0.45	0.43	0.45
Al ₂ O ₃	13.90	14.24	14.38	14.31	14.30	14.27
FeO	2.83	3.03	2.85	3.15	3.25	3.13
MgO	0.41	0.39	0.42	0.41	0.41	0.41
CaO	1.56	1.80	1.71	1.67	1.70	1.69
Na ₂ O	4.43	4.91	5.15	5.02	5.05	5.11
K ₂ O	3.14	2.78	2.73	2.66	2.70	2.68
Total	98.83	99.63	99.60	99.62	99.56	99.59

(1) From Federman and Carey [10]

Table 6.5 - Comparison of major element composition of glass shards from Philippi and from Akrotiri

	Campanian Ignimbrite				Philippi Lower Tephra					
					PH-1	PH-2	PH-2	PH-3	PH-3	
	A	B	C	D	660-680	830-840	840-855	565-570	570-595	
SiO ₂	61.40	61.21	60.16	62.30	61.40	61.64	61.65	61.13	61.37	
TiO ₂	0.42	0.42	0.38	0.46	0.43	0.41	0.40	0.43	0.44	
Al ₂ O ₃	18.67	18.65	19.98	18.98	18.61	18.49	18.48	18.69	18.72	
FeO	3.35	3.52	3.03	3.25	2.97	2.97	3.04	3.01	2.96	
MgO	0.47	0.36	0.09	0.35	0.32	0.33	0.39	0.33	0.34	
CaO	2.03	1.60	3.43	1.62	1.71	1.68	1.80	1.71	1.72	
Na ₂ O	5.49	5.18	4.12	5.51	6.79	6.80	6.13	6.90	6.16	
K ₂ O	7.28	7.66	8.92		6.72	6.65	7.20	6.74	7.30	
Total	99.11	98.60	100.11	92.47	98.95	98.97	99.09	98.93	99.01	

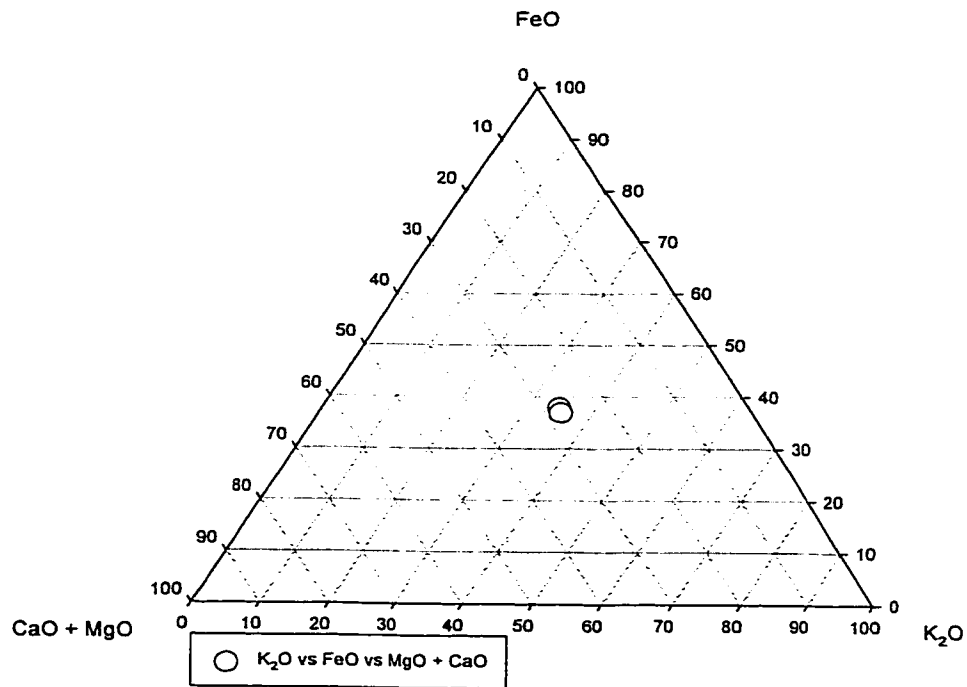
(A), (B) From Civetta et al. [6]
 (C) From Pateme et al. [19]
 (D) From St. Seymour and Christianis [24]

Table 6.6 - Comparison of major element composition of glass shards from Philippi and the Campanian Ignimbrite

Philippi Sample	Layer	Identified layer					
		M	S	Y	C	X	S
PH-1 358-362	Upper tuff	25.5	6.3	27.0	30.7	48.8	101.0
PH-1 447-450	Median tuff	26.6	7.5	29.0	31.5	48.6	103.0
PH-1 630-640	Lower tuff	37.8	60.2	42.6	12.3	99.9	81.3
PH-1 640-680	Lower tuff			NOT MEASURED			
PH-1 660-680	Lower tuff	26.4	42.4	32.8	8.2	84.5	86.3
PH-2 487-490	Upper tuff	26.1	7.1	25.3	31.3	49.4	104.4
PH-2 528-530	Median tuff	26.0	7.2	29.6	30.8	48.9	102.2
PH-2 830-840	Lower tuff	25.7	42.2	32.6	6.8	84.4	86.8
PH-2 840-855	Lower tuff	26.1	43.0	33.0	6.3	85.1	86.8
PH-3 305-309	Median tuff	26.6	7.1	28.6	31.4	48.6	103.1
PH-3 565-570	Lower tuff	26.3	42.4	33.0	7.7	84.5	86.5
PH-3 570-595	Lower tuff	29.7	47.1	34.3	8.5	89.3	88.6

Table 6.7 – Correlation of tephra layers from the Philippi basin by coefficients of variation.

**Figure 6.6 - Ternary plot of the
tephra layers from the upper tuff of Philippi**



**Figure 6.7 - Ternary plot of the
tephras from the middle tuff of Philippi**

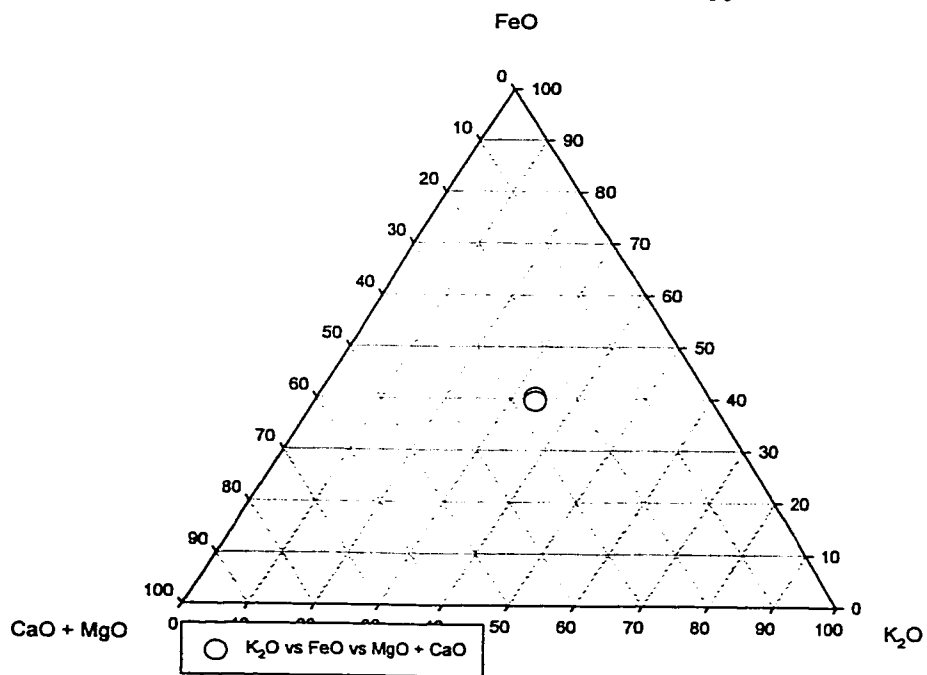
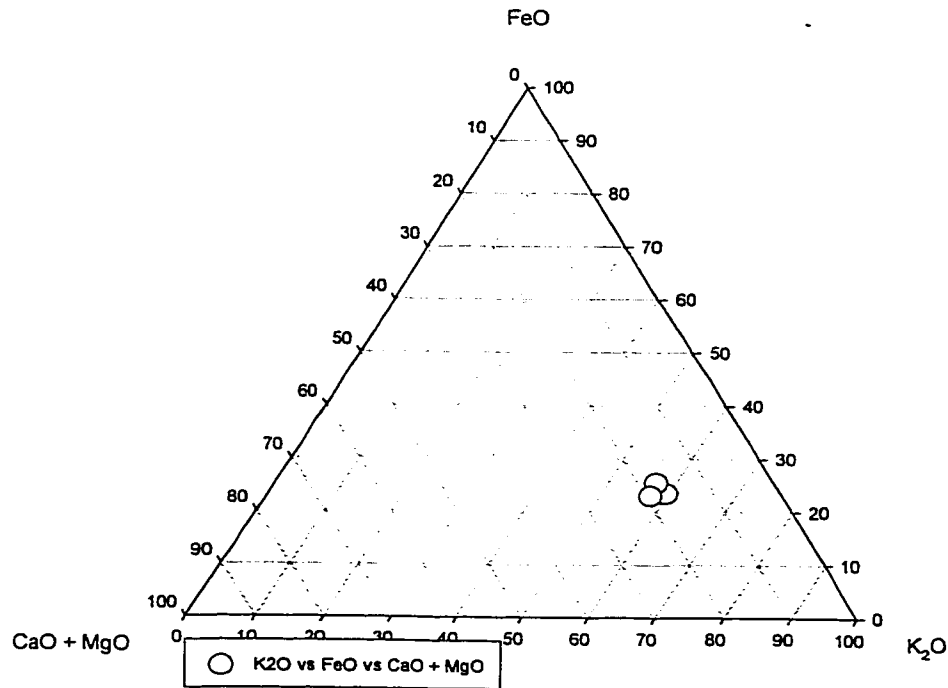


Figure 6.8 - Ternary plot of the tephra layers from the lower tuff of Philippi



10 thousand yr. BP and to have deposited the Santorini turbidite [14]. A third episode of activity is occurred at the Akrotiri vent and is thought to have deposited the Akrotiri ignimbrite approximately 18000 yr. ago.

The approximate age of the upper tuff (~10 thousand years) shows good correlation to the period of occurrence of the Santorini turbidite of about 10,000 yrs ago, while the age of the middle tuff (17-18 thousand years) shows good correlation to the explosion at the Akrotiri vent of about 18000 years ago.

The Grey Campanian tuff is a voluminous tephra in the Campanian and Neapolitan region that is thought to have originated from the Campanian volcanic province in Italy. The Campanian tuff has been dated as having been deposited during a

volcanic event that occurred 28-38 thousand years ago [1], and which covered at least 7000 km². This approximate age is close to the approximate age of the layers that are part of the lower tuff (28-30 thousand years).

6.7 Summary

The tephras from the Philippi peat basin were composed of glass shards, pumice shards, and mineral fragments. The tephras were found to be part of three different layers of compacted ash, or tuffs, within the cores. The upper tuff (UT) was 3-4 cm thick, with an approximate age of 10 ka. The median tuff (MT) was 2-4 cm thick, with an approximate age of about 18 ka. The lower tuff (LT) was 25-100 cm thick, with an approximate age of 28-30 ka.

The glass shards found in these tephras were cusped. The pumice shards contained small, elongated vesicles. The morphology of the glass and pumice shards indicates that the eruptions that gave rise to these volcanic deposits were plinian, and that the magmas involved in the eruptions were high-viscosity magmas.

The mineral fragments that were detected by the XRD and search/match methods included quartz, biotite, sodic plagioclase, calcic plagioclase, sanidine, anorthoclase, orthoclase, muscovite, microcline, chloritoid, and kaolinite. Other minerals that were expected to be in the samples were not detected, possibly because they were present at concentrations below the detection limit of the method.

The study of the mineralogy of the Philippi tephras did not provide a spectrum of minerals that could be used in the identification of all of the tephras. Only the tephras from the lower tuff contained some diagnostic minerals. Based on some of the

mineralogy results, the chemical composition, and approximate ages of the tephra layers, the following correlation is proposed:

- a) The upper tuff is correlated to the Santorini turbidite ash layer, which is believed to originate from the eruption of the Akrotiri vent of Thera on the island of Santorini approximately 10,000 years before present.
- b) The middle tuff is correlated to the Akrotiri ignimbrite, which is believed to originate from the eruption of the Akrotiri vent of Thera on the island of Santorini approximately 18,000 years before present.
- c) The lower tuff is correlated to the Campanian ash layer, which is believed to have originated from volcanoes in the Campanian and Neapolitan regions of Italy approximately 28-30 thousand years ago.

CHAPTER 7
RESULTS AND DISCUSSION
TEPHROCHRONOLOGY OF THE MYRTÖÖN BASIN.

7.1 Description of the Basin

The Myrtöön Basin is a deep basin in the southwestern part of the Aegean Sea in the eastern Mediterranean. Several cores were collected from this basin as part of a project sponsored by the electric power company of Greece, which was mapping the bottom of the sea in order to lay down cable to provide electricity to the islands in the area. Contained in these cores were sections of volcanic ashes mixed with sand and plankton material.

The tephra that were found in five of the cores were studied for this work. The cores were identified as core 18, core 20, core 37, core 39, and core 40. Table 7.1 describes the cores and their respective tephra deposits. The table lists the location in the basin from which the cores were taken, along with their length. Also included in this table is the thickness of the individual sections.

The mineralogy and chemical composition of these ash deposits were determined by X-ray diffraction and electron probe microanalysis, respectively. The age of the deposits in one of the cores was determined by ^{14}C radio-dating method by Geraga et al. [12], the approximate age of the deposits in the rest of the cores was not established

Core #	Location in Basin	Length of Core (cm)	Depth of water (m)	Sample #	Depth of sample from sea (cm)
18	Slope of St-George	191	480	MYR 18/12 MYR 18/13	147-149 153-155
20		210	836	MYR 20/1 MYR 20/2 MYR 20/3	12-14 34-37 60
37	Slope near volcanoes Milos - Antimilos	180	570	MYR 37/5	110
39	Central part of Myrtoon basin	165	905	MYR 39/2	40
40		219	933	MYR 40/2 MYR 40/7	34-36 125-127

Table 7.1 - Location and depth of tephra deposits from the Myrtöön basin

7.2 Mineralogy of the tephra deposits

The mineralogy of the Myrtöön tephra, as determined by our X-ray diffraction method, is described in Table 7.2. The XRPD patterns are included in Appendix I.

The most prevalent mineral phases found were quartz, sodic plagioclase, muscovite, and chloritoid. These minerals were present in almost all samples examined. Some of the samples also contained sanidine, orthoclase, and microcline. Augite, calcic plagioclase, and sanidine were found in only one sample each.

As in the case of the Philippi tephra, some of the diagnostic minerals such as augite, aegirine-augite, biotite, and hypersthene, that can be used to differentiate between Hellenic and Italian volcanoes, were not identified in most of the samples by our methods of analysis. It is possible that these diagnostic minerals are present in the tephra, but only at low levels. Again, the inability of the method to identify minerals at low levels may be the reason for the absence of these minerals from our results.

7.3 Shard Chemistry - Electron Microprobe Results

The chemical composition of the glassy fragments of the Myrtöön tephra is presented in Table 7.3. The values in this table represent the average of several analyses. The individual analyses are included in Appendix II.

The chemistry of the tephra deposits seems to be the same within each of the cores. There seems to be two general groupings of chemistry types among the tephra: the first group is the calc-alkalic, rhyolitic tephra that were found in cores 18, 39, and 40. These tephra have a %SiO₂ content of 71-76% with a percent K₂O

Core	Layer	Quartz	Augite	Plagioclase		Sanidine	Orthoclase	Muscovite	Microcline	Chinolchlore
18	18/12	x			x			x		x
	18/13	x			x			x	x	
20	20/1	x			x			x		x
	20/2	x			x	x		x		
	20/3	x			x			x		x
37	37/1	x			x		x			x
	37/5				NOT AVAILABLE	NOT AVAILABLE	NOT AVAILABLE	NOT AVAILABLE		
39	39/1	x			x			x		x
	39/2		x		x					
40	40/2	x						x		x
	40/7	x			x			x		x

Table 7.2 - Mineral Phases identified in the tephra deposits from the Myrtöön archipelago.

Core Layer	18		20				37		39		40	
	MYR 18/12	MYR 18/13	MYR 20/1 MYR 20/2 MYR 20/3				MYR 37/1	MYR 37/5	MYR 39/1	MYR 39/2	MYR 40/2	MYR 40/7
SiO ₂	72.15	71.15	61.62	61.82	62.09		59.64	61.65		74.27	74.55	59.45
TiO ₂	0.50	0.47	0.42	0.44	0.38		0.42	0.41		0.29	0.29	0.43
Al ₂ O ₃	14.07	14.69	18.51	18.58	18.49		19.63	18.53		13.78	13.72	20.32
FeO	3.10	3.38	2.97	2.96	2.89		3.04	2.94		2.08	2.10	3.43
MgO	0.41	0.44	0.37	0.33	0.39		0.35	0.32		0.29	0.28	0.44
CaO	1.63	1.77	1.76	1.62	1.82		1.68	1.63		1.40	1.39	1.68
Na ₂ O	5.00	4.94	6.48	6.65	5.62		7.71	6.70		4.36	4.21	6.40
K ₂ O	2.74	2.66	6.90	6.48	7.49		6.38	6.76		3.10	3.06	6.98
Total	99.60	99.49	99.02	98.88	99.17		98.85	98.93		99.58	99.60	99.13

Table 7.3 - Average major element composition of tephra from the Myrtöön basin

content of about 2-3%. These tephtras have been found to be characteristic of the tephtras from the Hellenic arc. The second group is made up by the tephtras from cores 20 and 37, which are classified as alkalic-trachytic tephtras. These tephtras have percent SiO₂ content of about 60-62% and higher K₂O content of about 7%. This type of tephtras is characteristic of volcanoes from the Italian volcanic provinces.

7.4 Approximate age of the Myrtöön tephtras.

The approximate age of the Myrtöön tephtras is listed in Table 7.4. Not all the tephtras from Myrtöön were dated using radio-dating methods. The only tephtras that were dated with a radio-dating method were those of core 40. The approximate ages for these deposits was found to be about 3345 yr. for layer 40/2, 11959 yr. for layer 40/7 [12].

The approximate age of the tephtra deposits from core 40 was obtained by Geraga et al. [12] in a study in which they established the sedimentation rate for the Myrtöön basin by studying the plankton material found in the cores. They found that the average rate of sedimentation in the area has been 10.2 cm/1000 years. However, this value could not be used together with the position of the deposits in the other cores to estimate their approximate age because it was suspected that other processes occurring in the basin could have affected the deposition of the ashes during the volcanic explosions.

7.5 Shard Morphology

The tephtras from the Myrtöön basin were examined under the scanning electron microscope, and under an optical microscope to study their morphology. The glass shards

Table 7.4. - Approximate ages of samples from the Myrtöön basin

Core	Sample #	Approximate Age (yr. B. P.)	Dating Method
18	MYR 18/12 MYR 18/13	not determined	none
20	MYR 20/1 MYR 20/2 MYR 20/3	not determined	none
37	MYR 37/5	not determined	none
39	MYR 39/1 MYR 39/2	not determined	none
40	MYR 40/2 MYR 40/7	3345 11959	AMS ¹⁴ C AMS ¹⁴ C

B.P. = Before present

AMS ¹⁴C = Accelerator Mass Spectrometry of ¹⁴C

that were observed were clear and Y-shaped, or cusped, which indicates that they were remnants of bubble junctions. The pumice shards were also clear, with small, elongated tubular vesicles. Examples of the morphology of some of the materials are shown in Figures 7.1 and 7.2.

The morphology of the glassy components of the tephras indicates that the deposits originated from high viscosity lavas that resulted in large-scale ash eruptions (Plinian eruptions). The fact that both types, bubble walls and pumice shards, are present in the deposits indicates that the temperature of the melt may have been near 850 °C, and that the viscosity of the melt varied during the eruptive episodes.

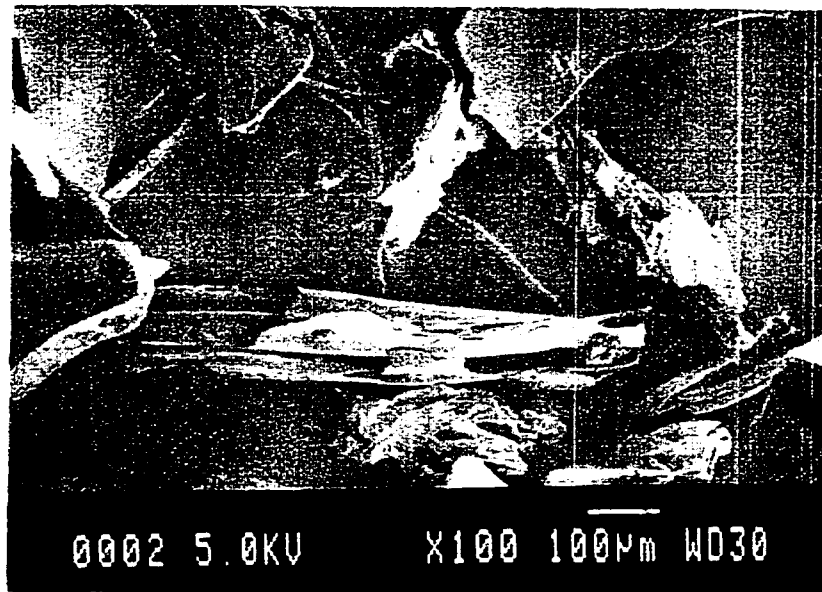
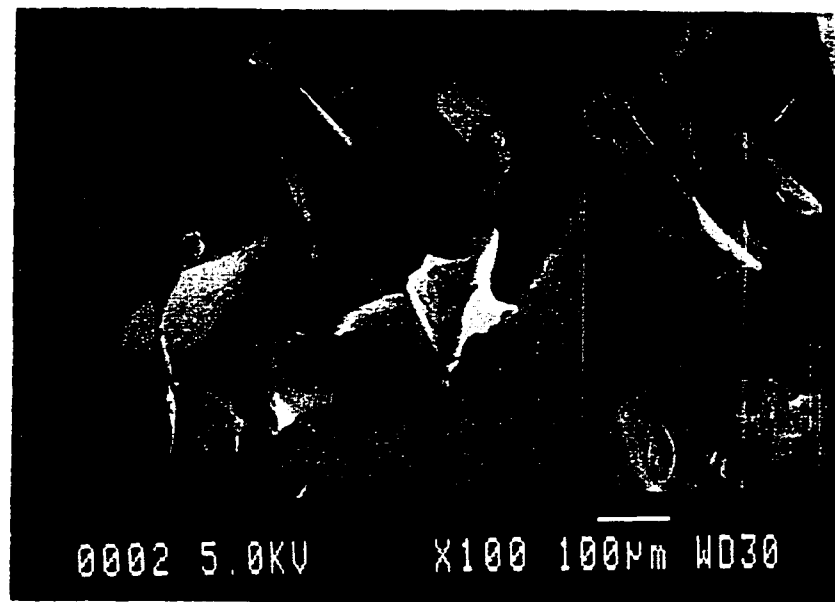


Figure 7.1 – SEM micrographs of Myrtöön tephra MYR 20/1 showing bubble wall junctions and pumice shards.

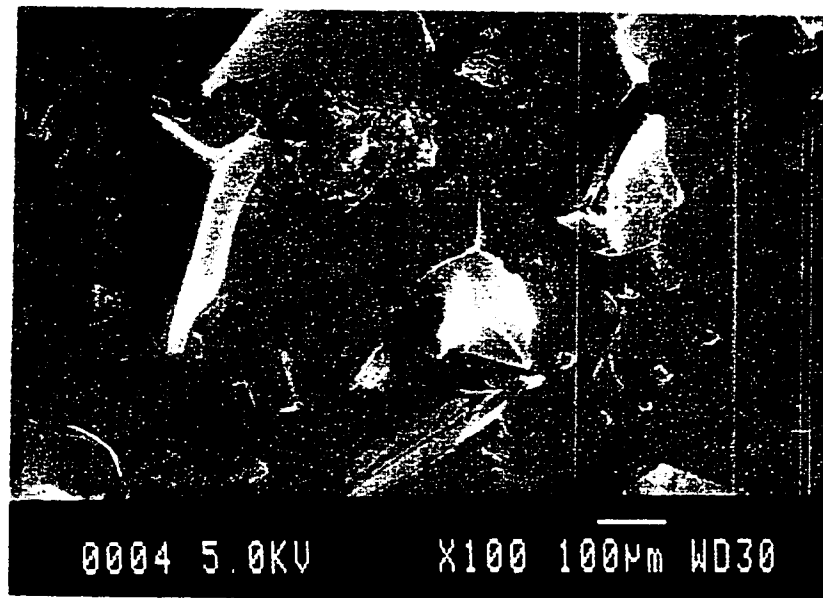
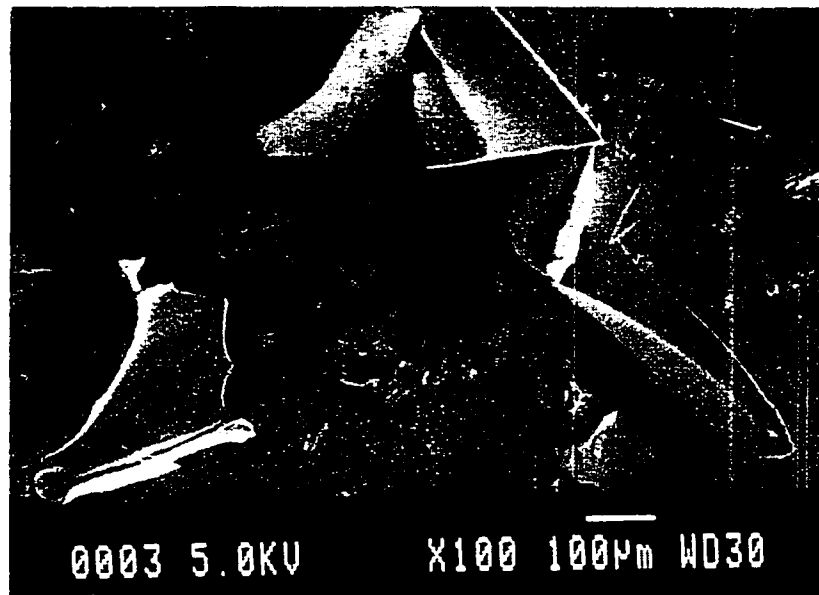


Figure 7.2 – SEM micrographs of Myrtöön tephra MYR 20/2 showing bubble wall junctions and pumice shards.

7.6 Identification of the tephra deposits.

The identification of tephra deposits is usually done using the mineralogy, chemical composition, and age of the unknown tephra to correlate to similar data found in the literature. In the case of the Myrtöön tephra, however, some of the expected minerals like hypersthene, augite, biotite, and aegirine-augite, were not detected in most of the samples, and could not be used in the correlation. Therefore the identification of the Myrtöön tephra was done using only the chemical composition, and, where available, the approximate ages, of the tephra layers.

7.6.1 Core 18

As shown in Table 7.1, core 18 contained two tephra: tephra 18/12 and 18/13. The chemistry of these tephra is comparable to that of calc-alkaline deposits from volcanoes of the Hellenic arc.

The side-to-side comparison of the major element composition of these deposits to that of the tephra from Akrotiri (Table 7.5) indicates that these two tephra may have the same origin.

When the major element composition of layers 18/12 and 18/13 was plotted on ternary graphs (Figures 7.3 and 7.4, respectively) as described before in Chapter 3, both deposits appeared to have the same composition as the deposits that originate from Akrotiri (see Figure 3.1 of Chapter 3).

The correlation by coefficient of variation (Table 7.6) showed that the greatest similarity occurred when layers 18/12 and 18/13 were compared to the chemical composition of tephra from the Akrotiri layer.

Based on the results of the shard analysis and on the graphical and statistical correlations, the tephras in layers 18/12 and 18/13 seem to have been deposited as a result of the Akrotiri vent eruption of the Thera volcano that occurred approximately 18000 yr. ago. This eruption was discussed in Chapter 6.

Table 7.5 - Comparison of major element composition of glass shards from Myrtöön and from Akrotiri.

	Akrotiri (1)	MYRTÖÖN DEPOSIT	
		MYR 18/12	MYR 18/13
SiO ₂	72.10	72.15	71.15
TiO ₂	0.46	0.50	0.47
Al ₂ O ₃	13.90	14.07	14.69
FeO	2.83	3.10	3.38
MgO	0.41	0.41	0.44
CaO	1.56	1.63	1.77
Na ₂ O	4.43	5.00	4.94
K ₂ O	3.14	2.74	2.66
Total	98.83	99.60	99.49

(1) From Federman and Carey [10].

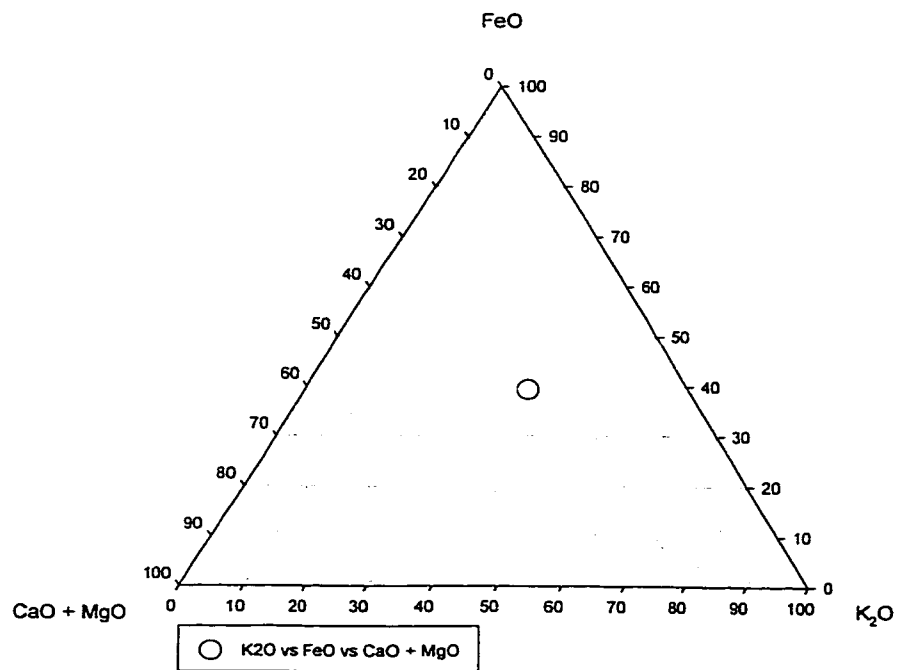


Figure 7.3 – Graphical correlation graph for Myrtöön 18/12

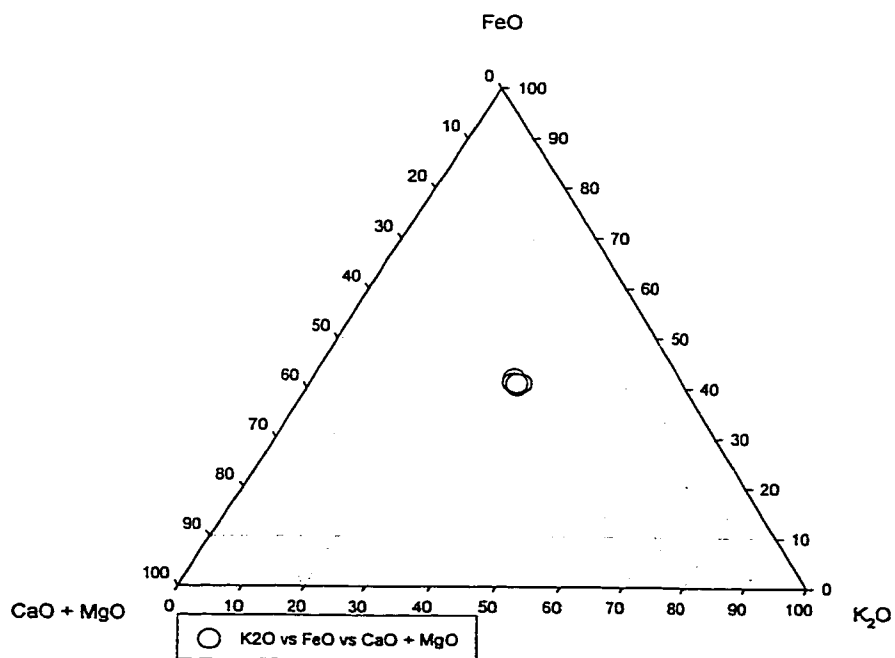


Figure 7.4 – Graphical correlation graph for Myrtöön 18/13

Myrtoon Sample	Identified Layers					
	M	S	Y	C	X	S
18/12	29.5	10.1	31.2	32.8	45.9	104.5
18/13	29.3	10.0	30.3	33.3	48.2	103.7
20/1	26.3	43.0	31.5	6.0	85.5	90.6
20/2	25.5	40.7	32.0	9.5	82.8	87.9
20/3	30.7	49.3	33.7	8.3	91.8	92.9
37/1	23.9	38.8	32.3	8.8	81.4	88.2
37/5	26.9	44.1	33.7	7.2	86.0	85.9
39/2	7.4	18.7	17.2	28.3	63.7	94.6
40/2	8.0	19.1	18.1	29.0	63.7	93.5
40/7	27.5	41.3	32.4	12.6	83.4	97.4

Table 7.6 - Correlation of tephra deposits from the Myrtöön archipelago by coefficients of variation

7.6.2 Core 20

Core 20 consisted of 3 sections: 20/1, 20/2, and 20/3 at depths of 11-12 cm, 34-37 cm, and 60 cm from the bottom of the basin, respectively. These deposits were found above sapropel 1 (a sedimentary layer which has been characterized as being approximately 7,000 years old), which makes them younger than 7 thousand years. However, the actual age of the tephra was not established

The chemistry of the three deposits is very similar to that of the alkalic-trachytic deposits of volcanoes from the Italian provinces. The side to side comparison of the major element composition of the deposits in core 20 to that of the deposits from the Italian deposits revealed their chemical similarity (Table 7.7).

The ternary plots of the chemical composition that were constructed for the three deposits are shown on Figures 7.5, 7.6, and 7.7. A comparison of these figures with Figure 3.1 suggests that all three tephra originated in the Campanian province of Italy.

The correlation by coefficient of variation shows that the three tephra are very similar to those from the Campanian province. This is shown by the fact that the lowest %CV occurs when the layers in core 20 are compared to the Campanian deposits (Table 7.6)

Patrone et al [19] constructed a chronological description of the explosive activity of the south Italian volcanoes over the past 80 thousand years from the geochemical study of marine tephra of the central Mediterranean sea. The authors found that, in marine deposits, 2 types of Campanian trachytes are observed, and that these two types show distinct alkaline content (Figure 7.8). One grouping was characterized by

	Campanian Ignimbrite				Myrtöön Deposit							
	A	B	C	D	MYR 20/1	MYR 20/2	MYR 20/3	MYR 37/1	MYR 37/5	MYR 40/7		
SiO ₂	61.40	61.21	60.16	62.30	61.62	61.82	62.09	59.64	61.65	59.45		
TiO ₂	0.42	0.42	0.38	0.46	0.42	0.44	0.38	0.42	0.41	0.43		
Al ₂ O ₃	18.67	18.65	19.98	18.98	18.51	18.58	18.49	19.63	18.53	20.32		
FeO	3.35	3.52	3.03	3.25	2.97	2.96	2.89	3.04	2.94	3.43		
MgO	0.47	0.36	0.09	0.35	0.37	0.33	0.39	0.35	0.32	0.44		
CaO	2.03	1.60	3.43	1.62	1.76	1.62	1.82	1.68	1.63	1.68		
Na ₂ O	5.49	5.18	4.12	5.51	6.48	6.65	5.62	7.71	6.70	6.40		
K ₂ O	7.28	7.66	8.92	7.03	6.90	6.48	7.49	6.38	6.76	6.98		
Total	99.11	98.60	100.11	99.50	99.02	98.88	99.17	98.85	98.93	99.13		

(A), (B) From Civetta et al [6]
(C) From Paternò et al. [19]
(D) From St. Seymour and Christianis [24]

Table 7.7 - Comparison of major element composition of glass shards from Myrtöön and the Campanian Ignimbrite

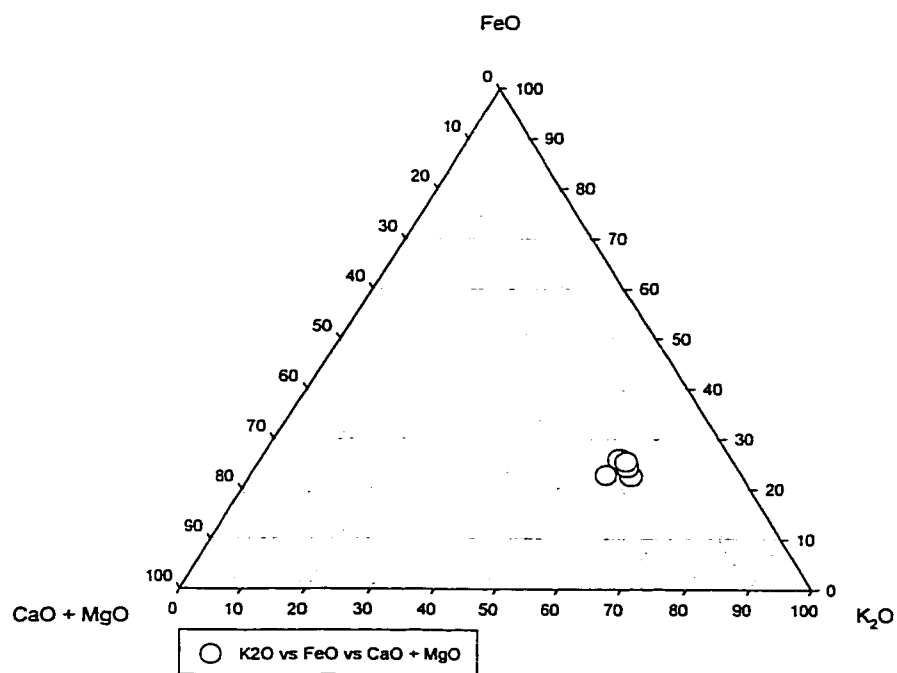


Figure 7.5 – Graphical correlation graph for Myrttöön 20/1

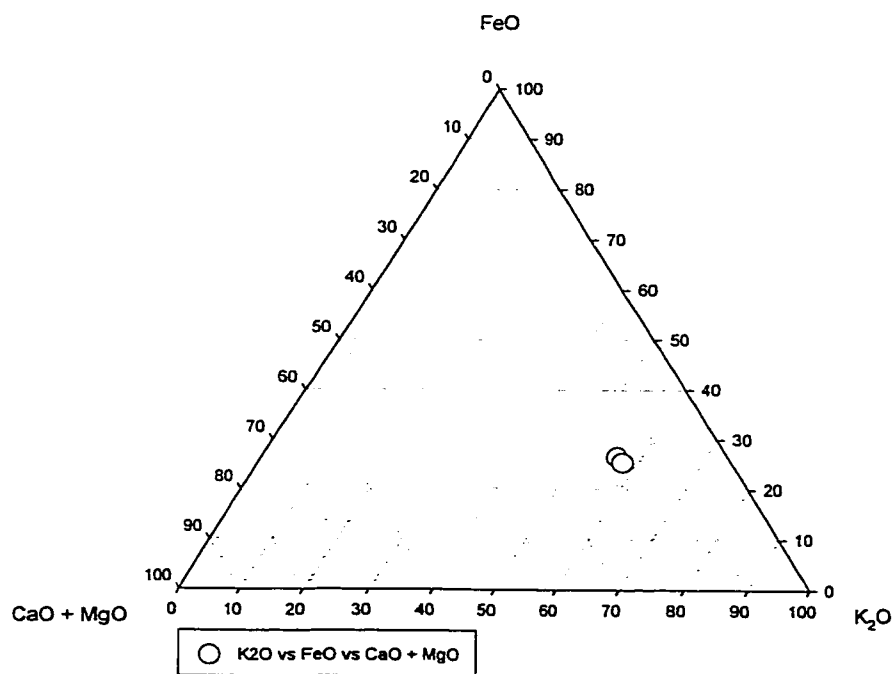


Figure 7.6 – Graphical correlation graph for Myrttöön 20/2

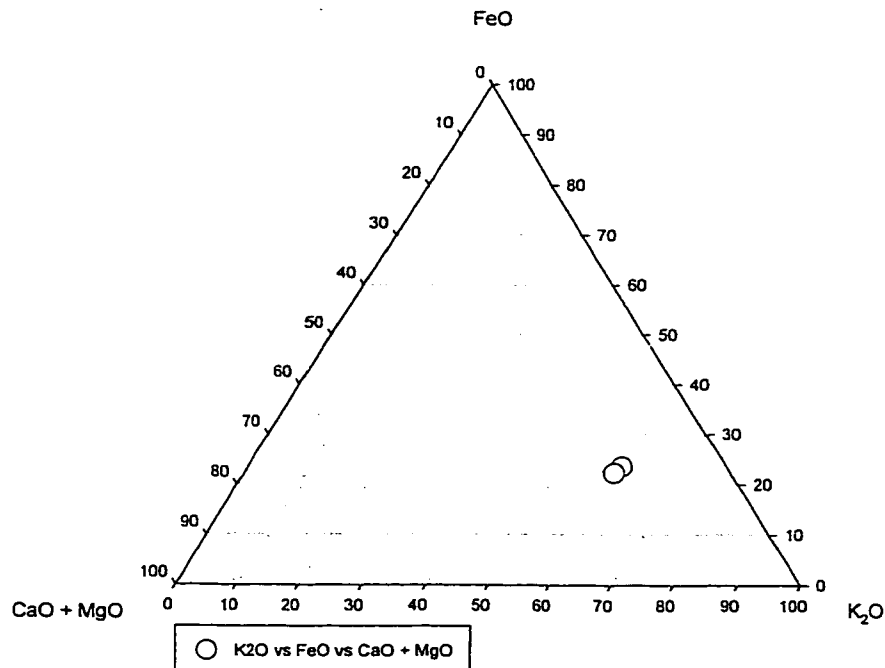


Figure 7.7 – Graphical correlation graph for Myrtöön 20/3

having lower K_2O/Na_2O ratios as compared to the same type of ratios for the second grouping.

Based on their findings, it can be seen that the tephras from core 20 are closer in composition to the deposits due to the activity on Ischia island than to those of the Phlegrean Fields (Campi Flegrei). As explained in the introductory chapter, the Ischia volcanic complex has seen many periods of activity. These periods of activity include eruptions as early as 53 thousand years ago to as late close as 100 years ago. The tephras from core 20 could have their origin in any of these eruptions.

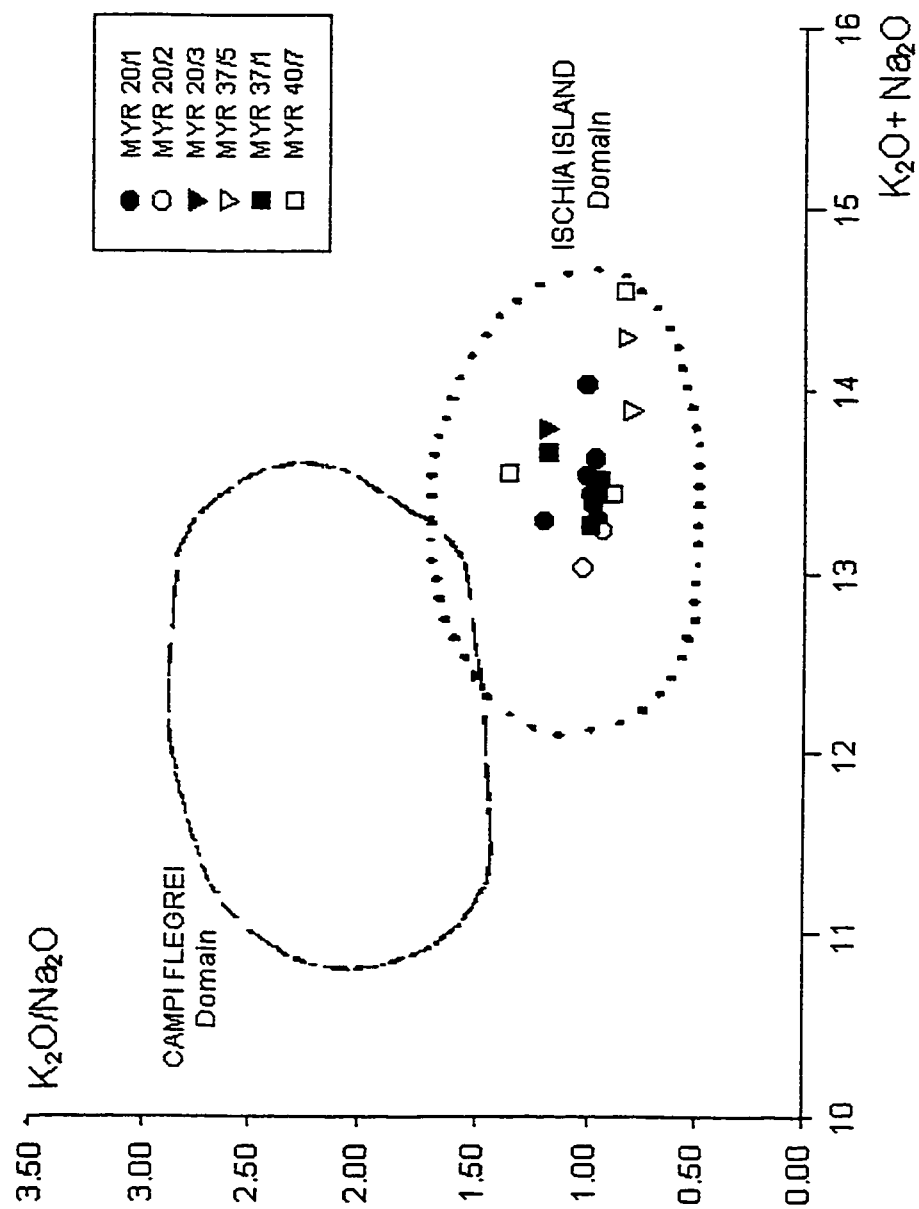


Figure 7.8 – Chemical characterization of deposits from Campanian origin by their alkali content.
(Adapted from Paternò et al. [18])

7.6.3 Core 37

Tephra 37/1

The only data available for tephra sample 37/1 was the major element composition by electron probe microanalysis. When the major element composition data was plotted on a ternary graph (Figure 7.9) and compared to Figure 3.1, the data from tephra deposit 37/1 plotted in the same area as those from the Campanian area of Italy.

The possible Campanian origin was supported by the correlation by coefficient of variation (Table 7.6), and by the side to side comparison of the major element compositions of the sample to those of tephtras from the Campanian area (Table 7.7), which also pointed to the possible origin. Figure 7.8 suggests that the deposits can be correlated to volcanic activity on Ischia Island.

Tephra 37/5

The major element composition of tephra 37/5 is very similar to that of core 37/1 above. The side-to-side comparison (Table 7.7), the major element ternary graph comparison (Figure 7.10), and the correlation by coefficients of variation (Table 7.6) all identify this tephra as coming from the Campanian area of Italy. The alkali content of this tephra classifies it as a trachyte that is believed to originate from the island of Ischia (Figure 7.8).

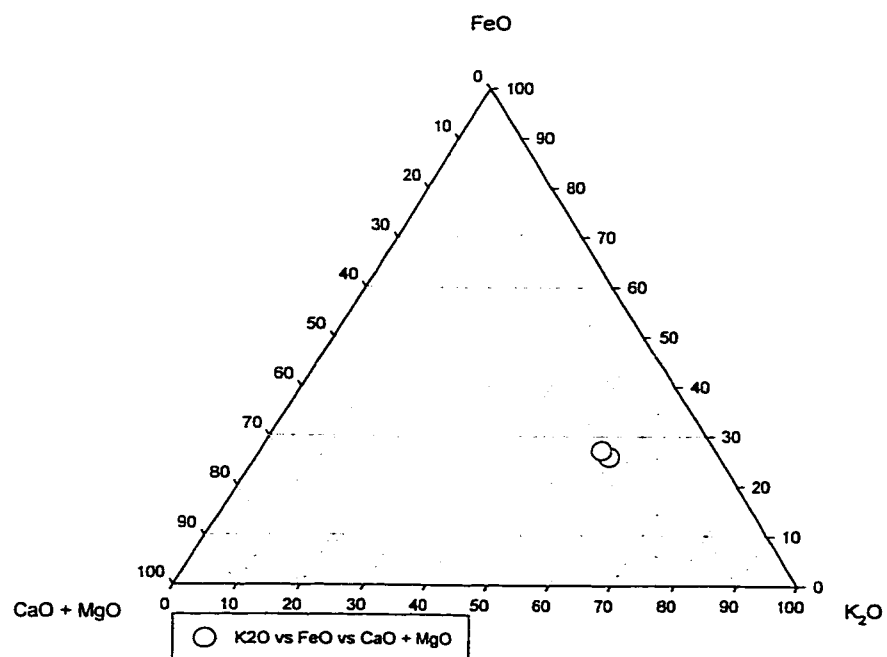


Figure 7.9 – Graphical correlation graph for Myrtöön 37/1

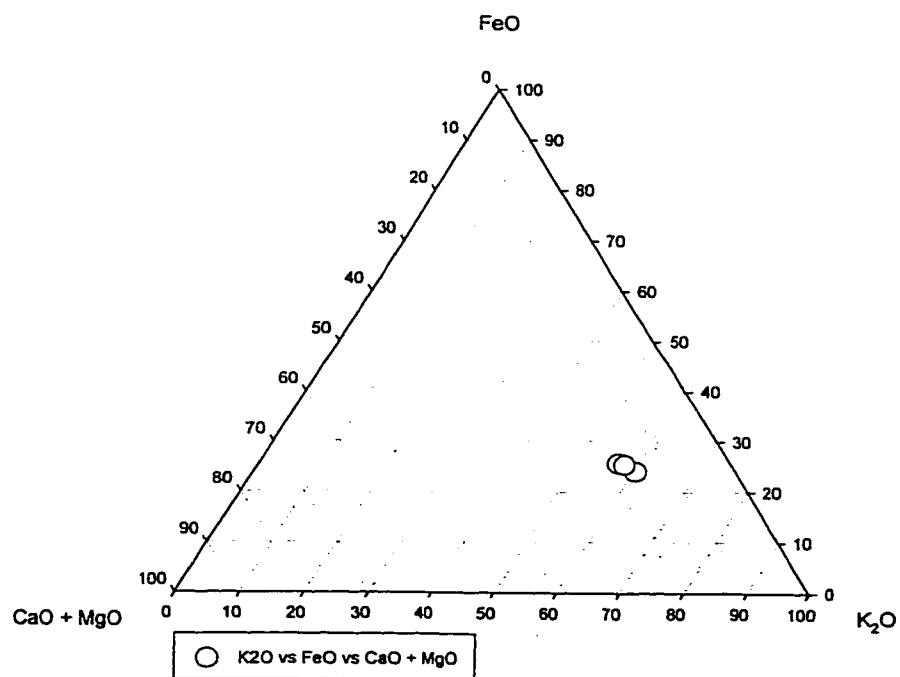


Figure 7.10 – Graphical correlation graph for Myrtöön 37/5

7.6.4 Core 39

Tephra 39/1

No data could be obtained for the chemical composition of this tephra because there were not enough glassy shards that could be used for analysis. The only data that was obtained was the mineral content by XRPD. However, as it was explained before no conclusions can be made about the possible origin of this layer based only on XRPD data.

Tephra 39/2

The major element chemical analysis of tephra 39/2 suggests that it had a Hellenic origin, considering the calc-alkaline characteristics of this tephra.

Correlation of this data through a side-to-side comparison (Table 7.8), and by coefficients of variation (Table 7.6) indicates the similarity of this deposit to the deposits that originated from the Minoan explosion of 3500 years ago. The comparison of the ternary graph plotted for layer 39/2 (Figure 7.11) with the graph of Figure 3.1. also shows that these deposits have the same chemical composition as those from the Minoan explosion.

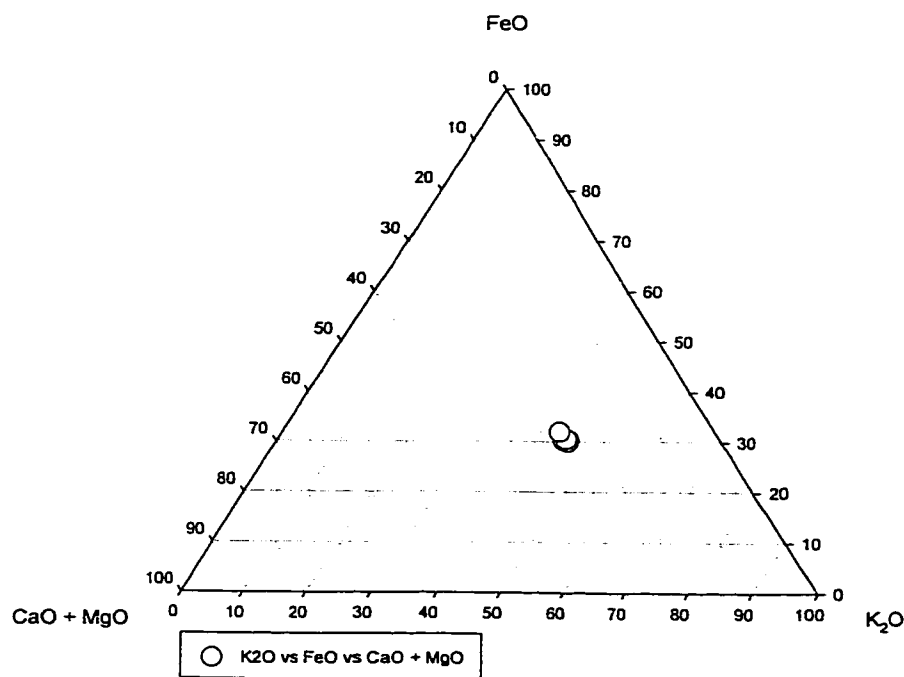


Figure 7.11 – Graphical correlation graph for Myrtöön 39/2

7.6.5 Core 40

Tephra 40/2

The approximate age of Myrtöön tephra 40/2 was found by AMS ^{14}C to be 3,345 yrs. B.P. (Table 7.4). The calc-alkaline characteristics of the tephra suggest that it had a Hellenic origin, quite possibly from the Minoan explosion of Thera due to the approximate age of the tephra.

The side-to-side comparison of the major element composition of this tephra to that of deposits from the Minoan explosion show that the tephtras are similar (Table 7.8). This conclusion is supported by the major element ternary plot that places these tephtras in the same area of the graph as the deposits of Minoan origin (Figures 7.12 and 3.1.). Also, the correlation by coefficients of variation (Table 7.6) identifies this tephra as having the same origin as the Minoan tephtras.

	Minoan Tephra Deposits				Myrtöön Deposit		
	1	2	3	4	MYR 39/2	MYR 40/2	MYR 40/125
SiO ₂	73.56	73.87	71.84	72.62	74.27	74.55	73.96
TiO ₂	0.27	0.28	0.50	0.36	0.29	0.29	0.25
Al ₂ O ₃	14.17	13.98	14.50	13.40	13.78	13.72	14.22
FeO	1.81	1.80	2.70	2.68	2.08	2.10	1.65
MgO	0.25	0.26	0.60	0.39	0.29	0.28	0.32
CaO	1.41	1.36	2.30	1.68	1.40	1.39	1.36
Na ₂ O	5.28	5.15	4.60	5.43	4.36	4.21	5.11
K ₂ O	3.25	3.30	3.00	3.42	3.10	3.06	2.64
Total	100.00	100.00	100.04	99.98	99.58	99.60	99.52

(1,2) Microprobe analyses of glass in Minoan tephra from Thera and the deep-sea cores

1 Tephra on land

2 Tephra in sea cores

From Watkins et al [29] [Tephra were recalculated to 100%]

(3) Pumice, Minoan eruption

(4) Pure volcanic glass, Minoan eruption.

(3,4) From Keller (1971). Reprinted from the Acta of the 1st International Scientific Congress on the Volcano of Thera, Athens, 15-23 Sept. 1969 (p.152-170)

Table 7.8 - Comparison of major element composition of glass shards from Myrtöön and from Minoan deposits.

Tephra 40/7

The approximate age of the Myrtöön tephra deposit 40/7 was found by AMS ^{14}C to be 11,959 yrs. B.P. (Table 7.4). The chemical composition of this tephra suggests that it had its origins in the volcanoes from the Italian peninsula.

A side-to-side comparison of this tephra shows that it is very similar to the deposits from the Campanian layers (Table 7.7). The correlation by coefficient of variation (Table 7.6), and by graphical analysis (Figures 7.13 and 3.1.) also support this conclusion. The K_2O and Na_2O content suggests that this tephra was due to activity on Ischia Island (Table 7.8).

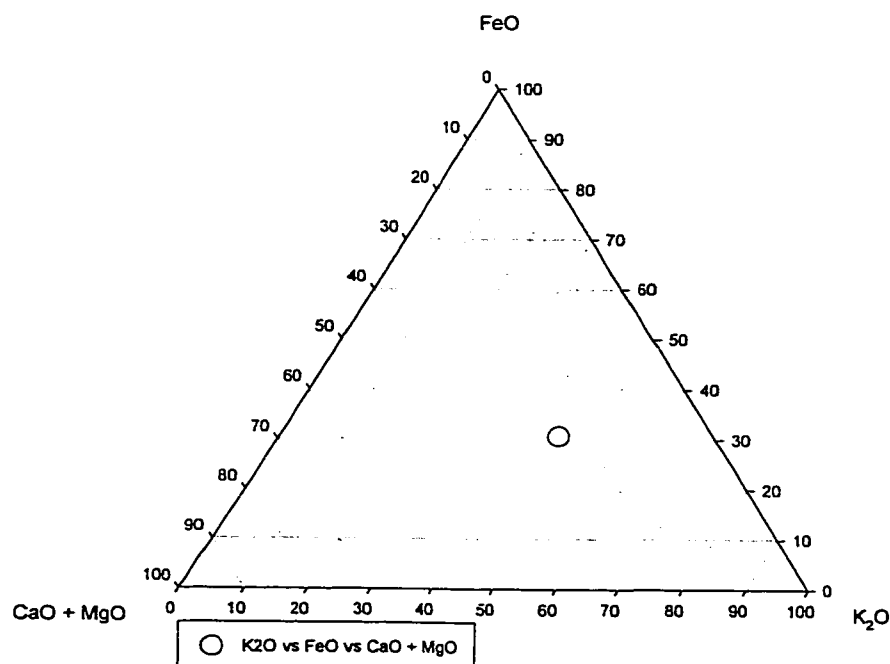


Figure 7.12 – Graphical correlation graph for Myrtöön 40/2

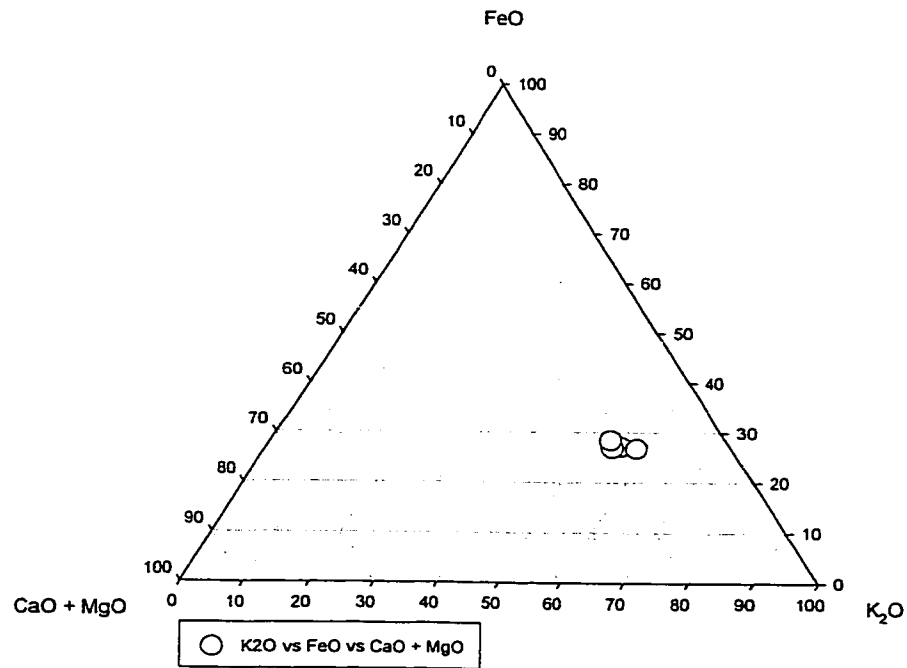


Figure 7.13 – Graphical correlation graph for Myrtöön 40/7

Patte et al [17] reported the existence of a layer from the Campanian area with similar characteristics as those of tephra 40/7. They identified this layer as part of the Neapolitan Yellow Tuff that is thought to have been deposited 12-12.3 thousand years ago. It is possible that layer 40/7 has the same origin.

7.7 Summary

The tephra from the Myrtöön basin were composed of glass shards, pumice shards, and mineral fragments. The tephra layers had different thickness, depending on the location from where they were obtained. The approximate ages of the deposits were only obtained for the tephra in one of the cores.

The glass shards found in these tephra were cusped. The pumice shards contained small, elongated vesicles. The morphology of the glass and pumice shards indicates that the eruptions that gave rise to these volcanic deposits were plinian, and that the magmas involved in the eruptions were high-viscosity magmas.

The mineral fragments that were detected by the XRD and search/match methods included quartz, augite, sodic plagioclase, calcic plagioclase, sanidine, orthoclase, muscovite, microcline, and clinoclase. Other minerals that were expected to be in the samples were not detected, possibly because they were present at concentrations below the detection limit of the method.

The tephra deposits from the Myrtöön basin that were characterized for this work can be grouped as originating from three distinct sources:

- a) the Minoan eruption of the Thera volcano from 3,500 years ago (layers 39/2, and 40/2),
- b) the eruption from the Akrotiri vent of Thera from 18,000 years ago (layers 18/12 and 18/13),
- c) and the eruptions of the volcanoes from Ischia Island in the Campanian area of Italy (layers 20/1, 20/2, 20/3, 37/1, 37/5, and 40/7), occurring during several periods of activity.

CHAPTER 8

CONCLUSIONS

The tephra from the Philippi peat basin that were studied as part of this work belonged to one of three tephra layers that have been designated as the upper tuff (UT), the middle tuff (MT), and the lower tuff (LT). These layers had approximate ages of 10 thousand years, 18 thousand years, and 28-30 thousand years, respectively. The three layers contained glassy particles whose morphology indicated that they originated from high viscosity magmas, and that they were deposited during periods of plinian volcanic eruptions. The layers were identified as follows:

- a) The upper tuff was correlated to the Santorini turbidite ash layer, which is believed to originate from the eruption of the Akrotiri vent of Thera on the island of Santorini approximately 10,000 years before present.
- b) The middle tuff was correlated to the Akrotiri ignimbrite, which is believed to originate from the eruption of the Akrotiri vent of Thera on the island of Santorini approximately 18000 years before present.
- c) The lower tuff was correlated to the Campanian ash layer, which is believed to have originated from volcanoes in the Campanian and Neapolitan regions of Italy approximately 28-30 thousand years ago.

The tephra from the Myrtöön basin that were studied as part of this work had approximate ages of between 1 thousand and 12.5 thousand years. The glassy particles that made up the tephra had morphology that suggested that they originated from plinian

volcanic eruptions. The identification of the tephtras showed that they could be grouped as originating from three possible sources:

- a) Two deposits were correlated to the Minoan eruption of the Thera volcano from 3500 years ago,
- b) Two tephtras were correlated to the eruption from the Akrotiri vent of Thera from 18000 years ago,
- c) and six tephtras were correlated to the eruptions of the volcanoes from Ischia Island in the Campanian area of Italy (layers 20/1, 20/2, 20/3, 37/1, 37/5, and 40/7), occurring during several periods of activity.

The mineralogy of all the tephtras was studied using X-ray powder diffraction and a search/match procedure. However, the method had a limit of detection of approximately 10% w/w for minerals such as augite and biotite, which are important in the differentiation of tephtras from Italian and Hellenic volcanoes. These minerals, as well as other important minerals, were generally not detected by the X-ray diffraction methods of analysis used for this work, and it is believed that it was due to a combination of the high limit of detection of the method and a low mineral content of the tephtras.

REFERENCES

1. Barberi, F., Innocenti, F., Lirer, L., Munno, R., Pescatore, T., Santacroce, R., "The Campanian Ignimbrite: a major prehistoric eruption in the Neapolitan area (Italy)", *Bulletin of Volcanology*, **41-1**, 10-31, (1978).
2. Bates, L. R., and Jackson, J. A., eds., "Glossary of geology, 2nd edition", American Geological Institute, Virginia, U.S.A. (1980).
3. Bish, S. L., Post, J.E. ed, "Modern Powder Diffraction", Mineralogical Society of America, **20**, (1989).
4. Borchardt, G., Harward, M. E., and Schmitt R. A. Correlation of volcanic ash deposits by activation analysis of glass separates. *Quaternary Research*, **1**, 247-260, (1971).
5. Christanis, K., "Phiippi/Greece: A peat deposit awaiting development", *International Peat Journal*, **2**, 45-54, (1987).
6. Civetta, L. Orsi, G., Pappalardo, L., Fisher, R.V., Heiken, G. and Ort, M., "Geochemical zoning, mingling, eruptive dynamics and depositional processes – the Campanian Ignimbrite, Campi Flegrei caldera, Italy". *Journal of Volcanology and Geothermal Research*, **75/3-4**, 183-220, (1997).
7. Cullity, B.D., "Elements of X-ray diffraction", Addison-Wesley Publishing Co. New York, (1967).
8. De Rita D, "Il vulcanismo". In: *Societa Geologica Italiana* (ed.), *Guide Geologiche Regionali*: pp. 50-64, (1993).
9. Denes, G., Madamba, C., private communication.
10. Federman, A., Carey, S., "Electron microprobe correlation of Tephra Layers from Eastern Mediterranean abyssal sediments and the Island of Santorini", *Quaternary Research*, **13**, 160-171, (1980).
11. Fisher, R.V., Schmincke. "Pyroclastic Rocks". Springer-Verlag, Berlin, pp. 1-218, (1984).
12. Geraga St. Tsaila-Monopolis, M., Ioakim, C., Papatheodorou, G., and Ferentinos, G., "An evaluation of palaeo environmental changes during the last 1800 years in the Myrtoon basin, SW Aegean Sea", *Palaeogeography*, **156**, 1-17, (2000).
13. Goodhedw, P. J., Humphreys, F. J., "Electron Microscopy and Analysis", 2nd ed., Taylor and Frances, London, (1988).

14. Keller, J., Ryan, W., Ninkovich, D., Altherr, R., "Explosive volcanic activity in the Mediterranean over the past 2000,000 yr as recorded in deep-sea sediments.", Geological Society of America Bulletin, **89**, 591-604, (1978).
15. Keller, J., "Quaternary tephrochronology in the Mediterranean region". In *Tephra Studies*, (S. Self and R. S. J. Sparks, eds.). pp. 95-102. D. Reidel Publishing Company, (1981).
16. Marinatos, S., *Antiquity*, **13**, 425-439 (1939).
17. Melidonis, N., The peat-lignite deposit of Philippi (Macedonia, Greece), *Geol. Geophys. Res.* **XII/3**, 87-250 (1976).
18. Patterne, M., Guichardt, F., Labeyrie, J., Gillot, P. Y., Duplessy, J.C., "Tyrrhenian sea tephrochronology of the oxygen isotope record for the past 60,000 years", *Marine Geology*, **72**, 259-285, (1986).
19. Patterne, M., Guichardt, F., Labeyrie, J., "Explosive activity of the South Italian Volcanoes during the past 80,000 years as determined by marine tephrochronology", *Journal of Volcanology and Geothermal Research*, **34**, 153-172, (1988).
20. PDF-2 JCPDS database, International Center for Diffraction Data, (1989).
21. Reed, S. J. B., "Electron Microprobe analysis and scanning electron microscopy in geology", Cambridge University Press, (1996).
22. Reed, S. J. B., "Electron Microprobe Analysis", Cambridge University Press, Cambridge, (1993).
23. Richardson, D., Ninkovich, D., "Use of K₂O, Rb, Zr, and Y versus SiO₂ in volcanic ash layers of the eastern Mediterranean to trace their source", *Geological Society of America Bulletin*, **87**, 110-116, (1976).
24. St. Seymour, K., Christanis, K. "Correlation of tephra layer in Western Greece with a late Pleistocene eruption in the Campanian Province of Italy", *Quaternary Research*, **43**, 46-54, (1995).
25. St.-Seymour, K., Christanis, K., Papazisimou, S., Bouzinos, A., Papathodorou, G., Moran, E., and Denes, G., "Tephrostratigraphy and Tephrochronology in the Philippi Peat Basin, Northern Hellas", submitted to *Journal of Volcanology and Geothermal Research* (2000).
26. Thunell, R., Federman, A., Sparks, S., Williams, D., "The age, origin, and volcanological significance of the Y-5 ash layer in the Mediterranean", *Quaternary Research*, **12**, 241-253, (1979).

27. uPDSM User's Manual, r4.21, Feinn-Marquardt & Associates, New York, (1989).
28. Walker, P. L. G., "Volcanological applications of pyroclastic studies" in Tephra Studies, Self & Sparks, ed., Reidel, Dordercht, (1981).
29. Watkins, N.D., Sparks, R., Sigurdsson, H., Huang, T.C., Federman, A., Carey, S., Ninkovich, D., "Volume and extent of the Minoan tephra from Santorini Volcano: new evidence from deep-sea sediment cores", Nature, **271**, 122-126, (1978).

APPENDIX I

Representative X-ray Diffraction Patterns and their Corresponding Peaks Lists

Figure A1 – X-ray diffraction pattern of Philippi sample PH-1 358-362 (EEM-1)

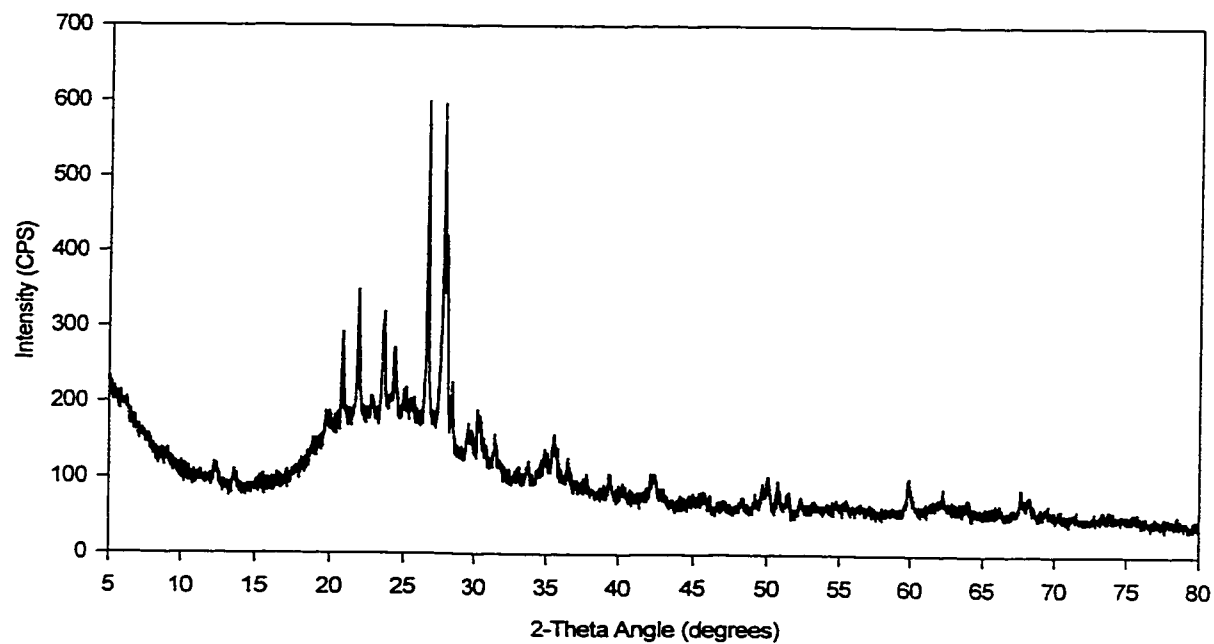


Figure A2 – X-ray diffraction pattern of Philippi sample PH-1 447-450 (EEM-2)

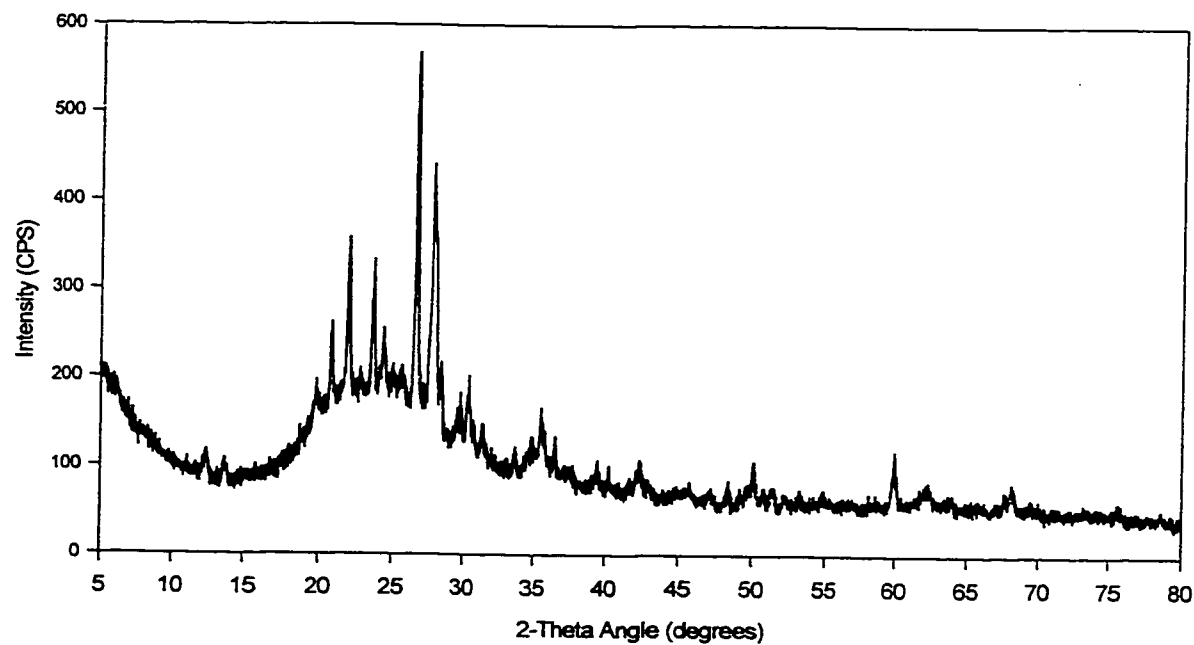


Table A1- Peak list for Philippi sample PH-1 358-362 (EEM-1)

2-theta angle (degrees)	d- spacing	relative intensity	2-theta angle (degrees)	d- spacing	relative intensity	2-theta angle (degrees)	d- spacing	relative intensity
9.04	9.775	5	30.80	2.901	5	53.24	1.719	2
12.34	7.167	5	31.40	2.847	9	54.76	1.675	3
13.66	6.477	2	31.66	2.824	4	55.33	1.659	2
15.12	5.855	3	32.44	2.758	1	57.09	1.612	2
18.82	4.711	5	33.72	2.656	6	59.90	1.543	13
19.18	4.624	4	34.88	2.570	10	60.20	1.536	4
19.72	4.498	10	35.07	2.557	6	61.94	1.497	4
19.96	4.445	7	35.54	2.524	13	62.26	1.490	7
20.50	4.329	4	35.74	2.510	8	62.63	1.482	1
20.78	4.271	28	36.06	2.489	2	62.92	1.476	2
20.98	4.231	5	36.48	2.461	8	63.98	1.454	3
21.90	4.055	38	37.69	2.385	4	64.83	1.437	2
22.74	3.907	6	38.96	2.310	2	65.14	1.431	2
23.60	3.767	27	39.38	2.286	5	65.55	1.423	3
24.00	3.705	6	40.25	2.239	4	66.18	1.411	4
24.14	3.684	6	40.28	2.237	3	67.64	1.384	11
24.34	3.654	20	42.11	2.144	9	68.09	1.376	7
25.00	3.559	7	42.38	2.131	8	68.20	1.374	7
25.54	3.485	5	42.80	2.111	4	68.60	1.367	3
26.58	3.351	100	45.69	1.984	5	69.00	1.360	2
26.90	3.312	5	47.10	1.928	2	69.47	1.352	4
27.04	3.295	4	48.35	1.881	4	69.70	1.348	2
27.72	3.216	99	49.16	1.852	3	71.15	1.324	3
27.94	3.191	58	49.67	1.834	4	73.33	1.290	2
28.36	3.144	15	50.05	1.821	10	75.59	1.257	3
29.54	3.022	9	50.73	1.798	10	77.62	1.229	2
29.76	3.000	6	51.38	1.777	6			
30.20	2.957	17	52.26	1.749	4			
30.38	2.940	15	52.65	1.737	2			
30.65	2.915	7	53.11	1.723	3			

Table A2- Peak list for Philippi sample PH-1 447-450 (EEM-2)

2-theta angle (degrees)	d- spacing	relative intensity	2-theta angle (degrees)	d- spacing	relative intensity	2-theta angle (degrees)	d- spacing	relative intensity
6.92	12.764	6	29.80	2.996	12	49.79	1.830	5
8.28	10.670	5	30.26	2.951	14	50.08	1.820	13
9.78	9.037	3	30.38	2.940	20	50.73	1.798	5
10.18	8.682	1	30.70	2.910	7	51.35	1.778	5
11.06	7.993	3	31.42	2.845	8	52.13	1.753	4
12.20	7.249	4	31.72	2.819	3	53.21	1.720	5
12.40	7.132	7	32.05	2.790	3	54.87	1.672	4
13.68	6.468	7	32.24	2.774	3	58.16	1.585	4
13.84	6.393	4	33.61	2.664	5	59.94	1.542	14
15.74	5.626	6	34.52	2.596	5	61.75	1.501	3
18.68	4.746	5	34.67	2.585	5	62.07	1.494	4
19.18	4.624	4	34.85	2.572	7	62.31	1.489	6
19.80	4.480	12	35.07	2.557	6	63.74	1.459	3
20.36	4.358	5	35.52	2.525	16	63.98	1.454	4
20.48	4.333	6	35.77	2.508	10	67.64	1.384	6
20.80	4.267	22	36.04	2.490	4	68.09	1.376	5
21.92	4.052	41	36.22	2.478	5	68.25	1.373	5
22.76	3.904	6	36.48	2.461	9	69.41	1.353	4
23.60	3.767	30	37.70	2.384	4	70.91	1.328	2
23.88	3.723	4	39.12	2.301	3	75.59	1.257	4
24.06	3.696	6	39.42	2.284	9	78.54	1.217	4
24.34	3.654	16	40.10	2.247	4			
24.94	3.567	6	40.26	2.238	6			
25.22	3.528	4	41.72	2.163	3			
25.54	3.485	5	42.15	2.142	6			
25.62	3.474	7	42.38	2.131	10			
25.78	3.453	4	42.61	2.120	4			
26.58	3.351	100	42.95	2.104	3			
26.98	3.302	5	44.69	2.026	3			
27.10	3.288	5	45.72	1.983	4			
27.44	3.248	19	45.96	1.973	1			
27.72	3.216	63	46.74	1.942	3			
27.94	3.191	47	47.07	1.929	2			
28.36	3.144	15	48.35	1.881	6			
29.44	3.032	6	49.18	1.851	5			
29.58	3.018	10	49.53	1.839	5			
				1.830	5			

Figure A3 – X-ray diffraction pattern of Philippi sample PH-1 630-640 (EEM-3)

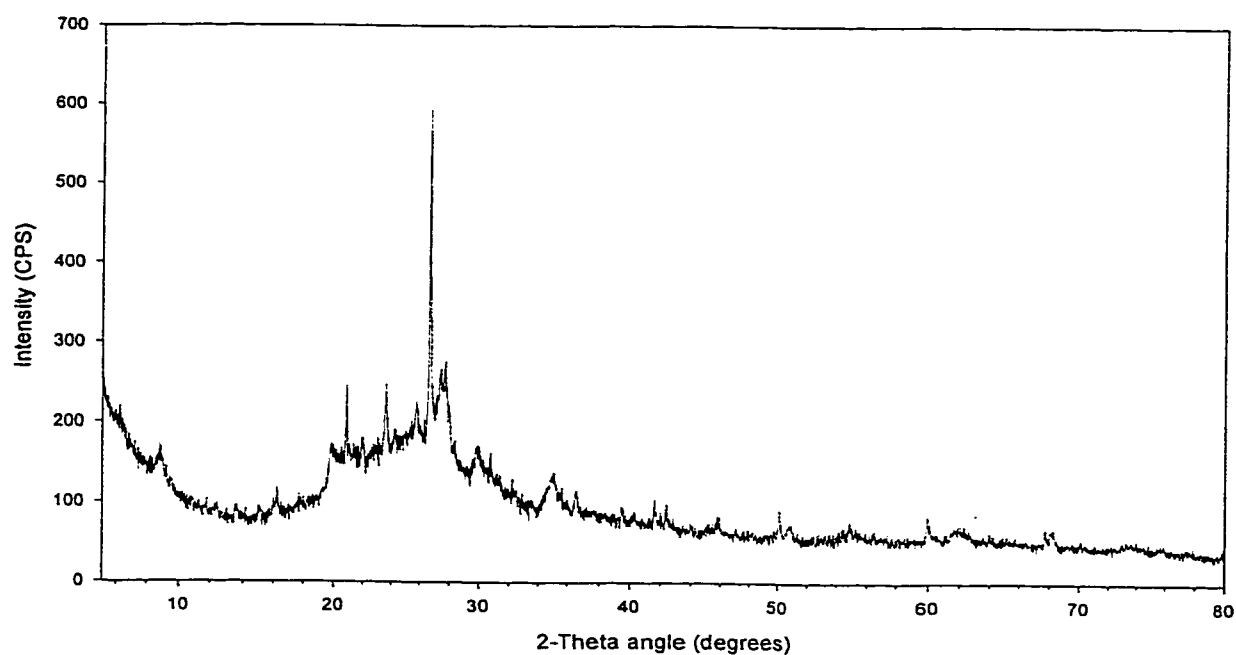


Figure A4 – X-ray diffraction pattern of Philippi sample PH-1 640-660 (EEM-4)

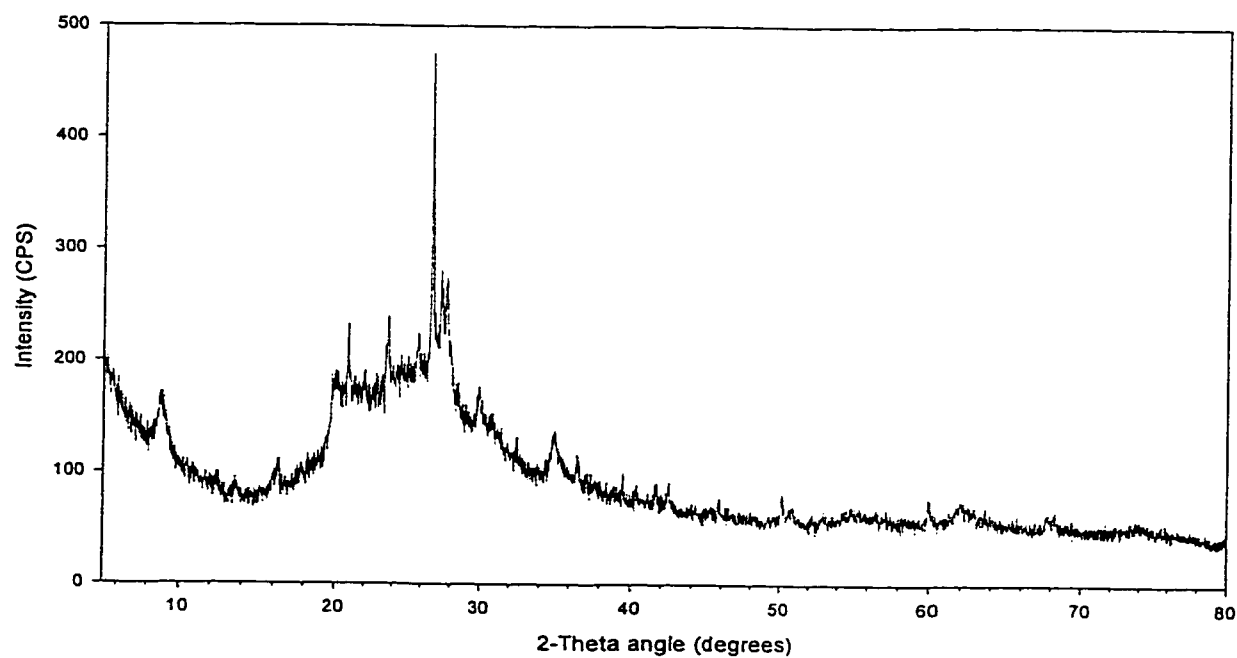


Table A3- Peak list for Philippi sample PH-1 630-640 (EEM-3)

2-theta angle (degrees)	d- spacing	relative intensity	2-theta angle (degrees)	d- spacing	relative intensity	2-theta angle (degrees)	d- spacing	relative intensity
8.84	9.995	11	30.00	2.976	9	55.30	1.66	4
9.14	9.668	4	30.36	2.942	3	59.94	1.542	9
9.46	9.341	4	30.44	2.934	3	61.53	1.506	3
12.46	7.098	3	30.74	2.906	7	61.75	1.501	3
13.60	6.506	3	31.20	2.864	4	61.98	1.496	3
15.18	5.832	2	31.40	2.847	4	62.31	1.489	3
16.00	5.535	6	32.22	2.776	5	62.68	1.481	2
16.26	5.447	8	32.46	2.756	4	64.03	1.453	4
19.82	4.476	11	32.68	2.738	3	65.19	1.43	3
20.30	4.371	6	32.88	2.722	3	67.75	1.382	6
20.50	4.329	5	34.43	2.603	4	68.14	1.375	7
20.68	4.292	6	34.60	2.59	6	70.18	1.34	2
20.84	4.259	23	34.97	2.564	11			
21.02	4.223	7	35.38	2.535	5			
21.36	4.157	6	35.58	2.521	5			
21.48	4.134	5	35.98	2.494	4			
21.70	4.092	4	36.53	2.458	7			
21.96	4.044	5	37.18	2.416	2			
22.86	3.887	5	37.65	2.387	2			
23.14	3.841	4	39.46	2.282	7			
23.56	3.773	15	40.28	2.237	4			
24.22	3.672	4	41.56	2.171	9			
25.30	3.517	4	42.40	2.13	7			
25.72	3.461	9	42.87	2.108	2			
26.62	3.346	100	44.03	2.055	3			
26.94	3.307	11	45.31	2	3			
27.12	3.285	14	45.79	1.98	5			
27.26	3.269	15	45.99	1.972	3			
27.40	3.252	21	47.07	1.929	2			
27.68	3.22	26	49.79	1.83	3			
27.94	3.191	15	50.11	1.819	11			
28.34	3.147	5	50.80	1.796	4			
29.46	3.03	4	51.35	1.778	2			
29.60	3.016	4	54.48	1.683	4			
29.80	2.996	9	54.83	1.673	7			

Table A4- Peak list for Philippi sample PH-1 640-660 (EEM-4)

2-theta angle (degrees)	d- spacing	relative intensity	2-theta angle (degrees)	d- spacing	relative intensity	2-theta angle (degrees)	d- spacing	relative intensity
8.90	9.928	16	27.40	3.252	28	47.18	1.925	2
9.30	9.502	8	27.68	3.22	33	47.60	1.909	3
10.48	8.434	3	27.92	3.193	15	50.11	1.819	11
10.90	8.11	3	28.46	3.134	3	50.64	1.801	4
12.38	7.144	5	29.90	2.986	13	50.89	1.793	6
13.56	6.525	5	30.12	2.965	8	54.83	1.673	4
13.70	6.458	4	30.26	2.951	7	59.94	1.542	11
15.08	5.87	2	30.78	2.903	9	61.62	1.504	4
16.00	5.535	6	31.00	2.882	5	61.80	1.5	4
16.28	5.44	8	31.18	2.866	5	62.03	1.495	6
16.48	5.375	6	31.42	2.845	4	62.40	1.487	5
17.56	5.046	6	32.44	2.758	7	67.69	1.383	5
17.80	4.979	6	33.88	2.644	3	68.25	1.373	4
19.86	4.467	16	34.40	2.605	6			
20.04	4.427	19	34.65	2.587	6			
20.44	4.341	12	34.85	2.572	12			
20.64	4.3	9	34.98	2.563	14			
20.86	4.255	28	35.32	2.539	7			
21.30	4.168	8	35.58	2.521	6			
21.60	4.111	8	36.54	2.457	11			
22.00	4.037	8	37.20	2.415	5			
22.54	3.942	3	37.43	2.401	5			
22.82	3.894	4	37.72	2.383	4			
23.22	3.828	6	38.02	2.365	6			
23.62	3.764	22	38.89	2.314	6			
24.22	3.672	6	39.08	2.303	5			
24.52	3.628	6	39.46	2.282	12			
25.06	3.551	6	40.12	2.246	4			
25.44	3.498	5	40.32	2.235	6			
25.76	3.456	11	41.60	2.169	7			
25.96	3.429	8	41.70	2.164	5			
26.64	3.343	100	42.32	2.134	4			
26.88	3.314	18	42.49	2.126	7			
27.16	3.281	14	45.26	2.002	4			
27.30	3.264	32	45.79	1.98	9			

Figure A5 – X-ray diffraction pattern of Philippi sample PH-1 660-680 (EEM-5)

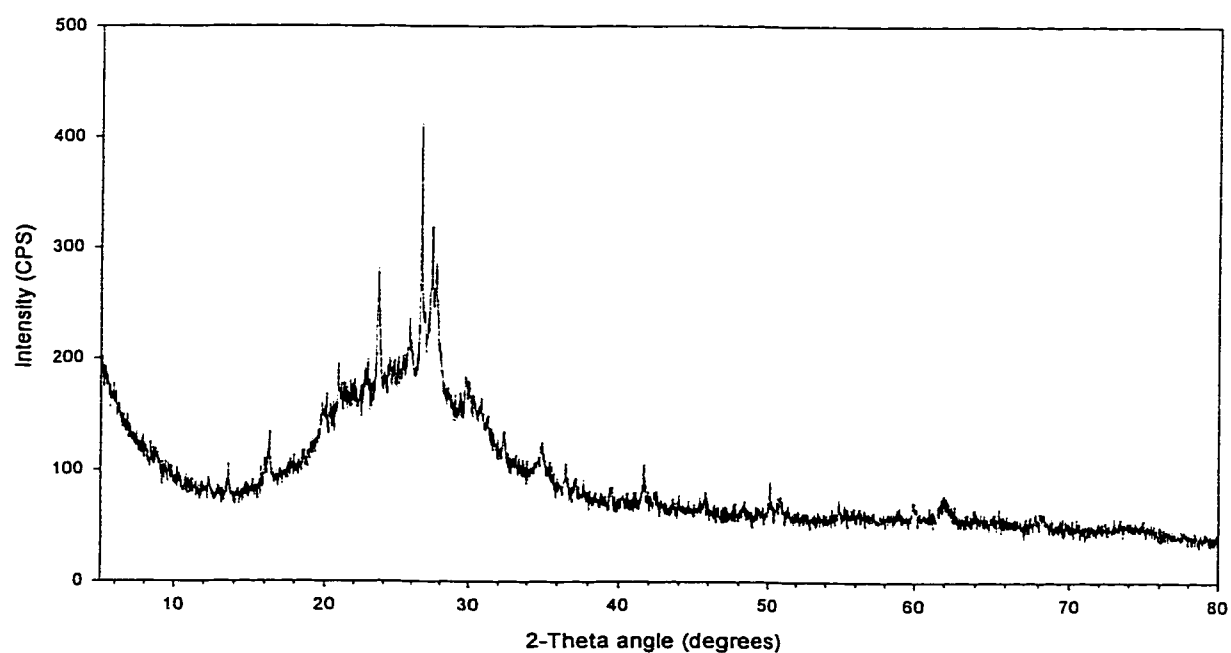


Figure A6 – X-ray diffraction pattern of Philippi sample PH-2 487-490 (EEM-6)

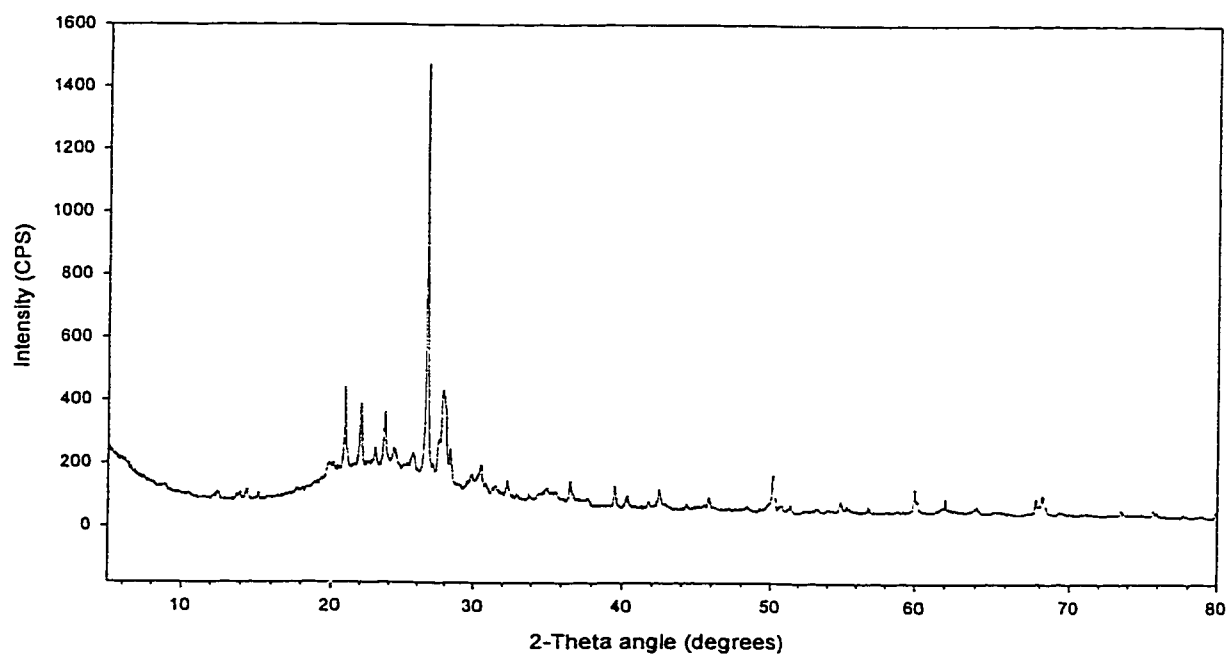


Table A5- Peak list for Philippi sample PH-1 660-680 (EEM-5)

2-theta angle (degrees)	d- spacing	relative intensity	2-theta angle (degrees)	d- spacing	relative intensity	2-theta angle (degrees)	d- spacing	relative intensity
8.82	10.02	6	27.30	3.264	35	48.29	1.883	4
10.18	8.682	5	27.40	3.252	62	50.11	1.819	16
12.30	7.19	5	27.56	3.234	35	50.61	1.802	7
13.56	6.525	10	27.70	3.218	43	50.89	1.793	9
15.20	5.824	4	27.94	3.191	16	51.41	1.776	5
15.94	5.556	11	29.06	3.07	6	54.87	1.672	7
16.24	5.454	19	29.38	3.038	7	59.90	1.543	9
19.70	4.503	11	29.78	2.998	18	61.57	1.505	7
19.80	4.48	15	30.00	2.976	15	61.80	1.5	6
20.06	4.423	11	30.26	2.951	14	62.03	1.495	8
20.32	4.367	10	30.68	2.912	9	67.69	1.383	7
20.62	4.304	9	30.82	2.899	11	68.14	1.375	8
20.82	4.263	25	31.26	2.859	9			
20.94	4.239	14	32.30	2.769	12			
21.08	4.211	15	34.49	2.598	5			
21.24	4.18	12	34.72	2.582	9			
22.66	3.921	10	34.90	2.569	15			
22.82	3.894	13	35.08	2.556	9			
23.02	3.86	8	35.64	2.517	6			
23.14	3.841	8	36.50	2.46	10			
23.60	3.767	45	37.03	2.426	5			
24.04	3.699	8	37.20	2.415	6			
24.24	3.669	10	37.36	2.405	5			
24.36	3.651	10	37.69	2.385	7			
24.56	3.622	6	38.10	2.36	4			
24.64	3.61	8	38.44	2.34	4			
24.94	3.567	10	39.42	2.284	7			
25.30	3.517	7	41.64	2.167	15			
25.76	3.456	18	42.36	2.132	7			
25.90	3.437	13	42.80	2.111	5			
26.60	3.348	100	45.38	1.997	6			
26.78	3.326	22	45.59	1.988	6			
26.92	3.309	22	45.79	1.98	11			
27.06	3.293	17	45.99	1.972	7			
27.18	3.278	21	47.65	1.907	4			

Table A6- Peak list for Philippi sample PH-2 487-490 (EEM-6)

2-theta angle (degrees)	d- spacing	relative intensity	2-theta angle (degrees)	d- spacing	relative intensity	2-theta angle (degrees)	d- spacing	relative intensity
8.90	9.928	1	29.84	2.992	3	45.79	1.98	3
12.42	7.121	1	30.42	2.936	6	48.35	1.881	1
12.50	7.076	1	30.76	2.904	2	49.73	1.832	1
13.88	6.375	1	31.26	2.859	1	49.90	1.826	1
14.32	6.18	2	31.48	2.84	2	50.14	1.818	10
15.10	5.863	1	31.79	2.813	1	50.61	1.802	1
19.84	4.471	3	32.28	2.771	3	50.73	1.798	1
20.10	4.414	3	32.91	2.719	1	51.25	1.781	1
20.86	4.255	19	33.78	2.651	1	51.44	1.775	1
22.00	4.037	13	34.48	2.599	1	52.39	1.745	1
22.96	3.87	4	34.94	2.566	2	54.87	1.672	3
23.64	3.761	12	35.29	2.541	1	55.33	1.659	1
23.84	3.729	1	35.54	2.524	1	56.74	1.621	1
24.26	3.666	4	35.64	2.517	1	56.90	1.617	1
24.44	3.639	2	36.54	2.457	5	59.94	1.542	6
25.20	3.531	1	36.74	2.444	2	60.07	1.539	1
25.62	3.474	3	37.69	2.385	1	62.03	1.495	3
26.64	3.343	100	39.46	2.282	5	64.08	1.452	1
27.06	3.293	2	40.28	2.237	3	67.69	1.383	4
27.54	3.236	7	41.75	2.162	1	67.92	1.379	1
27.80	3.207	20	42.24	2.138	1	68.14	1.375	5
27.96	3.189	17	42.44	2.128	5	68.31	1.372	3
28.32	3.149	7	42.85	2.109	1	73.46	1.288	1
29.56	3.02	1	44.28	2.044	1	75.66	1.256	1

Figure A7 – X-ray diffraction pattern of Philippi sample PH-2 528-530 (EEM-7)

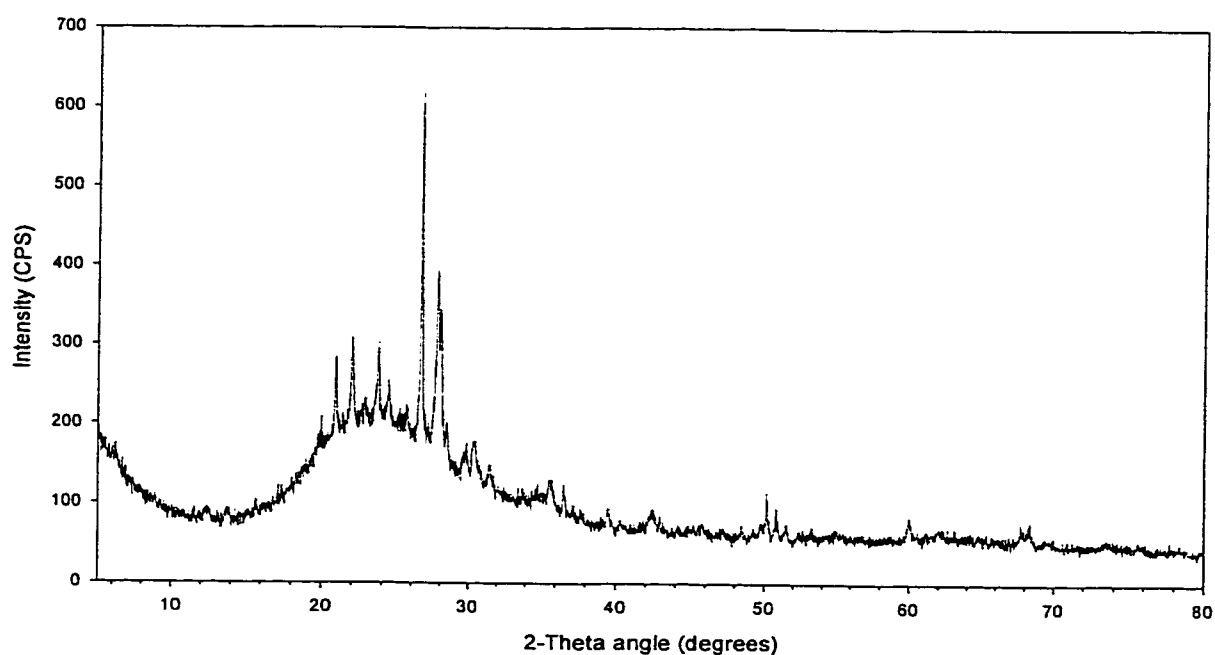


Figure A8 – X-ray diffraction pattern of Philippi sample PH-2 830-840 (EEM-8)

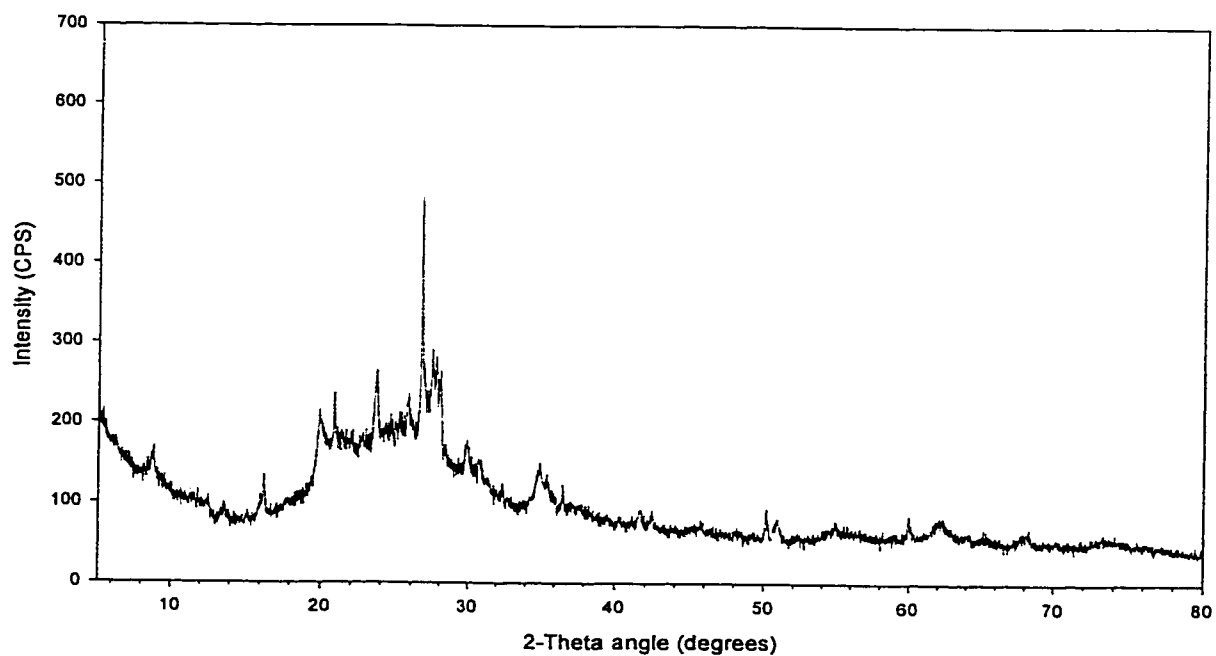


Table A7- Peak list for Philippi sample PH-2 528-530 (EEM-7)

2-theta angle (degrees)	d- spacing	relative intensity	2-theta angle (degrees)	d- spacing	relative intensity	2-theta angle (degrees)	d- spacing	relative intensity
11.58	7.636	3	24.44	3.639	8	37.18	2.416	2
12.38	7.144	3	24.60	3.616	4	37.65	2.387	3
12.54	7.053	3	25.10	3.545	3	39.03	2.306	1
13.76	6.43	3	25.28	3.52	5	39.15	2.299	2
15.20	5.824	2	25.50	3.49	5	39.46	2.282	6
15.66	5.654	2	25.68	3.466	5	40.30	2.236	3
17.18	5.157	2	26.46	3.366	12	40.93	2.203	2
17.42	5.087	3	26.64	3.343	10	41.64	2.167	2
18.04	4.913	4	26.94	3.307	4	41.85	2.157	3
18.30	4.844	4	27.14	3.283	3	42.13	2.143	5
18.52	4.787	4	27.52	3.239	12	42.30	2.135	5
18.88	4.697	4	27.62	3.227	25	42.42	2.129	5
19.74	4.494	8	27.76	3.211	51	42.61	2.12	4
19.86	4.467	7	27.98	3.186	40	42.93	2.105	4
19.98	4.44	7	28.32	3.149	6	45.57	1.989	2
20.06	4.423	6	28.44	3.136	11	45.79	1.98	4
20.40	4.35	5	29.64	3.012	6	47.18	1.925	3
20.86	4.255	22	29.82	2.994	9	47.23	1.923	2
21.36	4.157	6	30.28	2.949	11	48.32	1.882	1
21.44	4.141	4	30.42	2.936	11	48.46	1.877	2
21.56	4.118	5	30.70	2.91	3	49.27	1.848	2
21.70	4.092	7	30.74	2.906	3	49.73	1.832	4
21.98	4.041	25	30.90	2.892	4	49.84	1.828	3
22.54	3.942	5	31.46	2.841	7	49.96	1.824	2
22.64	3.924	5	31.54	2.834	6	50.14	1.818	11
22.82	3.894	6	31.74	2.817	3	50.29	1.813	1
22.94	3.874	6	33.76	2.653	3	50.80	1.796	8
23.02	3.86	3	34.44	2.602	4	50.92	1.792	2
23.46	3.789	6	34.66	2.586	4	51.47	1.774	5
23.56	3.773	11	34.80	2.576	5	52.33	1.747	3
23.68	3.754	22	35.07	2.557	3	53.24	1.719	3
23.88	3.723	7	35.60	2.52	7	55.51	1.654	2
24.12	3.687	5	35.77	2.508	7	59.98	1.541	6
24.22	3.672	7	36.54	2.457	7	62.07	1.494	3
24.36	3.651	9	36.67	2.449	3	62.31	1.489	3

Table A8- Peak list for Philippi sample PH-2 830-840 (EEM-8)

2-theta angle (degrees)	d- spacing	relative intensity	2-theta angle (degrees)	d- spacing	relative intensity	2-theta angle (degrees)	d- spacing	relative intensity
8.76	10.09	5	25.70	3.464	10	36.48	2.461	8
13.56	6.525	3	25.78	3.453	6	39.42	2.284	8
15.18	5.832	5	26.60	3.348	100	40.25	2.239	4
15.96	5.549	6	26.82	3.321	10	41.58	2.17	7
16.22	5.46	7	27.08	3.29	11	42.40	2.13	5
19.88	4.462	11	27.38	3.255	24	50.11	1.819	12
20.82	4.263	26	27.66	3.222	23	50.64	1.801	5
21.26	4.176	7	27.92	3.193	10	50.89	1.793	5
21.44	4.141	4	28.18	3.164	6	54.94	1.67	4
21.86	4.063	6	28.36	3.144	6	59.94	1.542	10
21.98	4.041	22	29.82	2.994	9	67.69	1.383	5
22.72	3.911	3	30.30	2.947	6	68.09	1.376	4
22.84	3.89	4	30.74	2.906	8	68.25	1.373	5
23.56	3.773	18	32.34	2.766	5			
24.34	3.654	4	34.80	2.576	9			
24.46	3.636	6	34.97	2.564	10			
24.72	3.599	2	35.58	2.521	6			
25.70	3.464	10	36.48	2.461	8			

Figure A9 – X-ray diffraction pattern of Philippi sample PH-2 840-855 (EEM-9)

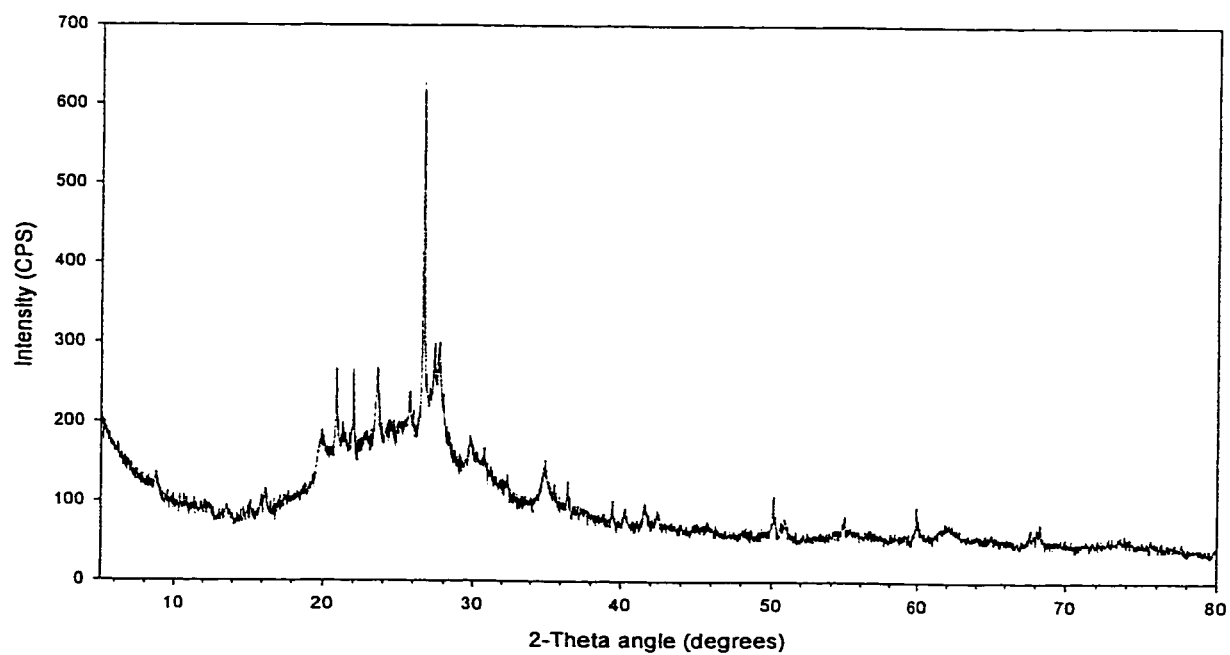


Figure A10 – X-ray diffraction pattern of Philippi sample PH-3 305-309 (EEM-10m2)

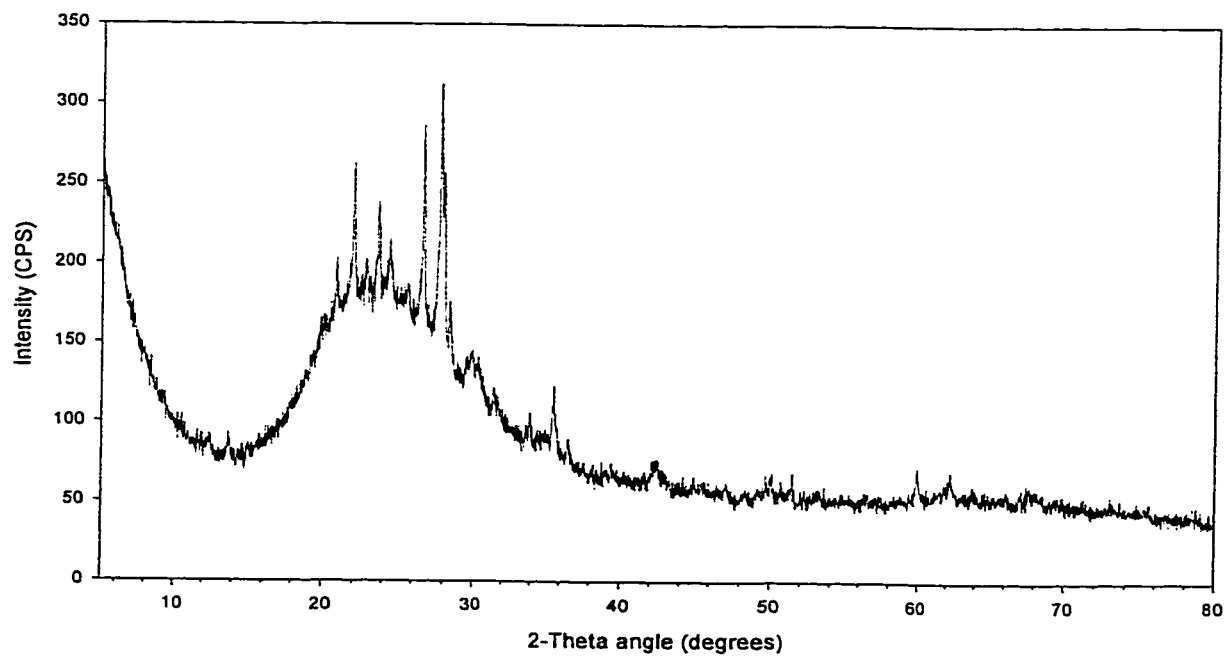


Table A9- Peak list for Philippi sample PH-2 840-855 (EEM-9)

2-theta angle (degrees)	d- spacing	relative intensity	2-theta angle (degrees)	d- spacing	relative intensity	2-theta angle (degrees)	d- spacing	relative intensity
8.76	10.09	5	25.70	3.464	10	36.48	2.461	8
13.56	6.525	3	25.78	3.453	6	39.42	2.284	8
15.18	5.832	5	26.60	3.348	100	40.25	2.239	4
15.96	5.549	6	26.82	3.321	10	41.58	2.17	7
16.22	5.46	7	27.08	3.29	11	42.40	2.13	5
19.88	4.462	11	27.38	3.255	24	50.11	1.819	12
20.82	4.263	26	27.66	3.222	23	50.64	1.801	5
21.26	4.176	7	27.92	3.193	10	50.89	1.793	5
21.44	4.141	4	28.18	3.164	6	54.94	1.67	4
21.86	4.063	6	28.36	3.144	6	59.94	1.542	10
21.98	4.041	22	29.82	2.994	9	67.69	1.383	5
22.72	3.911	3	30.30	2.947	6	68.09	1.376	4
22.84	3.89	4	30.74	2.906	8	68.25	1.373	5
23.56	3.773	18	32.34	2.766	5			
24.34	3.654	4	34.80	2.576	9			
24.46	3.636	6	34.97	2.564	10			
24.72	3.599	2	35.58	2.521	6			
25.70	3.464	10	36.48	2.461	8			

Table A10- Peak list for Philippi sample PH-3 305-309 (EEM-10m2)

2-theta angle (degrees)	d- spacing	relative intensity	2-theta angle (degrees)	d- spacing	relative intensity	2-theta angle (degrees)	d- spacing	relative intensity
12.46	7.098	6	35.22	2.546	5	61.84	1.499	5
12.94	6.834	3	35.55	2.523	25	62.26	1.49	12
13.74	6.44	5	35.77	2.508	9	62.59	1.483	4
15.04	5.886	3	36.10	2.486	4	63.83	1.457	7
19.18	4.624	11	36.50	2.46	10	63.98	1.454	2
20.80	4.267	25	36.76	2.443	5	64.63	1.441	4
21.50	4.13	11	37.14	2.419	2	65.70	1.42	3
21.70	4.092	16	37.64	2.388	4	67.03	1.395	4
21.92	4.052	47	39.08	2.303	2	67.47	1.387	8
22.52	3.945	9	39.40	2.285	7	67.64	1.384	6
22.86	3.887	8	40.42	2.23	2	68.09	1.376	8
23.08	3.85	8	42.15	2.142	10	68.37	1.371	2
23.48	3.786	13	42.38	2.131	10	68.48	1.369	6
23.60	3.767	37	42.55	2.123	9	69.35	1.354	6
23.86	3.726	8	42.87	2.108	4	69.58	1.35	4
24.36	3.651	22	44.21	2.047	4	69.64	1.349	2
25.58	3.48	13	44.95	2.015	6	71.28	1.322	4
26.38	3.376	21	45.52	1.991	5	75.59	1.257	5
26.58	3.351	74	47.05	1.93	6	78.54	1.217	7
26.98	3.302	10	47.15	1.926	4			
27.60	3.229	35	48.27	1.884	3			
27.74	3.213	100	48.38	1.88	4			
27.96	3.189	68	49.21	1.85	5			
28.38	3.142	23	49.73	1.832	8			
29.54	3.022	10	49.99	1.823	10			
29.60	3.016	9	50.11	1.819	6			
29.82	2.994	13	50.73	1.798	6			
29.92	2.984	16	51.47	1.774	10			
30.20	2.957	12	52.29	1.748	5			
30.36	2.942	13	53.18	1.721	4			
30.60	2.919	7	53.35	1.716	3			
31.40	2.847	13	57.09	1.612	4			
31.70	2.82	9	57.32	1.606	4			
33.64	2.662	7	58.76	1.57	3			
33.90	2.642	12	59.94	1.542	12			

Figure A11 – X-ray diffraction pattern of Philippi sample PH-3 565-570 (EEM-11)

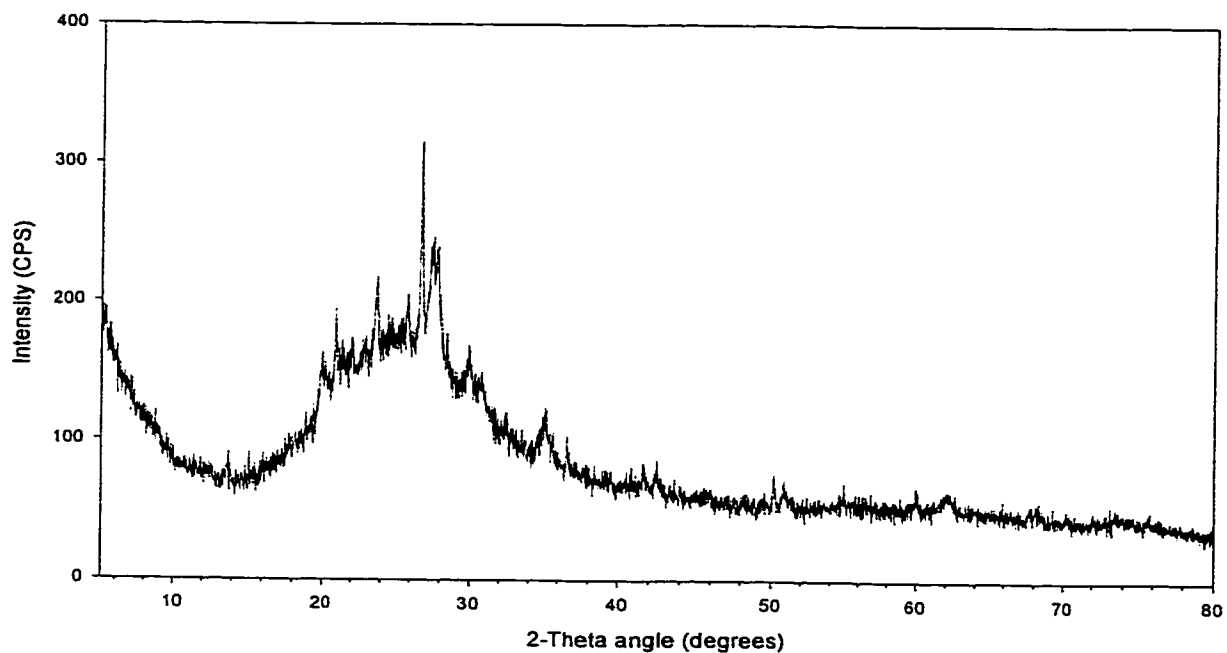


Figure A12 – X-ray diffraction pattern of Philippi sample PH-3 570-595 (EEM-12)

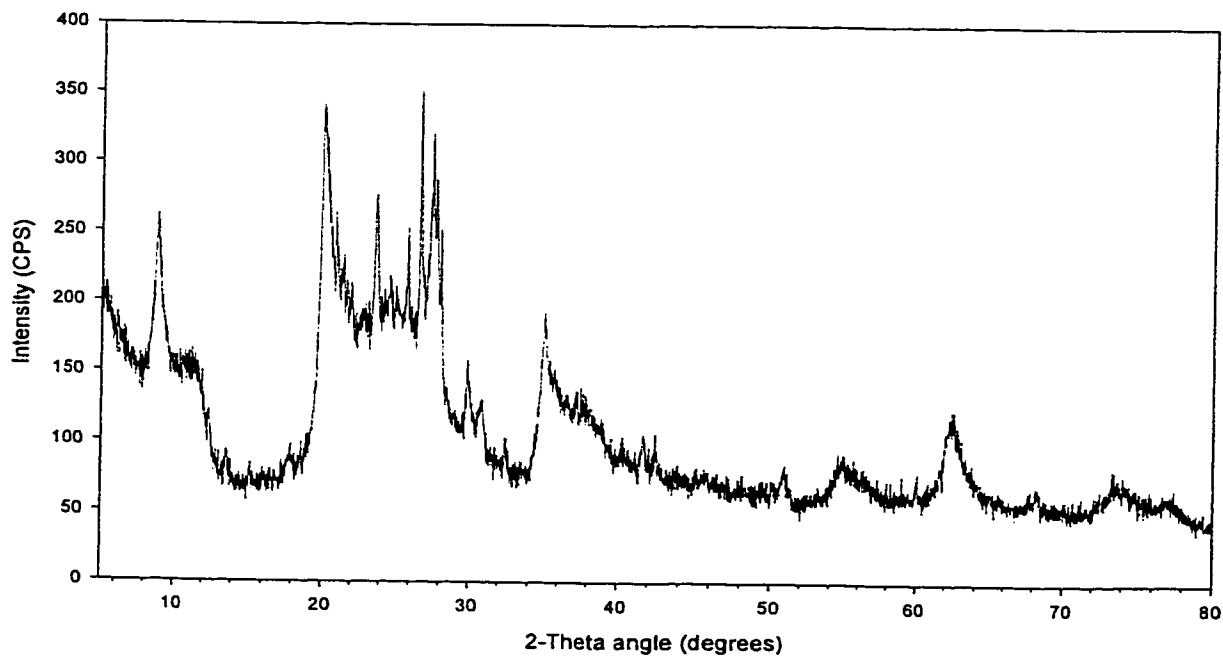


Table A11- Peak list for Philippi sample PH-3 565-570 (EEM-11)

2-theta angle (degrees)	d- spacing	relative intensity	2-theta angle (degrees)	d- spacing	relative intensity	2-theta angle (degrees)	d- spacing	relative intensity
13.68	6.468	10	28.44	3.136	19	42.46	2.127	9
15.08	5.87	10	29.82	2.994	15	50.17	1.817	16
19.96	4.445	22	29.94	2.982	26	50.29	1.813	6
20.18	4.397	20	30.31	2.946	14	50.89	1.793	13
20.46	4.337	12	30.60	2.919	16	51.28	1.78	6
20.90	4.247	32	30.80	2.901	18	54.94	1.67	5
21.14	4.199	14	32.42	2.759	13	56.52	1.627	5
21.38	4.153	15	33.76	2.653	6	59.98	1.541	12
21.98	4.041	17	34.90	2.569	20	61.80	1.5	7
22.80	3.897	4	35.08	2.556	23	62.07	1.494	8
23.66	3.757	30	35.24	2.545	17	62.31	1.489	6
23.98	3.708	12	35.42	2.532	13	67.75	1.382	5
25.78	3.453	20	35.64	2.517	9	68.14	1.375	10
26.66	3.341	100	36.57	2.455	14	68.37	1.371	4
27.34	3.259	46	37.87	2.374	11			
27.44	3.248	50	38.03	2.364	9			
27.74	3.213	48	39.49	2.28	11			
27.96	3.189	25	41.64	2.167	12			

Table A12- Peak list for Philippi sample PH-3 570-595 (EEM-12)

2-theta angle (degrees)	d- spacing	relative intensity	2-theta angle (degrees)	d- spacing	relative intensity	2-theta angle (degrees)	d- spacing	relative intensity
8.84	9.995	56	26.86	3.317	28	54.34	1.687	10
9.48	9.322	14	27.18	3.278	37	54.58	1.68	9
9.86	8.963	5	27.34	3.259	58	54.83	1.673	12
10.22	8.648	6	27.48	3.243	75	55.33	1.659	9
10.46	8.451	9	27.68	3.22	77	59.94	1.542	6
10.68	8.277	12	28.02	3.182	51	60.07	1.539	5
10.98	8.051	17	29.86	2.99	29	62.03	1.495	22
11.96	7.394	18	30.04	2.972	20	62.40	1.487	26
12.42	7.121	16	30.65	2.915	14	62.63	1.482	22
13.62	6.496	11	30.80	2.901	19	67.75	1.382	6
17.68	5.013	6	32.40	2.761	13	68.37	1.371	9
17.84	4.968	9	34.99	2.562	48	73.40	1.289	13
18.04	4.913	6	35.34	2.538	28	73.80	1.283	9
19.98	4.44	100	35.70	2.513	22	74.20	1.277	9
20.88	4.251	48	36.09	2.487	12	74.75	1.269	5
21.26	4.176	26	37.20	2.415	12	76.52	1.244	3
21.40	4.149	22	37.88	2.373	12	76.96	1.238	3
21.60	4.111	15	38.18	2.355	12	77.33	1.233	5
21.98	4.041	10	38.92	2.312	6			
22.86	3.887	6	40.32	2.235	8			
23.50	3.783	31	41.66	2.166	16			
23.62	3.764	49	42.05	2.147	9			
24.58	3.619	17	42.46	2.127	12			
24.98	3.562	12	49.53	1.839	8			
25.66	3.469	12	50.11	1.819	9			
25.78	3.453	32	50.80	1.796	9			
26.66	3.341	98	50.95	1.791	14			

Figure A13 – X-ray diffraction pattern of Philippi sample PH-4 330-335 (EEM-14)

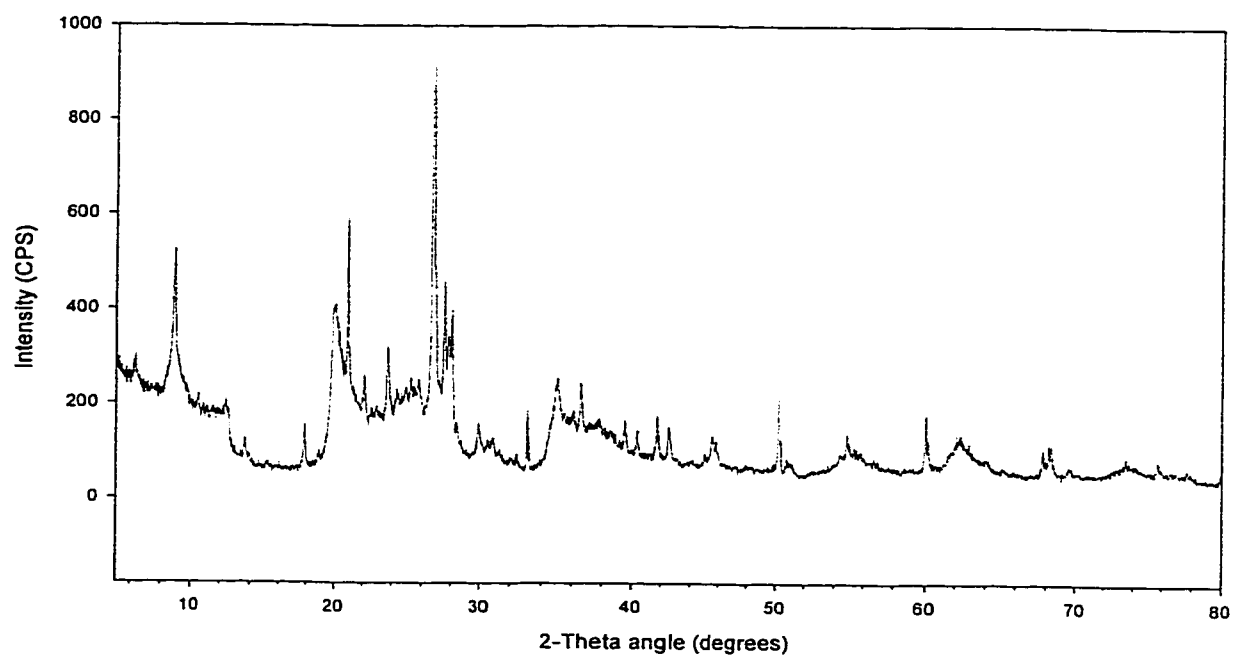


Figure A14 – X-ray diffraction pattern of Philippi sample PH-4 335-350 (EEM-15)

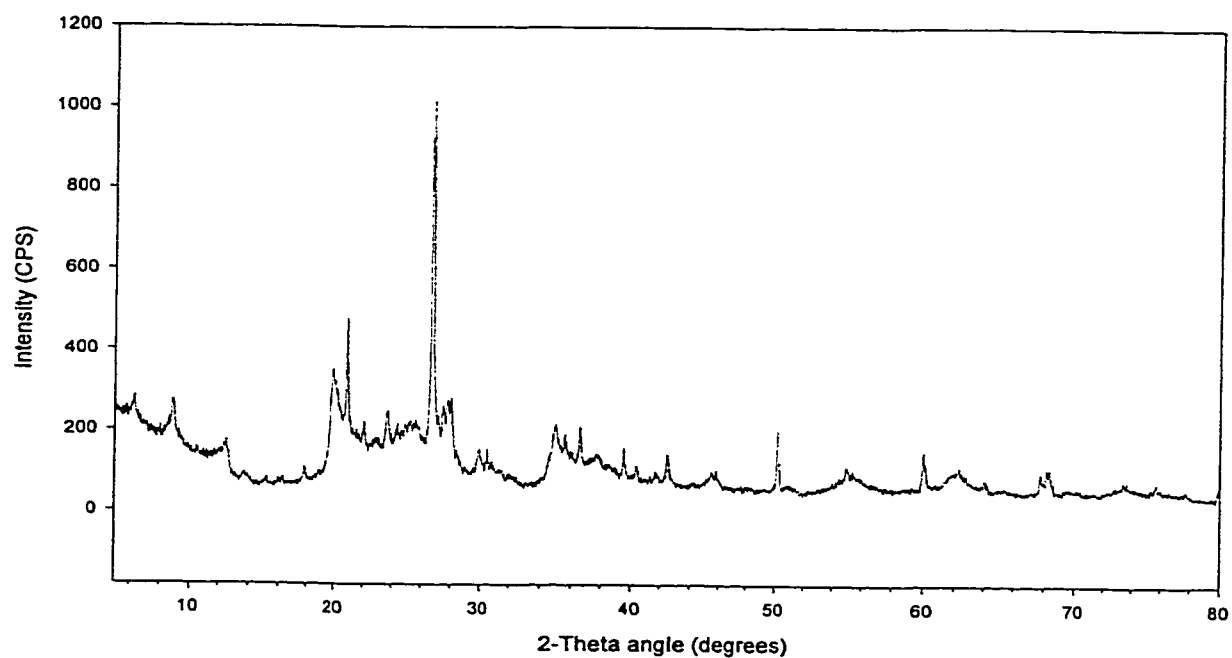


Table A13- Peak list for Philippi sample PH-4 330-335 (EEM-14)

2-theta angle (degrees)	d- spacing	relative intensity	2-theta angle (degrees)	d- spacing	relative intensity	2-theta angle (degrees)	d- spacing	relative intensity
6.34	13.93	3	29.88	2.988	3	55.12	1.665	1
8.92	9.906	18	30.52	2.927	2	55.40	1.657	2
9.46	9.341	2	30.82	2.899	2	55.77	1.647	1
9.70	9.111	2	31.31	2.855	1	59.98	1.541	8
10.56	8.371	2	32.05	2.79	1	60.16	1.537	1
10.90	8.11	1	32.40	2.761	1	61.53	1.506	1
12.38	7.144	4	33.10	2.704	8	61.75	1.501	1
12.80	6.91	1	34.60	2.59	3	62.12	1.493	3
13.66	6.477	2	34.97	2.564	7	62.35	1.488	3
13.94	6.348	1	35.50	2.527	3	62.59	1.483	2
17.06	5.193	1	35.74	2.51	2	62.82	1.478	1
17.84	4.968	5	36.10	2.486	2	64.03	1.453	1
18.88	4.697	1	36.60	2.453	7	67.81	1.381	3
19.94	4.449	15	37.15	2.418	1	67.97	1.378	1
20.00	4.436	15	37.78	2.379	2	68.20	1.374	5
20.32	4.367	11	38.10	2.36	1	68.37	1.371	2
20.66	4.296	7	38.54	2.334	1	69.58	1.35	1
20.90	4.247	26	38.71	2.324	1	73.53	1.287	1
21.26	4.176	3	39.21	2.296	1	73.73	1.284	1
21.46	4.137	2	39.53	2.278	4	75.73	1.255	2
22.08	4.023	4	40.36	2.233	3	75.73	1.255	2
22.60	3.931	1	41.75	2.162	6			
22.92	3.877	1	41.87	2.156	1			
23.66	3.757	8	42.51	2.125	5			
24.32	3.657	2	44.97	2.014	1			
24.94	3.567	2	45.52	1.991	3			
25.24	3.526	3	45.62	1.987	2			
25.74	3.458	2	45.81	1.979	3			
26.70	3.336	100	50.17	1.817	11			
27.14	3.283	4	50.73	1.798	1			
27.50	3.241	19	50.89	1.793	1			
27.78	3.209	11	51.07	1.787	1			
27.86	3.2	10	54.37	1.686	2			
28.04	3.18	15	54.58	1.68	1			
28.40	3.14	1	54.94	1.67	4			

Table A14- Peak list for Philippi sample PH-4 335-350 (EEM-15)

2-theta angle (degrees)	d- spacing	relative intensity	2-theta angle (degrees)	d- spacing	relative intensity	2-theta angle (degrees)	d- spacing	Relative intensity
6.34	13.93	4	28.02	3.182	10	55.77	1.647	1
8.32	10.62	1	28.38	3.142	1	59.98	1.541	8
8.62	10.25	3	29.88	2.988	4	60.72	1.524	1
8.86	9.973	7	30.54	2.925	5	61.35	1.51	1
9.28	9.522	2	30.82	2.899	2	61.57	1.505	2
10.52	8.402	1	31.32	2.854	1	61.75	1.501	2
10.94	8.081	1	32.00	2.795	1	61.98	1.496	2
11.74	7.532	1	34.52	2.596	3	62.31	1.489	3
11.98	7.382	2	34.84	2.573	6	62.54	1.484	1
12.12	7.297	3	34.99	2.562	8	62.87	1.477	1
12.44	7.11	5	35.24	2.545	5	64.08	1.452	2
13.66	6.477	1	35.38	2.535	4	64.23	1.449	1
15.16	5.84	1	35.60	2.52	6	67.81	1.381	4
16.04	5.521	1	35.98	2.494	2	68.20	1.374	5
16.28	5.44	1	36.57	2.455	8	68.37	1.371	3
17.84	4.968	2	37.31	2.408	1	72.87	1.297	1
18.86	4.701	1	37.69	2.385	2	73.53	1.287	2
19.92	4.454	15	37.88	2.373	1	75.37	1.26	1
20.90	4.247	24	38.52	2.335	1	75.73	1.255	2
21.56	4.118	2	38.85	2.316	1	77.70	1.228	1
22.06	4.026	3	39.49	2.28	6			
22.74	3.907	1	40.34	2.234	3			
22.98	3.867	1	41.27	2.186	1			
23.62	3.764	5	41.68	2.165	2			
24.36	3.651	2	42.51	2.125	6			
24.90	3.573	3	44.23	2.046	1			
25.14	3.539	3	45.14	2.007	2			
25.24	3.526	3	45.52	1.991	3			
25.46	3.496	3	45.84	1.978	3			
25.60	3.477	2	50.17	1.817	14			
26.68	3.339	10	53.99	1.697	1			
27.12	3.285	5	54.37	1.686	1			
27.48	3.243	8	54.58	1.68	1			
27.78	3.209	10	54.94	1.67	4			
27.94	3.191	9	55.37	1.658	2			

Figure A15 – X-ray diffraction pattern of Philippi sample PH-4 350-400 (EEM-16)

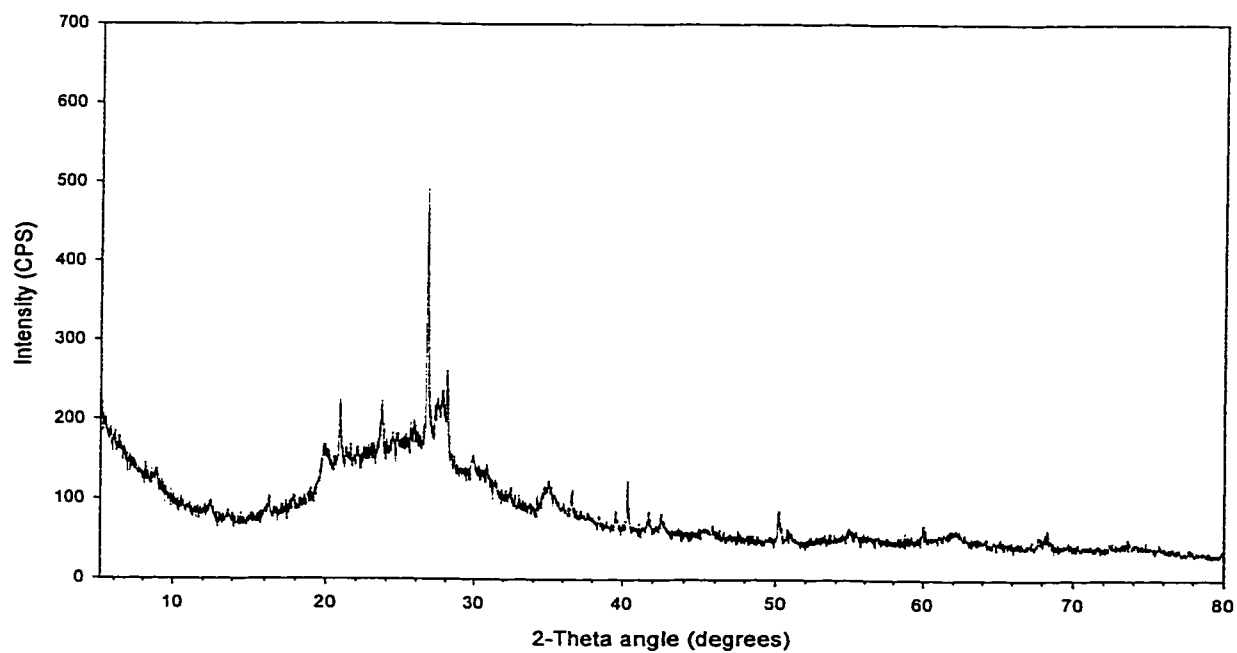


Figure A16 – X-ray diffraction pattern of Philippi sample PH-4 400-430 (EEM-17)

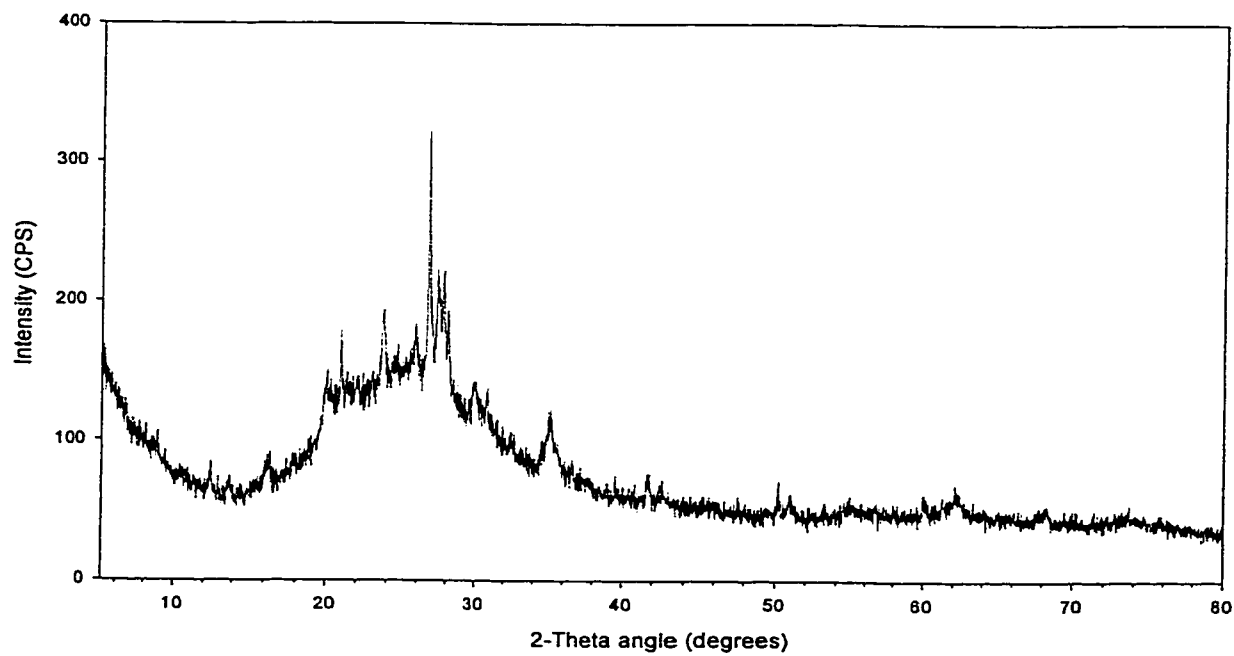


Table A15- Peak list for Philippi sample PH-4 350-400 (EEM-16)

2-theta angle (degrees)	d- spacing	relative intensity	2-theta angle (degrees)	d- spacing	relative intensity	2-theta angle (degrees)	d- spacing	Relative intensity
8.90	9.928	8	28.40	3.14	3	50.20	1.816	15
12.50	7.076	4	28.60	3.119	1	50.43	1.808	2
15.98	5.542	5	29.84	2.992	7	50.73	1.798	4
16.30	5.434	8	30.50	2.929	6	50.95	1.791	4
17.86	4.962	5	30.84	2.897	9	54.97	1.669	4
19.82	4.476	12	32.44	2.758	5	55.37	1.658	3
19.98	4.44	13	34.24	2.617	5	59.94	1.542	6
20.90	4.247	23	34.60	2.59	6	61.84	1.499	4
21.32	4.164	7	34.76	2.579	10	62.07	1.494	2
22.00	4.037	5	35.04	2.559	9	62.21	1.491	4
23.64	3.761	19	35.18	2.549	8	62.45	1.486	3
24.38	3.648	6	35.39	2.534	7	67.81	1.381	5
24.72	3.599	2	36.04	2.49	4	68.20	1.374	7
25.80	3.45	10	36.57	2.455	10	68.37	1.371	4
26.68	3.339	100	38.44	2.34	5	68.54	1.368	2
27.12	3.285	8	39.53	2.278	9			
27.26	3.269	18	40.34	2.234	21			
27.44	3.248	20	41.68	2.165	6			
27.74	3.213	22	42.51	2.125	7			
28.04	3.18	32	45.84	1.978	6			

Table A16- Peak list for Philippi sample PH-4 400-430 (EEM-17)

2-theta angle (degrees)	d- spacing	relative intensity	2-theta angle (degrees)	d- spacing	relative intensity	2-theta angle (degrees)	d- spacing	relative intensity
8.90	9.928	11	25.82	3.448	18	35.42	2.532	10
12.46	7.098	12	26.34	3.381	9	35.60	2.52	9
13.60	6.506	5	26.70	3.336	100	35.80	2.506	7
13.78	6.421	6	26.86	3.317	22	36.00	2.493	5
16.02	5.528	8	27.14	3.283	16	36.57	2.455	9
16.18	5.474	11	27.36	3.257	42	38.99	2.308	7
16.36	5.414	10	27.48	3.243	36	41.75	2.162	5
19.82	4.476	13	27.76	3.211	43	42.34	2.133	6
20.04	4.427	20	28.00	3.184	20	42.51	2.125	8
20.28	4.375	12	28.06	3.177	30	42.65	2.118	9
20.92	4.243	31	28.74	3.104	7	50.23	1.815	17
21.26	4.176	11	29.30	3.046	5	50.83	1.795	7
21.46	4.137	10	29.58	3.018	6	51.01	1.789	7
21.94	4.048	10	29.86	2.99	12	60.03	1.54	10
22.06	4.026	12	30.02	2.974	12	61.30	1.511	7
22.48	3.952	9	30.34	2.944	10	62.12	1.493	10
22.60	3.931	9	30.52	2.927	10	62.40	1.487	9
23.00	3.864	9	30.82	2.899	12	67.97	1.378	5
23.28	3.818	8	30.90	2.892	9	68.25	1.373	6
23.66	3.757	28	32.46	2.756	10	68.42	1.37	4
24.30	3.66	12	34.49	2.598	7			
24.44	3.639	12	34.78	2.577	12			
24.66	3.607	10	34.98	2.563	17			
25.56	3.482	7	35.12	2.553	21			

Figure A17 – X-ray diffraction pattern of Myrtöön sample MYR 18/12 (EEM-50)

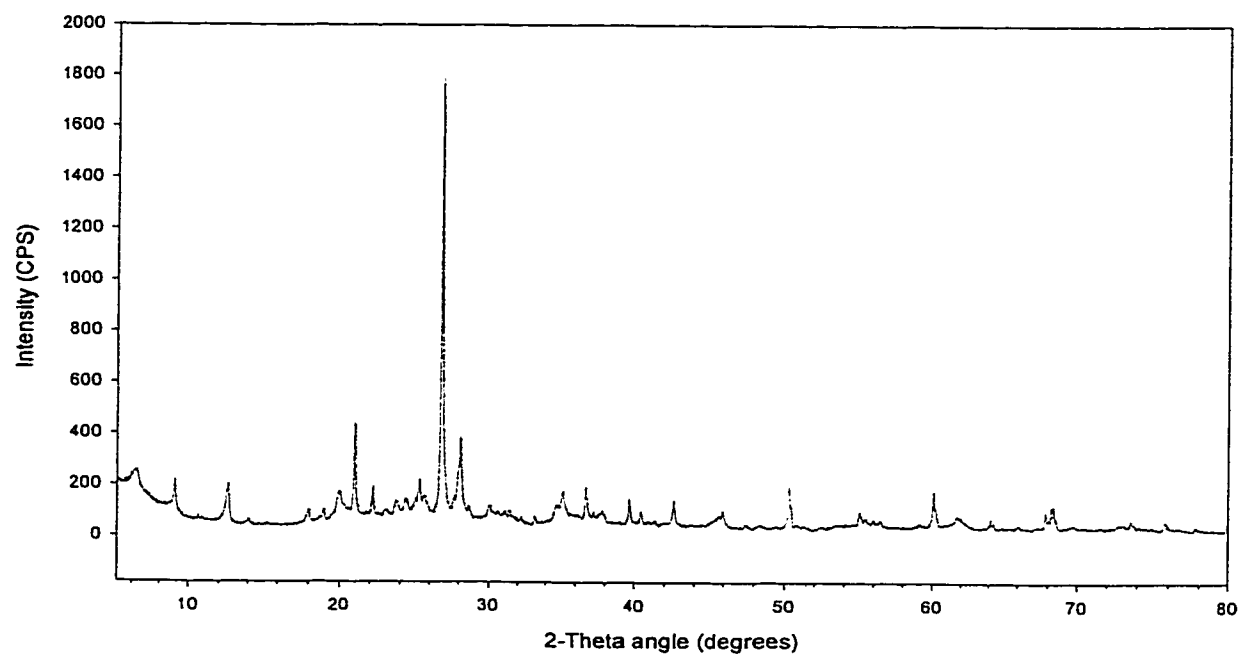


Figure A18 – X-ray diffraction pattern of Myrtöön sample MYR 18/13 (EEM-53)

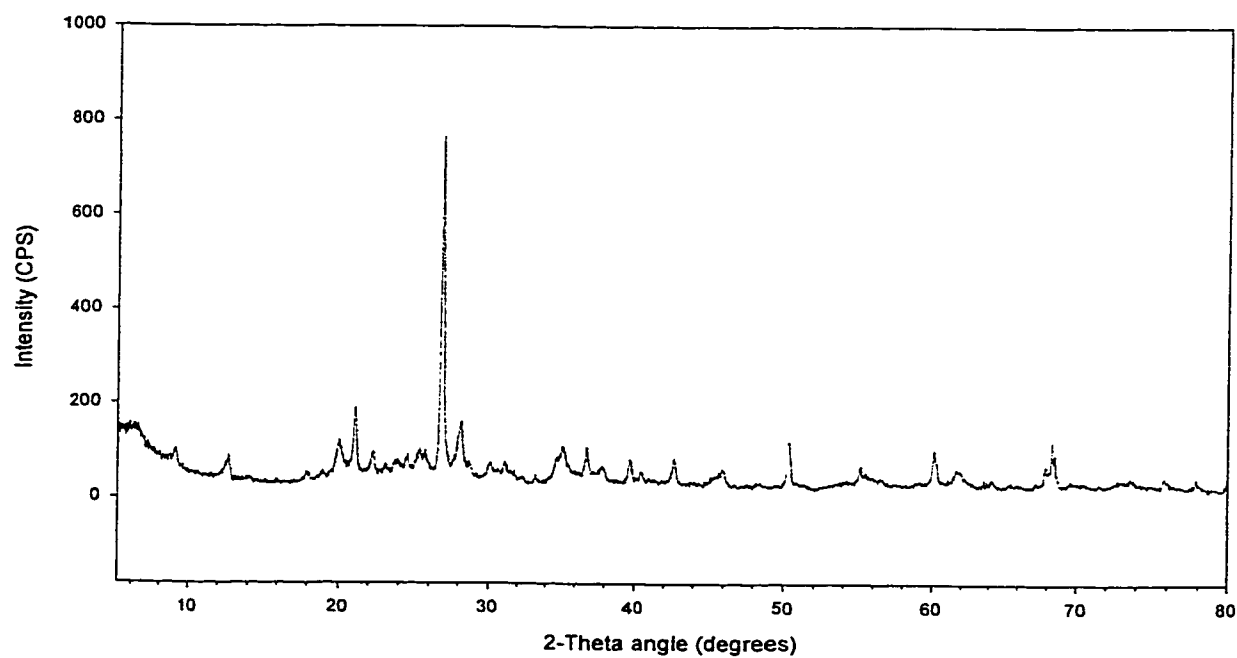


Table A17 – Peak list for Myrtöön sample MYR 18/12 (EEM-50)

2-theta angle (degrees)	d- spacing	relative intensity	2-theta angle (degrees)	d- spacing	relative intensity	2-theta angle (degrees)	d- spacing	relative intensity
6.34	13.93	4	30.60	2.919	1	55.95	1.642	1
9.02	9.796	6	31.10	2.873	1	56.44	1.629	1
12.64	6.998	7	31.40	2.847	2	60.07	1.539	8
14.02	6.312	1	33.17	2.699	1	61.75	1.501	2
17.96	4.935	1	34.66	2.586	2	62.03	1.495	1
18.94	4.682	1	35.09	2.555	4	64.18	1.45	1
19.96	4.445	4	36.68	2.448	7	67.86	1.38	3
21.00	4.227	19	37.22	2.414	1	68.25	1.373	5
22.18	4.005	5	37.64	2.388	1	68.37	1.371	3
23.08	3.85	1	37.78	2.379	2	73.60	1.286	1
23.70	3.751	2	39.62	2.273	5	75.73	1.255	1
24.42	3.642	2	40.42	2.23	2			
25.16	3.537	1	40.87	2.206	1			
25.30	3.517	6	42.57	2.122	5			
25.66	3.469	2	45.16	2.006	1			
26.78	3.326	100	45.43	1.995	1			
26.96	3.305	14	45.69	1.984	2			
27.66	3.222	2	45.91	1.975	3			
28.06	3.177	16	50.29	1.813	9			
28.60	3.119	2	55.01	1.668	3			
30.00	2.976	2	55.48	1.655	1			

Table A18 – Peak list for Myrtöön sample MYR 18/13 (EEM-53)

2-theta angle (degrees)	d- spacing	relative intensity	2-theta angle (degrees)	d- spacing	relative intensity	2-theta angle (degrees)	d- spacing	relative intensity
6.32	13.97	4	28.70	3.108	2	45.43	1.995	2
9.08	9.732	5	30.10	2.967	3	45.67	1.985	2
12.68	6.976	6	30.66	2.914	1	45.91	1.975	5
14.12	6.267	1	31.06	2.877	4	50.29	1.813	14
17.98	4.93	1	31.50	2.838	2	55.04	1.667	4
18.98	4.672	1	31.76	2.815	2	55.37	1.658	2
19.98	4.44	8	32.20	2.778	1	55.95	1.642	1
20.40	4.35	2	32.36	2.764	1	56.52	1.627	1
21.04	4.219	18	33.25	2.692	1	60.11	1.538	10
22.22	3.998	6	34.70	2.583	4	61.66	1.503	4
23.04	3.857	1	35.07	2.557	8	61.89	1.498	2
23.76	3.742	1	35.19	2.548	7	64.23	1.449	1
23.88	3.723	2	35.50	2.527	2	67.92	1.379	6
24.48	3.633	3	36.03	2.491	1	68.31	1.372	16
25.18	3.534	3	36.28	2.474	1	69.70	1.348	1
25.34	3.512	4	36.74	2.444	9	72.80	1.298	1
25.70	3.464	4	37.78	2.379	3	73.60	1.286	2
26.84	3.319	100	39.66	2.271	5	75.80	1.254	3
27.04	3.295	10	40.43	2.229	2	77.85	1.226	3
27.70	3.218	3	42.61	2.12	7			
28.08	3.175	14	45.21	2.004	1			

Figure A19 – X-ray diffraction pattern of Myrtöön sample MYR 20/1 (EEM-56)

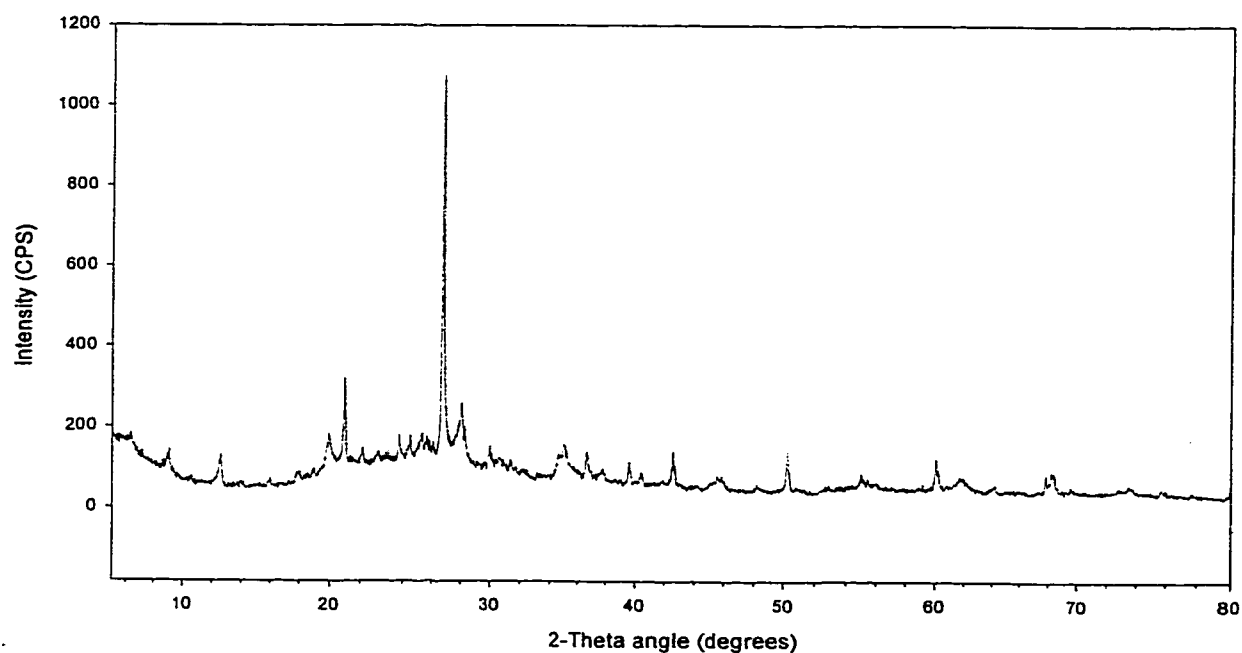


Figure A20 – X-ray diffraction pattern of Myrtöön sample MYR 20/2 (EEM-48)

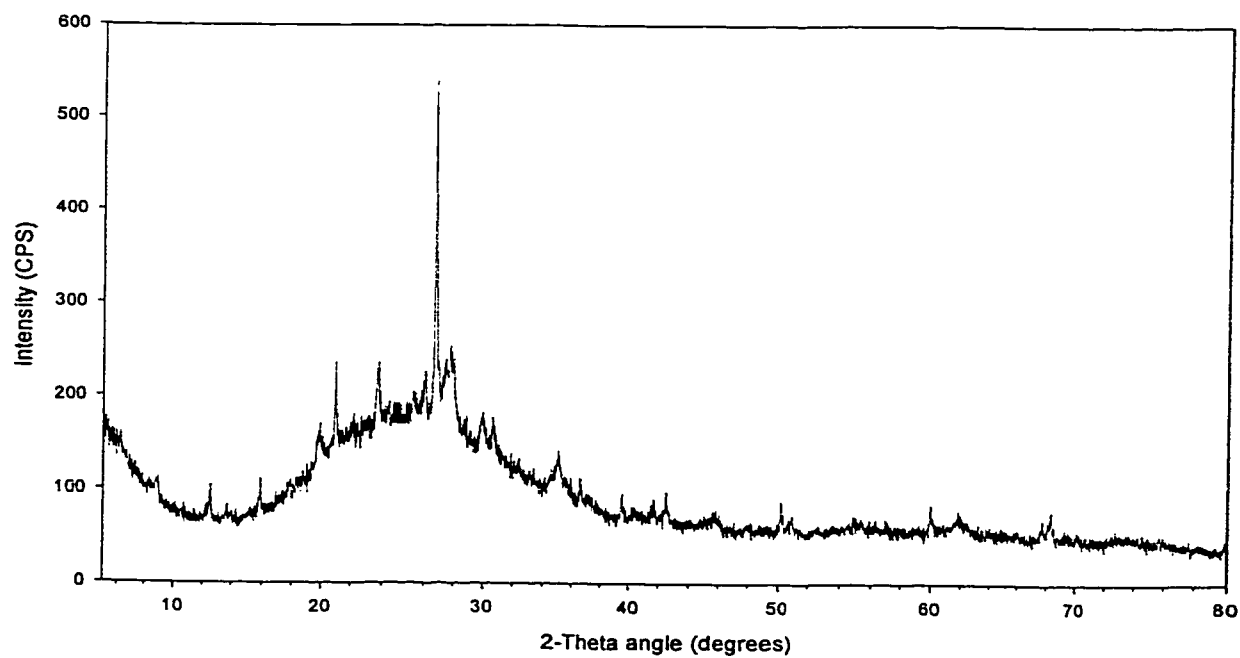


Table A19 – Peak list for Myrtöön sample MYR 20/1 (EEM-56)

2-theta angle (degrees)	d- spacing	relative intensity	2-theta angle (degrees)	d- spacing	relative intensity	2-theta angle (degrees)	d- spacing	relative intensity
6.42	13.76	2	29.98	2.978	4	60.03	1.54	8
9.00	9.818	5	30.60	2.919	2	61.66	1.503	1
12.60	7.02	6	30.76	2.904	1	61.84	1.499	2
15.96	5.549	1	31.32	2.854	2	62.12	1.493	1
17.92	4.946	1	34.62	2.589	3	64.13	1.451	1
19.92	4.454	7	34.80	2.576	3	67.81	1.381	4
20.98	4.231	18	35.04	2.559	7	68.25	1.373	4
22.12	4.015	3	36.67	2.449	6	75.73	1.255	1
23.12	3.844	1	37.74	2.382	1			
23.66	3.757	3	39.56	2.276	6			
24.46	3.636	4	40.38	2.232	2			
25.28	3.52	4	42.57	2.122	8			
25.62	3.474	2	45.00	2.013	1			
26.10	3.411	1	45.33	1.999	1			
26.74	3.331	100	45.84	1.978	3			
26.92	3.309	11	50.23	1.815	10			
28.02	3.182	13	55.01	1.668	2			
28.28	3.153	8	55.44	1.656	1			

Table A20 – Peak list for Myrtöön sample MYR 20/2 (EEM-48)

2-theta angle (degrees)	d- spacing	relative intensity	2-theta angle (degrees)	d- spacing	relative intensity	2-theta angle (degrees)	d- spacing	relative intensity
8.90	9.928	5	26.82	3.321	17	45.62	1.987	3
12.50	7.076	6	27.46	3.245	16	45.81	1.979	3
13.64	6.487	1	27.74	3.213	20	50.17	1.817	9
15.88	5.576	6	29.94	2.982	9	50.98	1.79	3
17.82	4.973	1	30.60	2.919	11	59.98	1.541	7
19.86	4.467	6	34.97	2.564	9	61.84	1.499	2
20.90	4.247	19	36.57	2.455	7	67.75	1.382	4
23.70	3.751	16	39.47	2.281	6	68.20	1.374	3
24.38	3.648	4	41.58	2.17	2	68.37	1.371	5
26.04	3.419	11	41.70	2.164	3			
26.68	3.339	100	42.51	2.125	9			

Figure A21 – X-ray diffraction pattern of Myrtöön sample MYR 20/3 (EEM-60)

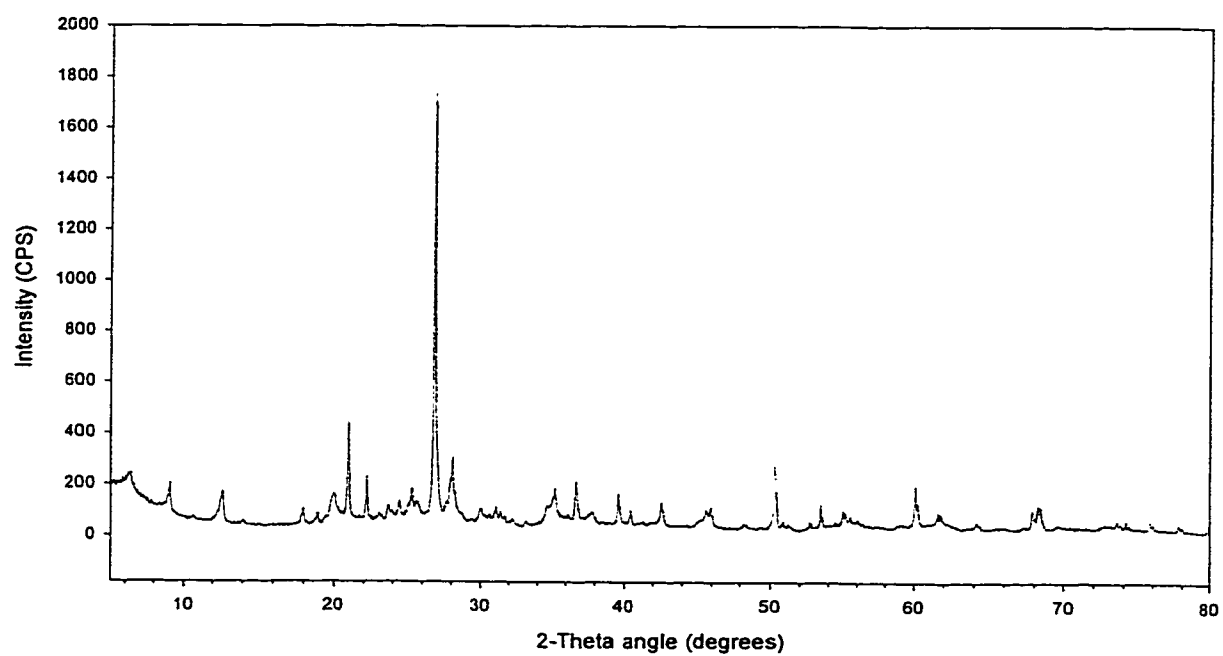


Figure A22 – X-ray diffraction pattern of Myrtöön sample MYR 37/1 (EEM-61)

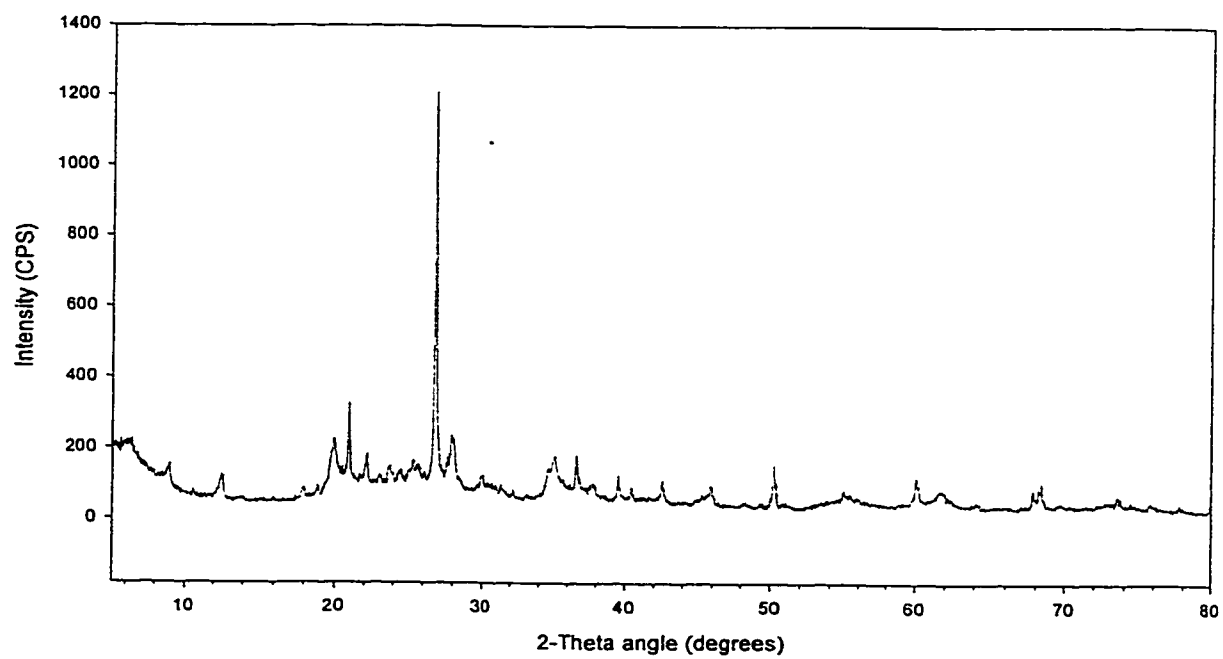


Table A21 – Peak list for Myrtöön sample MYR 20/3 (EEM-60)

2-theta angle (degrees)	d- spacing	relative intensity	2-theta angle (degrees)	d- spacing	relative intensity	2-theta angle (degrees)	d- spacing	relative intensity
6.40	13.8	3	28.04	3.18	12	50.26	1.814	15
9.00	9.818	6	29.98	2.978	2	50.83	1.795	1
10.62	8.324	1	30.60	2.919	1	51.25	1.781	1
12.62	7.009	6	31.08	2.875	2	52.72	1.735	1
14.00	6.321	1	31.38	2.848	2	53.41	1.714	3
17.94	4.94	3	31.68	2.822	1	54.97	1.669	3
18.92	4.687	1	32.28	2.771	1	55.15	1.664	1
19.94	4.449	4	33.22	2.695	1	55.51	1.654	1
20.98	4.231	18	34.65	2.587	2	60.07	1.539	9
22.20	4.001	8	35.18	2.549	5	61.62	1.504	3
23.04	3.857	1	36.68	2.448	9	64.13	1.451	1
23.68	3.754	1	37.56	2.393	1	67.86	1.38	4
23.94	3.714	1	37.75	2.381	2	68.25	1.373	5
24.40	3.645	2	39.60	2.274	6	73.53	1.287	1
25.04	3.553	1	40.42	2.23	3	74.13	1.278	1
25.28	3.52	5	42.57	2.122	5	75.73	1.255	2
25.66	3.469	2	45.21	2.004	1	77.77	1.227	1
26.76	3.329	100	45.59	1.988	3			
26.94	3.307	16	45.91	1.975	4			

Table A22 – Peak list for Myrtöön sample MYR 37/1 (EEM-61)

2-theta angle (degrees)	d- spacing	relative intensity	2-theta angle (degrees)	d- spacing	relative intensity	2-theta angle (degrees)	d- spacing	relative intensity
6.34	13.93	6	26.16	3.404	1	40.36	2.233	4
8.96	9.862	8	26.76	3.329	100	42.55	2.123	8
12.56	7.042	7	26.90	3.312	20	45.26	2.002	2
17.90	4.951	2	27.64	3.225	8	45.55	1.99	2
18.90	4.692	1	27.86	3.2	17	45.89	1.976	7
19.92	4.454	14	28.00	3.184	17	50.23	1.815	18
20.94	4.239	29	30.00	2.976	4	54.97	1.669	4
22.10	4.019	9	31.34	2.852	2	55.37	1.658	2
23.06	3.854	1	32.18	2.779	1	60.03	1.54	10
23.62	3.764	3	33.17	2.699	1	61.66	1.503	4
23.72	3.748	5	34.60	2.59	8	61.94	1.497	3
24.46	3.636	2	35.04	2.559	11	64.13	1.451	1
24.92	3.57	2	36.63	2.451	14	67.81	1.381	8
25.26	3.523	5	37.64	2.388	3	68.20	1.374	7
25.62	3.474	4	37.87	2.374	3	68.42	1.37	5
25.76	3.456	2	39.55	2.277	9	73.53	1.287	4

Figure A23 – X-ray diffraction pattern of Myrtöön sample MYR 39/1 (EEM-63)

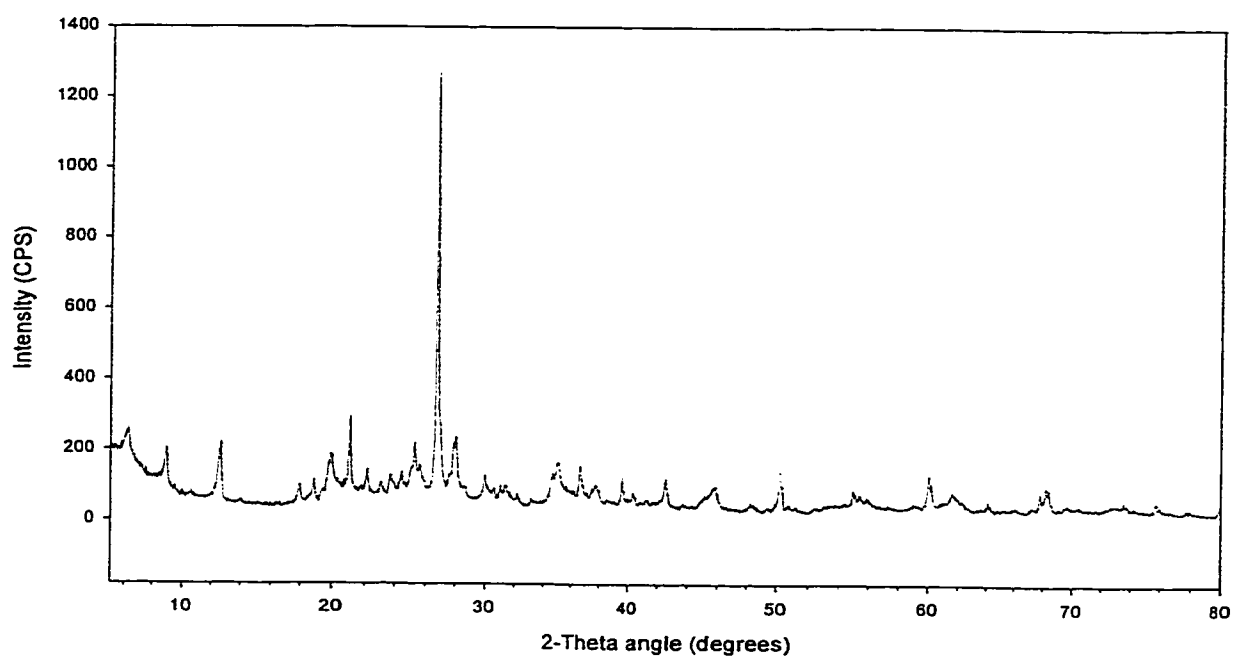


Figure A24 – X-ray diffraction pattern of Myrtöön sample MYR 39/2 (EEM-64)

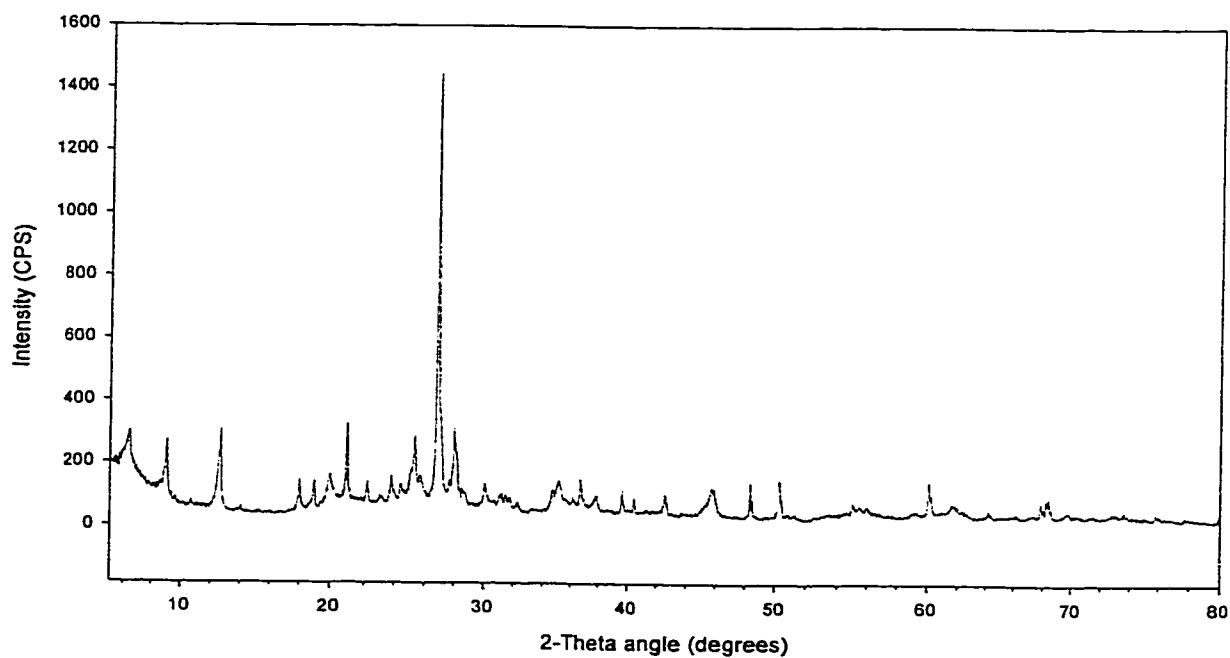


Table A23 – Peak list for Myrtöön sample MYR 39/1 (EEM-63)

2-theta angle (degrees)	d- spacing	relative intensity	2-theta angle (degrees)	d- spacing	relative intensity	2-theta angle (degrees)	d- spacing	relative intensity
6.32	13.97	7	27.66	3.222	3	45.23	2.003	1
8.96	9.862	8	27.98	3.186	12	45.74	1.982	3
10.58	8.355	1	28.64	3.114	1	45.84	1.978	4
12.56	7.042	12	29.96	2.98	4	48.24	1.885	1
17.90	4.951	3	30.56	2.923	2	48.43	1.878	1
18.86	4.701	3	31.02	2.881	2	50.23	1.815	10
19.88	4.462	7	31.34	2.852	2	54.94	1.67	3
20.94	4.239	16	31.66	2.824	1	55.37	1.658	2
21.74	4.085	1	32.16	2.781	2	55.99	1.641	1
22.10	4.019	4	33.12	2.703	1	60.03	1.54	7
22.96	3.87	1	34.67	2.585	4	61.57	1.505	3
23.66	3.757	3	34.99	2.562	6	61.80	1.5	1
24.40	3.645	3	36.62	2.452	7	62.26	1.49	1
25.02	3.556	3	37.52	2.395	1	64.13	1.451	1
25.22	3.528	9	37.70	2.384	3	67.81	1.381	4
25.56	3.482	4	39.55	2.277	5	68.20	1.374	6
26.72	3.334	100	40.36	2.233	2	75.73	1.255	2
26.90	3.312	17	42.53	2.124	6			

Table A24 – Peak list for Myrtöön sample MYR 39/2 (EEM-64)

2-theta angle (degrees)	d- spacing	relative intensity	2-theta angle (degrees)	d- spacing	relative intensity	2-theta angle (degrees)	d- spacing	relative intensity
6.36	13.89	10	26.82	3.321	100	39.64	2.272	5
9.06	9.753	14	26.98	3.302	26	40.45	2.228	3
10.68	8.277	1	27.64	3.225	3	42.59	2.121	5
12.66	6.987	18	27.98	3.186	14	45.16	2.006	1
14.04	6.303	1	28.50	3.129	3	45.74	1.982	5
17.98	4.93	6	28.64	3.114	2	45.91	1.975	5
18.96	4.677	6	30.02	2.974	4	48.32	1.882	8
19.96	4.445	6	31.14	2.87	2	50.29	1.813	10
21.02	4.223	19	31.42	2.845	3	55.01	1.668	2
22.20	4.001	4	31.72	2.819	2	55.44	1.656	1
23.02	3.86	1	32.30	2.769	1	55.95	1.642	1
23.16	3.837	1	34.70	2.583	3	60.11	1.538	10
23.74	3.745	4	35.08	2.556	5	61.66	1.503	2
24.44	3.639	2	35.18	2.549	5	64.18	1.45	1
25.12	3.542	5	36.16	2.482	1	67.86	1.38	4
25.32	3.515	13	36.70	2.447	7	68.25	1.373	4
25.66	3.469	4	37.90	2.372	1	75.80	1.254	1

Figure A25 – X-ray diffraction pattern of Myrtöön sample MYR 40/2 (EEM-40)

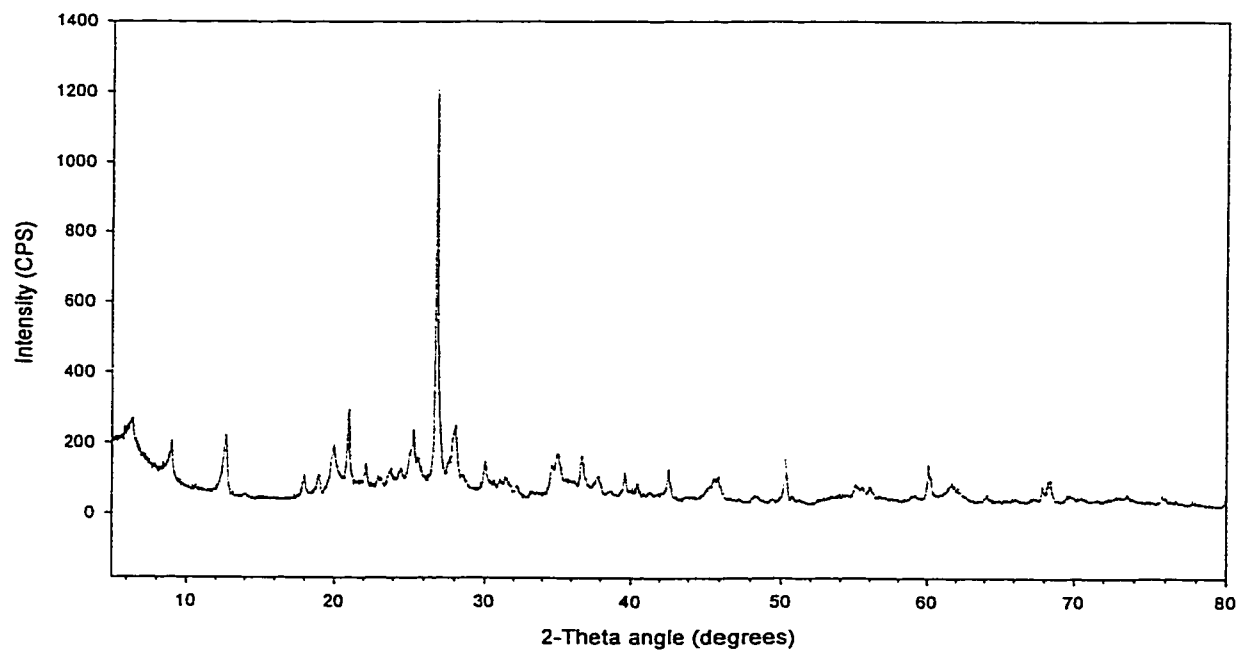


Figure A26 – X-ray diffraction pattern of Myrtöön sample MYR 40/7 (EEM-44)

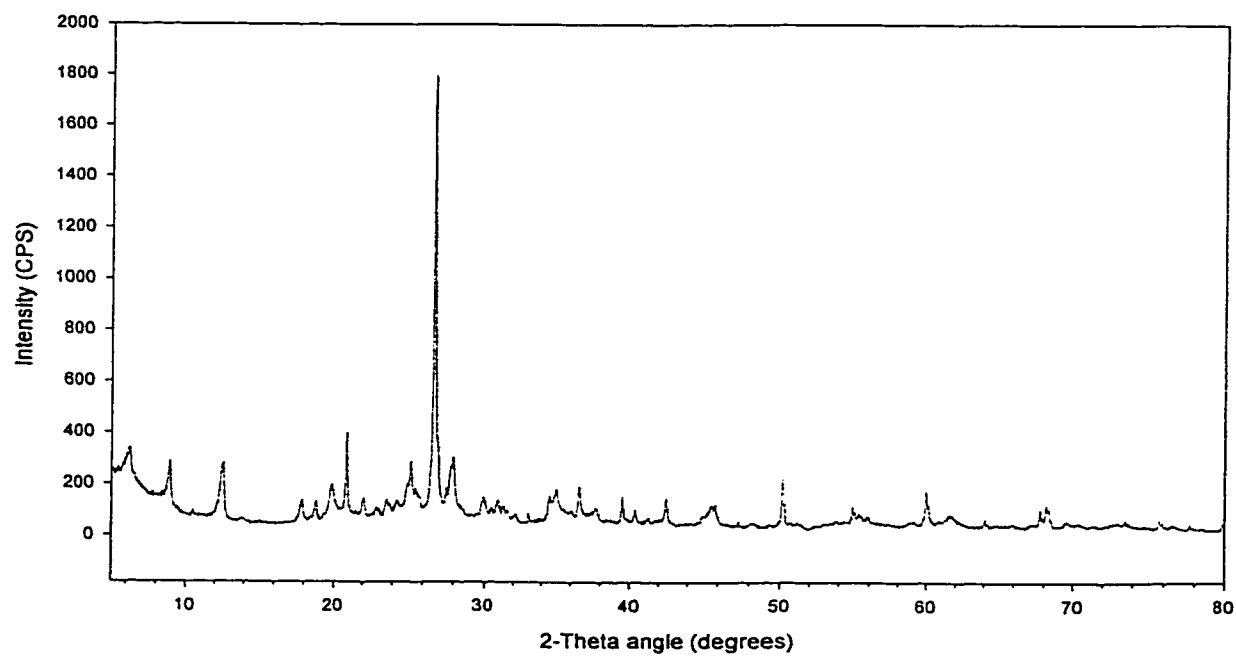


Table A25 – Peak list for Myrtöön sample MYR 40/2 (EEM-40)

2-theta angle (degrees)	d- spacing	relative intensity	2-theta angle (degrees)	d- spacing	relative intensity	2-theta angle (degrees)	d- spacing	relative intensity
6.36	13.89	8	30.00	2.976	5	45.33	1.999	2
9.00	9.818	8	30.36	2.942	1	45.62	1.987	4
12.58	7.031	13	30.65	2.915	1	45.91	1.975	5
14.00	6.321	1	31.02	2.881	2	48.27	1.884	1
17.98	4.93	3	31.40	2.847	2	50.26	1.814	12
18.88	4.697	3	31.64	2.826	2	50.76	1.797	1
19.94	4.449	8	32.16	2.781	2	54.97	1.669	3
21.04	4.219	12	33.17	2.699	1	55.26	1.661	1
22.14	4.012	4	34.65	2.587	5	55.48	1.655	2
22.98	3.867	2	35.04	2.559	7	55.95	1.642	2
23.74	3.745	1	35.83	2.504	1	60.07	1.539	9
24.46	3.636	2	36.68	2.448	8	61.71	1.502	3
25.02	3.556	5	37.80	2.378	3	62.12	1.493	2
25.24	3.526	11	38.59	2.331	1	64.13	1.451	1
25.58	3.48	4	39.58	2.275	5	67.86	1.38	4
26.76	3.329	100	40.40	2.231	3	68.25	1.373	6
28.04	3.18	12	41.40	2.179	1	69.58	1.35	1
28.44	3.136	2	69.58	1.35	1	75.73	1.255	1
30.00	2.976	5	42.57	2.122	7			

Table A26 – Peak list for Myrtöön sample MYR 40/7 (EEM-44)

2-theta angle (degrees)	d- spacing	relative intensity	2-theta angle (degrees)	d- spacing	relative intensity	2-theta angle (degrees)	d- spacing	relative intensity
6.24	14.15	7	27.96	3.189	11	45.47	1.993	3
8.88	9.95	9	29.88	2.988	3	45.79	1.98	4
10.48	8.434	1	30.50	2.929	1	47.31	1.92	1
12.48	7.087	11	30.96	2.886	3	50.17	1.817	11
13.84	6.393	1	31.26	2.859	2	54.87	1.672	4
17.82	4.973	4	31.56	2.833	1	55.33	1.659	1
18.78	4.721	3	32.10	2.786	1	55.84	1.645	1
19.84	4.471	6	33.04	2.709	1	59.98	1.541	7
20.86	4.255	17	34.45	2.601	3	61.57	1.505	2
22.02	4.033	3	34.58	2.592	3	64.08	1.452	1
22.90	3.88	1	34.97	2.564	5	67.75	1.382	3
23.02	3.86	1	36.06	2.489	1	68.14	1.375	5
23.60	3.767	2	36.56	2.456	7	69.52	1.351	1
24.28	3.663	1	37.39	2.403	1	73.46	1.288	1
24.94	3.567	4	37.65	2.387	2	75.66	1.256	2
25.16	3.537	9	39.47	2.281	6	77.62	1.229	1
25.50	3.49	3	40.30	2.236	3			
25.76	3.456	2	41.21	2.189	1			
26.66	3.341	100	41.29	2.185	1			
26.84	3.319	17	42.46	2.127	6			
27.52	3.239	3	44.95	2.015	1			

APPENDIX II

Major-element Chemical Composition Tables

Table A27 – Major-element composition of Philippi sample PH-1 358-362

Core Line #	PH1 358-362 (UT)
	90
SiO ₂	72.02
TiO ₂	0.45
Al ₂ O ₃	14.24
FeO	3.03
MgO	0.39
CaO	1.80
Na ₂ O	4.91
K ₂ O	2.78
Total	99.63

Table A28 – Major-element composition of Philippi sample PH-1 447-450

Core Line #	PH1 447-450 (MT)									
	81	82	83	84	85	86	87	88	89	Average
SiO ₂	72.25	71.82	72.17	72.09	72.10	71.73	71.71	71.84	71.82	71.95
TiO ₂	0.42	0.46	0.47	0.45	0.43	0.45	0.41	0.47	0.47	0.45
Al ₂ O ₃	14.15	14.39	14.31	14.29	14.33	14.39	14.28	14.25	14.36	14.31
FeO	3.12	3.07	3.13	3.15	3.10	3.21	3.15	3.17	3.23	3.15
MgO	0.42	0.42	0.40	0.41	0.36	0.40	0.41	0.42	0.45	0.41
CaO	1.75	1.66	1.66	1.66	1.60	1.74	1.68	1.67	1.66	1.67
Na ₂ O	4.75	5.08	4.97	4.95	5.01	5.08	5.31	5.00	5.01	5.02
K ₂ O	2.74	2.68	2.68	2.55	2.67	2.65	2.66	2.73	2.63	2.66
Total	99.61	99.57	99.79	99.54	99.60	99.65	99.61	99.55	99.62	99.62

Table A29 – Major-element composition of Philippi sample PH-1 630-640

Core Line #	PH1 630-640 (LT)									
	131	138	139	140	141	142	143	144	145	Average
SiO ₂	61.07	64.22	64.40	60.58	59.99	60.16	60.33	60.05	59.85	61.18
TiO ₂	0.38	0.04	0.01	0.40	0.44	0.41	0.41	0.42	0.44	0.33
Al ₂ O ₃	19.49	19.85	19.19	19.60	19.40	19.30	19.52	19.12	19.33	19.42
FeO	3.19	0.30	0.13	3.15	3.11	3.09	3.18	3.05	3.12	2.48
MgO	0.36	0.13	0.00	0.34	0.35	0.35	0.32	0.33	0.34	0.28
CaO	1.82	0.16	0.24	1.73	1.80	1.77	1.75	1.73	1.73	1.41
Na ₂ O	6.46	2.73	2.41	6.74	7.08	7.20	6.98	7.18	7.18	6.00
K ₂ O	5.96	12.32	13.25	6.18	6.56	6.45	6.16	6.79	6.78	7.83
Total	98.72	99.75	99.62	98.72	98.73	98.73	98.66	98.66	98.78	98.93

Table A30 – Major-element composition of Philippi sample PH-1 660-680

Core	PH1 660-680 (LT)				
Line #	77	78	79	80	Average
SiO ₂	61.33	61.44	61.55	61.28	61.40
TiO ₂	0.44	0.43	0.43	0.44	0.43
Al ₂ O ₃	18.65	18.69	18.42	18.69	18.61
FeO	2.95	3.03	2.99	2.89	2.97
MgO	0.31	0.32	0.32	0.33	0.32
CaO	1.74	1.71	1.69	1.70	1.71
Na ₂ O	6.85	6.71	6.80	6.80	6.79
K ₂ O	6.75	6.60	6.72	6.79	6.72
Total	99.02	98.93	98.92	98.92	98.95

Table A31 – Major-element composition of Philippi sample PH-2 487-490

Core	PH2 487-490 (UT)									
Line #	11	12	13	14	15	16	17	19	20	
SiO ₂	71.40	71.59	71.32	71.11	70.82	71.83	71.67	71.61	71.71	
TiO ₂	0.50	0.45	0.46	0.53	0.52	0.43	0.43	0.48	0.46	
Al ₂ O ₃	14.26	14.35	14.48	14.53	14.43	14.27	14.23	14.25	14.19	
FeO	3.28	3.18	3.16	3.26	3.32	3.11	3.22	3.21	3.13	
MgO	0.43	0.44	0.43	0.45	0.45	0.42	0.41	0.41	0.42	
CaO	1.64	1.72	1.86	1.73	1.74	1.57	1.70	1.75	1.72	
Na ₂ O	5.28	5.12	5.13	5.12	5.55	5.26	5.29	5.14	5.21	
K ₂ O	2.75	2.71	2.75	2.87	2.73	2.69	2.60	2.71	2.76	
Total	99.55	99.55	99.59	99.61	99.56	99.56	99.56	99.56	99.59	
Core	PH2 487-490 (UT) Continued									
Line #	21	22	23	24	25	27	28	29	31	Average
SiO ₂	71.66	71.82	71.71	71.89	71.94	71.74	71.85	71.95	71.56	71.62
TiO ₂	0.43	0.46	0.40	0.46	0.47	0.43	0.44	0.44	0.48	0.46
Al ₂ O ₃	14.17	14.42	14.37	14.42	14.46	14.32	14.40	14.38	14.35	14.35
FeO	3.24	3.16	3.10	3.17	3.10	3.15	3.10	3.08	3.12	3.17
MgO	0.40	0.40	0.42	0.41	0.42	0.42	0.42	0.40	0.41	0.42
CaO	1.70	1.66	1.65	1.70	1.63	1.65	1.71	1.63	1.64	1.69
Na ₂ O	5.26	5.02	5.23	4.85	4.87	5.22	5.08	5.08	5.29	5.17
K ₂ O	2.73	2.67	2.73	2.70	2.75	2.65	2.63	2.68	2.71	2.71
Total	99.59	99.60	99.60	99.61	99.63	99.57	99.63	99.63	99.57	99.59

Table A32 – Major-element composition of Philippi sample PH-2 528-530

Core Line #	PH2 528-530 (MT)														
	32	33	34	35	36	37	38	40	41	42	43	44	45	46 Ave.	
SiO ₂	71.82	71.89	71.73	70.35	71.63	71.80	71.94	71.86	71.91	72.14	71.85	71.88	71.27	72.03	71.72
TiO ₂	0.45	0.39	0.49	0.49	0.44	0.41	0.47	0.45	0.45	0.48	0.44	0.42	0.57	0.44	0.46
Al ₂ O ₃	14.34	14.32	14.38	14.18	14.44	14.30	14.28	14.31	14.33	14.23	14.26	14.39	14.08	14.35	14.30
FeO	3.13	3.21	3.13	4.26	3.13	3.11	3.11	3.13	3.08	3.00	3.19	3.16	3.87	3.06	3.26
MgO	0.41	0.42	0.43	0.40	0.42	0.39	0.40	0.39	0.40	0.40	0.41	0.40	0.39	0.41	0.41
CaO	1.72	1.62	1.77	2.03	1.63	1.66	1.63	1.61	1.73	1.73	1.77	1.67	1.66	1.65	1.71
Na ₂ O	4.92	5.12	5.01	5.07	5.25	5.18	5.23	5.06	5.06	4.84	4.98	4.88	5.02	4.99	5.04
K ₂ O	2.68	2.66	2.63	2.74	2.66	2.69	2.54	2.78	2.70	2.79	2.67	2.80	2.75	2.69	2.70
Total	99.47	99.61	99.57	99.53	99.61	99.54	99.61	99.58	99.65	99.62	99.57	99.60	99.62	99.62	99.59

Table A33 – Major-element composition of Philippi sample PH-2 830-840

Core Line #	PH2 830-840 (LT)								
	47	48	49	50	51	52	53	54	55
SiO2	61.35	61.40	61.32	62.98	61.54	61.64	61.67	61.39	61.52
TiO2	0.43	0.44	0.40	0.38	0.41	0.42	0.43	0.40	0.41
Al2O3	18.53	18.61	18.67	18.20	18.59	18.58	18.51	18.54	18.55
FeO	3.05	2.99	3.04	2.76	2.86	2.97	2.96	3.02	2.98
MgO	0.32	0.33	0.30	0.41	0.31	0.30	0.34	0.32	0.34
CaO	1.74	1.71	1.68	1.80	1.58	1.64	1.65	1.65	1.70
Na2O	6.70	6.94	6.96	6.04	6.91	6.84	6.96	6.89	6.88
K2O	6.86	6.57	6.56	6.82	6.73	6.53	6.38	6.69	6.54
Total	98.99	98.99	98.93	99.38	98.93	98.92	98.90	98.89	98.92
Core Line #	PH2 830-840 (LT) Continued								
	56	57	58	59	60	61	62	AVERAGE	
SiO2	61.57	62.00	61.59	61.78	61.55	61.35	61.58	61.64	
TiO2	0.42	0.41	0.44	0.40	0.39	0.41	0.40	0.41	
Al2O3	18.60	17.87	18.49	18.51	18.43	18.62	18.62	18.49	
FeO	3.02	3.05	3.00	2.95	3.02	2.98	2.92	2.97	
MgO	0.31	0.35	0.32	0.32	0.32	0.32	0.32	0.33	
CaO	1.62	1.66	1.68	1.72	1.64	1.67	1.70	1.68	
Na2O	6.92	6.76	6.90	6.55	7.11	6.57	6.83	6.80	
K2O	6.54	6.80	6.54	6.62	6.44	7.10	6.62	6.65	
Total	99.00	98.91	98.97	98.84	98.90	99.02	98.98	98.97	

Table A34 – Major-element composition of Philippi sample PH-2 840-855

Core Line #	PH2 840-855 (LT)				
	68	69	71	72	AVERAGE
SiO ₂	61.51	61.45	61.98	61.61	61.64
TiO ₂	0.43	0.40	0.37	0.41	0.40
Al ₂ O ₃	18.58	18.61	18.54	18.49	18.55
FeO	3.00	2.95	3.01	2.98	2.99
MgO	0.32	0.31	0.35	0.33	0.33
CaO	1.62	1.70	1.62	1.72	1.67
Na ₂ O	6.92	6.74	6.38	6.77	6.70
K ₂ O	6.54	6.86	6.84	6.59	6.71
Total	98.94	99.02	99.09	98.89	98.99

Table A35 – Major-element composition of Philippi sample PH-3 305-309

Core Line #	PH3 305-309 (MT)			
	74	75	76	AVERAGE
SiO ₂	72.09	71.66	71.78	71.84
TiO ₂	0.41	0.48	0.47	0.45
Al ₂ O ₃	14.17	14.27	14.35	14.27
FeO	3.12	3.11	3.15	3.13
MgO	0.40	0.42	0.42	0.41
CaO	1.64	1.70	1.74	1.69
Na ₂ O	5.11	5.23	5.00	5.11
K ₂ O	2.68	2.70	2.66	2.68
Total	99.61	99.57	99.59	99.59

Table A36 – Major-element composition of Philippi sample PH-3 565-570

Core Line #	PH3 565-570 (LT)				
	2	3	4	5	AVERAGE
SiO ₂	60.92	61.20	61.03	61.36	61.13
TiO ₂	0.46	0.44	0.42	0.40	0.43
Al ₂ O ₃	18.61	18.83	18.69	18.64	18.69
FeO	3.00	2.97	3.10	2.96	3.01
MgO	0.33	0.32	0.33	0.32	0.33
CaO	1.76	1.68	1.73	1.67	1.71
Na ₂ O	7.01	6.83	6.94	6.79	6.90
K ₂ O	6.84	6.63	6.60	6.88	6.74
Total	98.93	98.91	98.84	99.02	98.93

Table A37 – Major-element composition of Philippi sample PH-3 570-595

Core Line #	PH3 570-595 (LT)		
	6	9	AVERAGE
SiO ₂	61.39	61.36	61.37
TiO ₂	0.47	0.41	0.44
Al ₂ O ₃	18.67	18.76	18.72
FeO	2.95	2.96	2.96
MgO	0.35	0.34	0.34
CaO	1.72	1.71	1.72
Na ₂ O	6.10	6.22	6.16
K ₂ O	7.38	7.23	7.30
Total	99.04	98.99	99.01

Table A38 – Major-element composition of Myrtöön sample MYR 18/12

Core Line #	MYR 18/12
	91
SiO ₂	72.15
TiO ₂	0.50
Al ₂ O ₃	14.07
FeO	3.10
MgO	0.41
CaO	1.63
Na ₂ O	5.00
K ₂ O	2.74
Total	99.60

Table A39 – Major-element composition of Myrtöön sample MYR 18/13

Core Line #	MYR 18/13								
	27	28	29	30	31	32	34	35	AVERAGE
SiO ₂	71.09	71.21	71.19	70.97	71.25	71.50	70.89	71.07	71.15
TiO ₂	0.47	0.44	0.48	0.51	0.47	0.47	0.44	0.45	0.47
Al ₂ O ₃	14.57	14.55	14.64	14.82	14.49	14.74	14.84	14.84	14.69
FeO	3.35	3.35	3.35	3.38	3.46	3.34	3.45	3.38	3.38
MgO	0.44	0.44	0.41	0.44	0.45	0.44	0.45	0.43	0.44
CaO	1.76	1.76	1.72	1.77	1.74	1.78	1.82	1.77	1.77
Na ₂ O	5.24	5.08	4.95	4.93	5.00	4.58	4.95	4.82	4.94
K ₂ O	2.63	2.62	2.71	2.69	2.60	2.70	2.68	2.68	2.66
Total	99.54	99.45	99.47	99.52	99.46	99.55	99.51	99.44	99.49

Table A40 – Major-element composition of Myrtöön sample MYR 20/1

Core Line #	MYR 20/1									
	92	93	94	95	96	97	98	99	116	AVERAGE
SiO ₂	61.90	61.36	62.45	61.70	61.57	60.82	61.72	61.38	61.67	61.62
TiO ₂	0.38	0.43	0.39	0.42	0.42	0.41	0.43	0.43	0.44	0.42
Al ₂ O ₃	18.34	18.53	18.33	18.56	18.53	18.58	18.56	18.61	18.56	18.51
FeO	3.31	3.03	2.72	2.91	2.90	2.91	2.98	3.03	2.93	2.97
MgO	0.64	0.31	0.40	0.32	0.35	0.32	0.33	0.32	0.31	0.37
CaO	2.44	1.72	1.69	1.60	1.63	1.71	1.64	1.76	1.62	1.76
Na ₂ O	4.36	6.95	6.06	6.77	6.77	7.02	6.82	6.79	6.79	6.48
K ₂ O	8.14	6.68	7.23	6.59	6.76	7.00	6.48	6.58	6.65	6.90
Total	99.51	99.00	99.27	98.88	98.95	98.78	98.96	98.90	98.96	99.02

Table A41 – Major-element composition of Myrtöön sample MYR 20/2

Core Line #	MYR 20/2		
	100	101	AVERAGE
SiO ₂	61.70	61.94	61.82
TiO ₂	0.40	0.47	0.44
Al ₂ O ₃	18.55	18.61	18.58
FeO	3.02	2.90	2.96
MgO	0.32	0.33	0.33
CaO	1.64	1.61	1.62
Na ₂ O	6.84	6.46	6.65
K ₂ O	6.40	6.57	6.48
Total	98.87	98.90	98.88

Table A42 – Major-element composition of Myrtöön sample MYR 20/3

Core Line #	MYR 20/3		
	112	113	AVERAGE
SiO ₂	61.15	63.03	62.09
TiO ₂	0.41	0.36	0.38
Al ₂ O ₃	18.50	18.48	18.49
FeO	2.95	2.82	2.89
MgO	0.32	0.45	0.39
CaO	1.76	1.88	1.82
Na ₂ O	6.31	4.93	5.62
K ₂ O	7.49	7.50	7.49
Total	98.89	99.45	99.17

Table A43 – Major-element composition of Myrtöön sample MYR 37/1

Core Line #	MYR 37/1		AVERAGE
	12	13	
SiO ₂	59.71	59.58	59.64
TiO ₂	0.39	0.44	0.42
Al ₂ O ₃	19.51	19.74	19.63
FeO	2.99	3.09	3.04
MgO	0.33	0.37	0.35
CaO	1.69	1.68	1.68
Na ₂ O	7.75	7.67	7.71
K ₂ O	6.54	6.22	6.38
Total	98.91	98.79	98.85

Table A44 – Major-element composition of Myrtöön sample MYR 37/5

Core Line #	MYR 37/5				AVERAGE
	108	109	110	111	
SiO ₂	61.54	61.62	61.47	61.97	61.65
TiO ₂	0.43	0.38	0.43	0.39	0.41
Al ₂ O ₃	18.53	18.54	18.50	18.53	18.53
FeO	2.95	2.92	2.99	2.90	2.94
MgO	0.31	0.31	0.34	0.31	0.32
CaO	1.61	1.64	1.69	1.58	1.63
Na ₂ O	6.26	6.96	6.92	6.65	6.70
K ₂ O	7.39	6.46	6.60	6.60	6.76
Total	99.02	98.84	98.93	98.93	98.93

Table A45 – Major-element composition of Myrtöön sample MYR 39/2

Core Line #	MYR 39/2					AVERAGE
	104	105	106	107	117	
SiO ₂	74.21	74.61	74.25	74.09	74.20	74.27
TiO ₂	0.29	0.28	0.30	0.30	0.27	0.29
Al ₂ O ₃	13.77	13.72	13.73	13.86	13.85	13.78
FeO	2.08	2.11	2.07	2.04	2.10	2.08
MgO	0.30	0.30	0.29	0.29	0.29	0.29
CaO	1.42	1.37	1.41	1.39	1.40	1.40
Na ₂ O	4.46	4.00	4.41	4.54	4.42	4.36
K ₂ O	3.06	3.17	3.11	3.08	3.08	3.10
Total	99.58	99.57	99.56	99.58	99.59	99.58

Table A46 – Major-element composition of Myrtöön sample MYR 40/2

Core Line #	MYR 40/2
	102
SiO ₂	74.55
TiO ₂	0.29
Al ₂ O ₃	13.72
FeO	2.10
MgO	0.28
CaO	1.39
Na ₂ O	4.21
K ₂ O	3.06
Total	99.60

Table A47 – Major-element composition of Myrtöön sample MYR 40/7

Core Line #	MYR 40/7				
					AVERAGE
SiO ₂	60.44	60.62	60.59	56.14	59.45
TiO ₂	0.40	0.34	0.51	0.47	0.43
Al ₂ O ₃	20.56	19.62	18.94	22.16	20.32
FeO	3.52	3.13	3.57	3.51	3.43
MgO	0.41	0.58	0.39	0.37	0.44
CaO	1.78	1.54	1.56	1.83	1.68
Na ₂ O	4.80	7.10	5.75	7.95	6.40
K ₂ O	7.21	6.33	7.79	6.59	6.98
Total	99.12	99.26	99.10	99.02	99.13

GLOSSARY ^[2]

Andesite: a dark-colored, fine-grained extrusive rock that contains phenocrysts composed primarily of sodic plagioclase and one or more of the mafic minerals (e.g. biotite, hornblende, pyroxene).

Alkalic: igneous-rock series where the silica percentage is less than 51 and the CaO and $K_2O + Na_2O$ are equal.

Alkali basalt: a critically silica-undersaturated basalt.

Aegirine-augite: Transitional form of augite towards aegirine ($NaFeSi_2O_6$).

Anorthoclase: intermediate member between orthoclase and albite

Apatite: $Ca_5(PO_4)_3(F,Cl,OH)$. Most abundant phosphate in the earth's crust.

Augite: $Ca(Mg,Fe,Al)(Si,Al)_2O_6$. An intermediate member of the Diopside-Hedenbergite series. Occurs chiefly in volcanic rocks

Basalt: a general term for dark colored mafic igneous rocks.

Biotite: $K(Mg,Fe)_3[AlSi_3O_{10}](OH,F)_2$. Endogenic mineral that is the chief constituent of many igneous rocks, metamorphic rocks, and pegmatites.

Calc-alkalic: igneous-rock series where the silica percentage is between 56 and 61 and the CaO and $K_2O + Na_2O$ are equal.

Dacite: a fine-grained extrusive rock with the same general composition of andesite but having more quartz.

Extrusive: igneous rock that has been erupted onto the surface of the Earth.

Hypersthene: $(Mg,Fe)_2Si_2O_6$. Occurs in basic or ultrabasic igneous rocks.

Hornblende: $\text{NaCa}_2(\text{Mg,Fe,Al})_3(\text{Si,Al})_8\text{O}_{22}(\text{OH})_2$. Principal rock-forming mineral in igneous rocks.

Igneous: rock or mineral that solidified from molten or partly molten material.

K-trachyte: a potassium rich trachyte

Kaolinite: $\text{Al}_4[\text{Si}_4\text{O}_{10}](\text{OH})_3$. Widely distributed product of weathering of aluminosilicate minerals (chiefly feldspars) under acid conditions.

Lapilli: pyroclastics of a size range within the limits of 2 and 64 mm.

Lava: molten extrusive material, and also the rock that solidifies from it.

Mafic: igneous rock composed mainly of one or more ferromagnesian, dark-colored minerals.

Magma: naturally occurring mobile rock material, generated within the Earth from which igneous rocks are thought to have been derived.

Microcline: KAlSi_3O_8 . A triclinic intermediate of the orthoclase.

Muscovite: $\text{KA}_2[\text{AlSi}_3\text{O}_{10}](\text{OH})$. The most widespread of the mica minerals. Found as a rule only in granitic rocks.

Olivine: $(\text{Mg,Fe})_2\text{SiO}_4$. Main constituent of the ultrabasic and basic igneous rocks.

Orthoclase: KAlSi_3O_8 . A potassium feldspar that is a principal constituent of acidic igneous rocks.

Peat: an unconsolidated deposit of semicarbonized plant remains in a water-saturated environment, such as a bog or a fen. It is considered an early stage in the development of coal; carbon content is about 60% and oxygen content about 30%.

Peralkalic: igneous rock in which the molecular proportion of aluminum oxide is less than that of sodium and potassium oxides combined.

Phenocryst: relatively large, conspicuous crystal in finer-grained igneous ground mass.

Plagioclase: a group of feldspars of general formula $(\text{Na,Ca})\text{Al}(\text{Si,Al})\text{Si}_2\text{O}_8$ that are among the commonest rock-forming minerals. It form a complete solid solution series from Albite ($\text{NaAlSi}_3\text{O}_8$), or **plagioclase-sodic**, to Anorthite ($\text{CaAl}_2\text{Si}_2\text{O}_8$), or **plagioclase-calcic**.

Plinian eruption: explosive eruption in which a steady, turbulent stream of fragmented magma and magmatic components is released at a high velocity from a vent, with characteristically large volumes of tephra and tall eruption columns.

Pyroclastic: clastic rock material formed by volcanic explosion or aerial expulsion from a volcanic vent.

Pyrogenics: said of material that is related to intrusion and extrusion of magma and its derivatives.

Rhyodacite: a group of extrusive igneous rocks intermediate in composition between dacite and rhyolite, with quartz, plagioclase, and biotite (or hornblende) as the main phenocryst minerals, an a fine-grained ground mass composed of alkali feldspars and silica minerals.

Rhyolite: a group of extrusive igneous rocks with phenocrysts of alkali feldspars and quartz. It grades into rhyodacite with decreasing alkali feldspar content and into trachyre with a decrease in quartz.

Sanidine: $\text{K}(\text{Al,Si})_4\text{O}_8$. A monoclinic member of the orthoclase group

Sphene: CaTiSiO_5 . Also known as titanite. Very frequent accessory constituent of intermediate and acid igneous rocks, and analogous metamorphic rocks.

Strombolian: a type of volcanic eruption characterized by jetting of clots or fountains of fluid, basaltic lava from a central crater.

Trachybasalt: an extrusive rock intermediate in composition between trachyte and basalt.

Trachyte: a group of fine-grained extrusive rocks having alkali feldspar and minor mafic minerals (biotite, hornblende, or pyroxene) as the main components and possible a small amount of sodic plagioclase.

Tuff: consolidated pyroclastic rocks.

Volcaniclastic: volcanic rock containing volcanic material in whatever proportion, and without regard to its origin or environment.

Zircon: ZrSiO_4 . Frequent accessory mineral in acid igneous rocks like granites and syenites.